



HAL
open science

Circuits photoniques intégrés III-V/Si pour les applications en télécommunications optiques

Xavier Pommarede

► **To cite this version:**

Xavier Pommarede. Circuits photoniques intégrés III-V/Si pour les applications en télécommunications optiques. Autre. Université Paris Saclay (COmUE), 2017. Français. NNT : 2017SACLCO20 . tel-01552496

HAL Id: tel-01552496

<https://theses.hal.science/tel-01552496>

Submitted on 3 Jul 2017

HAL is a multi-disciplinary open access archive for the deposit and dissemination of scientific research documents, whether they are published or not. The documents may come from teaching and research institutions in France or abroad, or from public or private research centers.

L'archive ouverte pluridisciplinaire **HAL**, est destinée au dépôt et à la diffusion de documents scientifiques de niveau recherche, publiés ou non, émanant des établissements d'enseignement et de recherche français ou étrangers, des laboratoires publics ou privés.

NNT : 2017SACL020

THÈSE DE DOCTORAT
DE L'UNIVERSITÉ PARIS-SACLAY
PRÉPARÉE À CENTRALESUPELEC

Ecole doctorale n°573

Interfaces

Spécialité de doctorat : Physique

par

M. Xavier Pommarede

Hybrid III-V/Si photonic integrated circuits for optical
communication applications

Thèse présentée et soutenue à Palaiseau, le 24 Mai 2017.

Composition du Jury :

M.	XAVIER LETARTRE	Directeur de recherche École Centrale Lyon	(Rapporteur)
M.	DRIES VAN THOURHOUT	Professeur des universités Ghent University	(Rapporteur)
M.	ÉRIC CASSAN	Professeur des universités Center for Nanosciences and Nanotechnology	(Président)
Mme.	SÉGOLÈNE OLIVIER	Ingénieur de recherche CEA leti	(Examinatrice)
Mme.	ANNE TALNEAU	Directeur de recherche Center for Nanosciences and Nanotechnology	(Examinatrice)
M.	GUANG-HUA DUAN	Ingénieur de recherche III-V lab	(Directeur de thèse)
M.	JEAN-MICHEL KIAT	Directeur de recherche CentraleSupélec	(Directeur de thèse)
M.	PIERRE LECOY	Professeur des universités CentraleSupélec	(Directeur de thèse)

Table of Contents

1	Introduction : Photonic integrated circuits	4
1.1	An overview of Optical Fiber Communications	4
1.1.1	Internet bandwidth demand	5
1.1.2	Optical networks	5
1.1.3	Optical Components for fiber networks	7
1.2	Silicon photonics	11
1.2.1	Why Silicon Photonics?	11
1.2.2	The light source challenge	12
1.3	Fabrication process	12
1.3.1	The silicon process	13
1.3.2	The III-V process	15
1.4	Measurement setups	17
1.5	Aim of the thesis	18
1.6	Conclusion	19
2	Passive Building Blocks	22
2.1	Optical waveguides	22
2.1.1	Definition	22
2.1.2	Guide denomination	24
2.1.3	Strip waveguide characteristics	26
2.1.4	Rib waveguide characteristics	27
2.1.5	Propagation losses	29
2.2	Bend guides & bends	30
2.2.1	bend modes	30
2.2.2	Different types of guides & their parametrisation	31
2.2.3	Simulation setup	34
2.2.4	Simulation results	35
2.2.5	Experimental results	38
2.3	Periodic structures	39
2.3.1	Bragg Gratings	40
2.3.2	Fiber Grating Coupler	41
2.4	Waveguide crossings	42

2.5	Power splitter	44
2.5.1	Multimode Interferometer	45
2.5.2	Directionnal couplers	48
2.6	Ring resonators	54
2.7	The Mach-Zehnder interferometer	58
2.8	Optical Isolators	60
2.8.1	Present day commercial optical isolators	60
2.8.2	Non Reciprocal Phaseshift	61
2.8.3	Mach-Zehnder interferometers as isolators	63
2.9	Multimode Interferometers as Hybrid 90	64
2.9.1	Use and operation of an hybrid 90	64
2.9.2	4×4 Multimode Interferometer	66
2.10	Conclusion	71
3	Wavelength Division Multiplexing : passive devices	75
3.1	Ring resonators (de)-multiplexer	77
3.2	Echelle grating	78
3.2.1	Theory	79
3.2.2	Echelle grating for Dense WDM applications	81
3.2.3	Echelle grating for Coarse WDM applications	85
3.3	Arrayed Waveguide Gratings	89
3.3.1	Theory	89
3.3.2	Modelling	90
3.3.3	Simulation & measure	99
3.4	Conclusion	101
4	Active Components & Integration	105
4.1	III-V gain section	106
4.1.1	Structure	106
4.1.2	Transferring light from Silicon to InP	107
4.2	Semi-conductor Optical Amplifiers	109
4.3	Tunable Lasers	110
4.3.1	The Vernier effect	111
4.3.2	Experimental results	112
4.4	Electro-absorption modulators	114
4.4.1	Integrated laser with modulator : first generation	115
4.4.2	Integrated laser with modulator : second generation	119
4.5	Modulation with silicon junctions	121
4.5.1	Different types of silicon junctions	121
4.5.2	the PN junction	122
4.5.3	Mach-Zehnder modulators	123
4.6	I/Q modulators	125
4.6.1	I/Q modulators with PN junctions	125

4.6.2	I/Q modulators with electro-absorption modulators	129
4.6.3	Silicon vs EAM I/Q modulator	132
4.7	Conclusion	133
Conclusion & Perspectives		136
Résumé (Français)		139
List of Acronyms		142

Chapter 1

Introduction : Photonic integrated circuits

TELECOMMUNICATIONS in the form of digital communication has seen an incredible growth over the last decades [1, 2]. This growth was made possible thanks to the development of optical fiber communications, from the first semi-conductor laser in 1962 to the latest long-haul transmissions. Record data bandwidths exhibits an aggregate speed larger than 2Tb/s on a single fiber actually deployed on existing networks [3] or up to 65Tbit/s in a laboratory [4]. But further growth is expected in the coming years, which require new technologies to meet those needs.

This chapter will give an overview of the photonic integrated circuits (PIC), beginning an introduction to optical fiber communications, explaining why they are required and how they are implemented in today's networks. Then a part is devoted to the solution proposed by our team at III-V lab in the form of Silicon Photonics. The third part explains the different fabrication steps, with the silicon process on one side and the InP process on the other side. Part four describes the different measurement setups that will be used throughout the thesis. The last part is used to present the objectives of the thesis.

1.1 An overview of Optical Fiber Communications

In the last few decades, the world has lived through a revolution that has changed our lives : the internet. This revolution started in the 1990's and was made possible thanks to the incredible success of optical fiber networks. Free space links on long distances have gradually been replaced by optical fibers to the point where virtually the whole metro and long-haul networks are made out of optical fiber and new links being deployed everyday in access networks.

1.1.1 Internet bandwidth demand

The data traffic has grown from virtually nothing in 1990 and is expected to be over 1ZB in 2016 [1] and should double by 2020 [5]. This exponential growth is displayed in figure 1.1, which shows the past and predicted yearly world data traffic. This growth will be fed in the future by new applications that are being developed as the data bandwidth increases. Among the most notable sources of data traffic growth are the following :

- Smartphone traffic, which is expected to exceed PC-traffic by 2020 [5]
- Internet video, through streaming for instance. The advent of streaming for 4K videos put a huge pressure on access networks as they require very high data bitrates larger than 18 Mb/s per user.
- The internet of things : an ever-increasing number of objects will be connected, with 3.4 networked devices per capita by 2020 on average compared to 2.2 in 2015 [5]

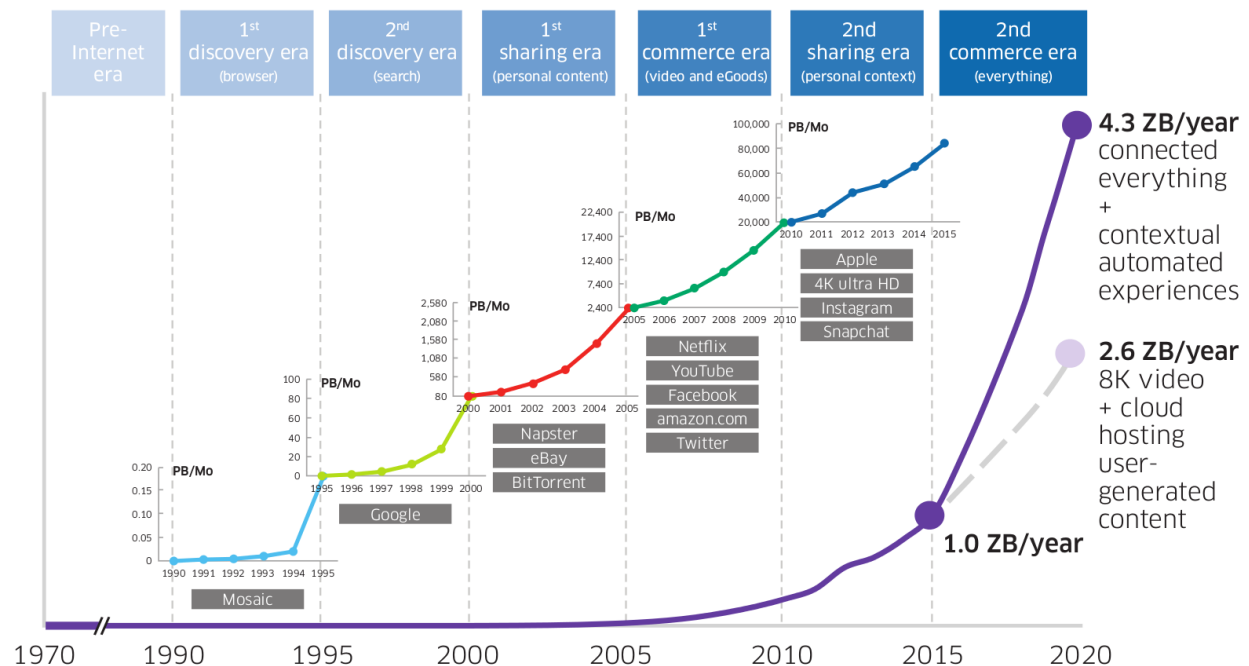


FIGURE 1.1: Growth of internet data traffic since 1990 and predictions for the next years

1.1.2 Optical networks

In order to fill the ever-increasing need for bandwidth as exposed in the previous section, optical networks have replaced free space communication. Today's networks are split in many levels, each with its own requirements. A schematic of all the network levels is shown in figure 1.2. One can distinguish 3 main levels : core, metro and access network.

Core networks are used for long distances at the scale of a country and even larger with for instance trans-oceanic cables. They have very few links but each of them must operate

at a high bit-rate and must be very reliable. This level puts an emphasis on individual performance far above the total cost.

Metro networks make the link between the long haul and the access networks. They are deployed at the scale of a region, with the main nodes located along each metropolitan area. The specifications for such a network are medium : a medium cost, medium bandwidth and medium consumption on a medium distance and a medium quantity of components required. Data centers are linked to the global network at this level.

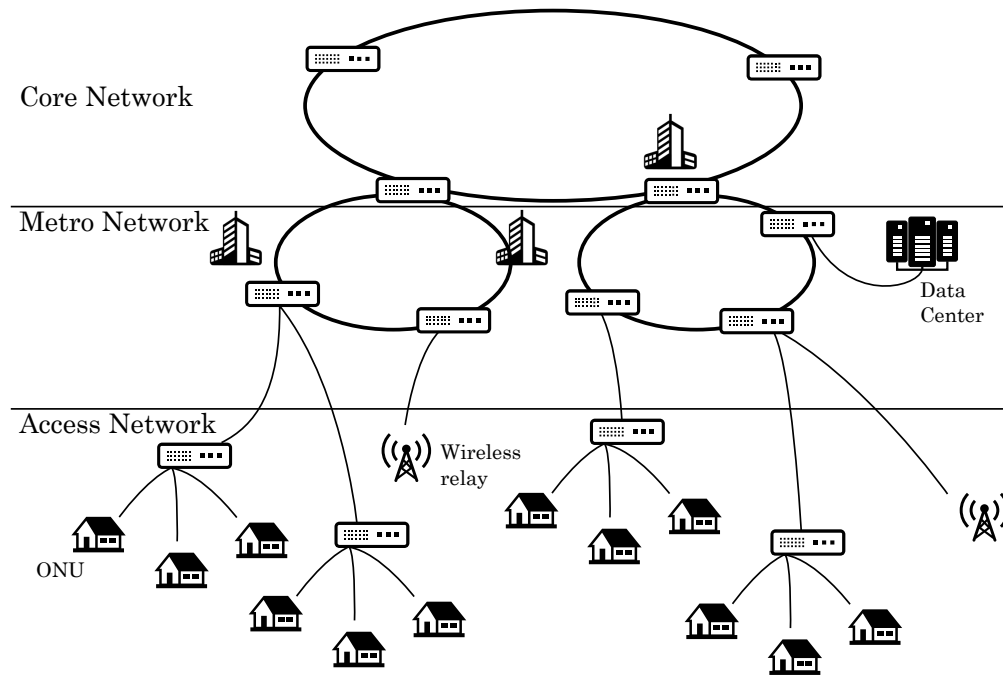


FIGURE 1.2: Schematic representation of an optical network. Long haul level not represented

Access networks on the other hand allow optical network units (ONU), or end user, to be connected to the whole network. In this layout, distances are much shorter, no more than 40km, but the number of connections is much higher. This implies that the unitary cost of a component must be very low. In consequence, the data rate in this segment are usually much lower than on the other segments. The norm for the next generation passive optical networks (NG-PON2) gives a data rate of 2.5Gb/s or 10Gb/s per ONU for instance [6]

A fourth level can be added to take into account the data center networks, which represent a large part of the global IP traffic. They require a large bandwidth over a very short distance, 10km maximum and usually shorter than 2km. But they require a high data bitrate on that short distance. The aggregated bandwidth for the incoming generation is typically 100Gb/s for each link.

A summary of the different levels and their expected performances are presented on table 1.1. In the context of this thesis, the focus will be on Metro network, access network and data center applications.

	Core	Metro	Access	Data centers
Distance	300-1000km	40-300km	<40km	0-10km
Max. Speed per fiber	>2Tb/s [3]	800Gb/s [7]	<1Gb/s	up to 400Gb/s
Link cost	++	+	-	-

TABLE 1.1: Performances for different network levels

1.1.3 Optical Components for fiber networks

The optical networks are made out of physical devices. The Open Systems Interconnection (OSI) "physical layer" [8] is made out of those physical devices. A table of the different OSI layers is presented in figure 1.3. All the devices studied throughout this thesis work at the physical layer level. They are the means by which information is created, transmitted and received. All the other levels rely on that base layer.

The rest section gives a summary of the main optical functions that are required in any optical network.

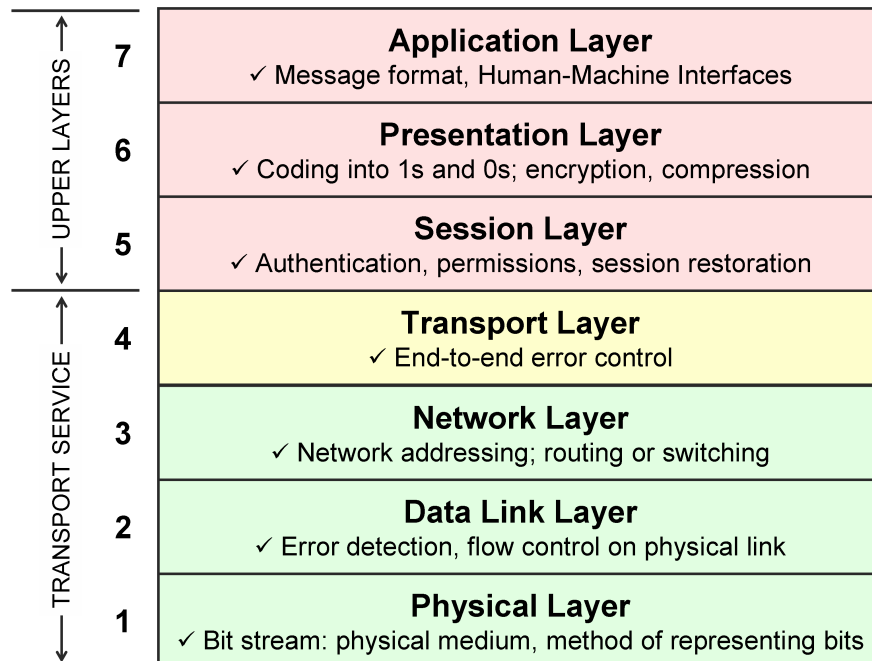


FIGURE 1.3: Description of the different layers in the Open System Interconnection model

Optical fiber

The optical fiber is considered to be the best medium for the transport of the optical signals. It consists of a cylindrical waveguide made out of silica with a slightly higher refractive index at the core. The fibers used in these networks are mostly single mode fibers (SMF). Commercial SMF exhibit losses of 0.25dB/km at the minimum of attenuation. Figure 1.4 shows the attenuation inside the fiber in relation with the different optical bands.

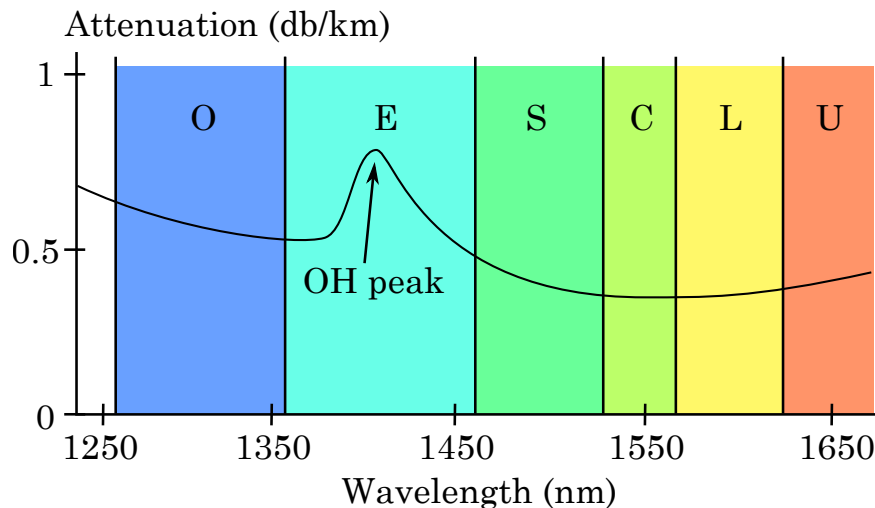


FIGURE 1.4: Attenuation in an optical fiber in relation with the telecom bands

The most commonly used bands are the O and C bands. In the O-band, SMFs present a minimum of dispersion at these wavelengths, thus reducing the need for dispersion management, therefore reducing the global cost. The O-band is mostly used in access networks and data centers. On the other hand, the C-band is located at the minimum of attenuation. This band is therefore very appreciated for longer distances such as in metro and core networks.

Light source

The optical fiber described above is only a mean of transportation for the optical signal. The first requirement for a communication terminal equipment is therefore the light source, usually in the form of a laser (laser is the acronym for light amplification by stimulated emission of radiation). They are usually semi-conductor lasers made out of III-V materials such as Indium Phosphide (InP) [9, 10]. The main characteristics of these lasers are the output power, wavelength, spectral purity, threshold current and power consumption. Depending on the network segment, the required specifications will be different : a laser designed for the long haul will require a long lifetime whereas a laser for the access networks will focus more on cost and consumption.

Modulator

The light source produces a continuous signal. The next step is to modulate the optical signal in order to encode the information. There are two different kinds of modulation. The first and simplest uses amplitude modulation : the information is coded in the optical signal intensity with 2 or more levels. The generic term is Power Amplitude Modulation (PAM), with the special case of 2 levels for On-Off Keying (OOK) and Non Return to Zero (NZR). In the second category, the information is coded in the phase of the signal with a constant intensity. The two most important representatives of that category are the Binary Phase Shift Keying (BPSK) and the Quadrature Phase Shift Keying (QPSK). One can also mix the amplitude and phase modulation. These are named Quadrature Amplitude Modulation (QAM). Figure 1.5 gives a schematic of the different modulation schemes described above in the I/Q domain. The modulation formats with more than 2 states increase the aggregate bandwidth of the signal. For instance, a QPSK signal will hold twice as much information as a BPSK signal.

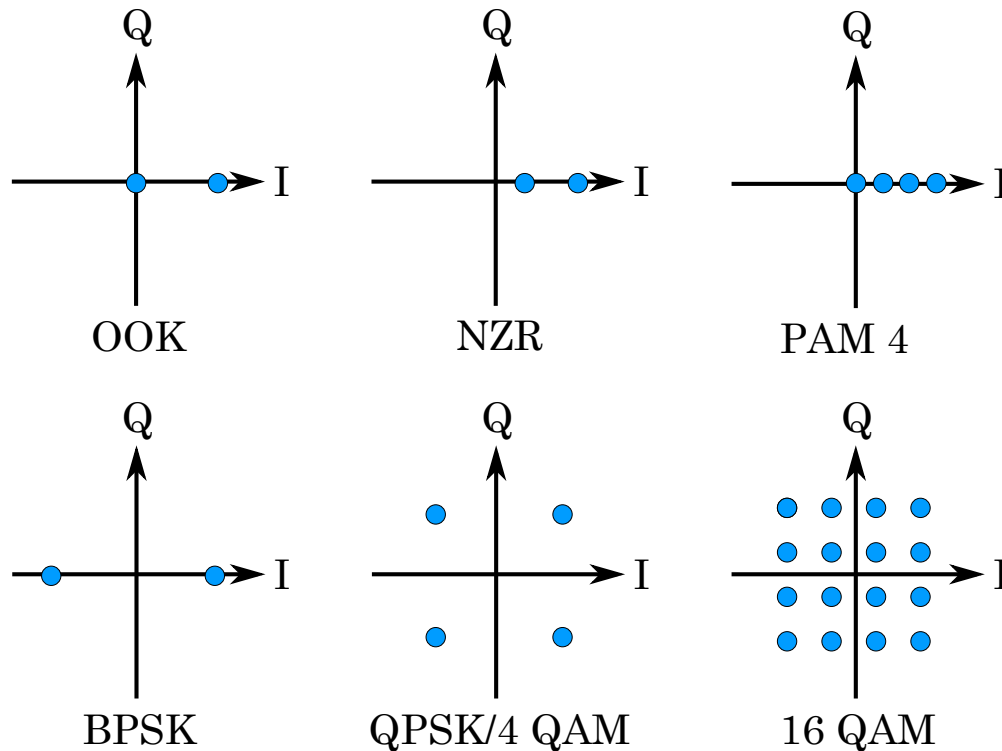


FIGURE 1.5: The different modulation formats represented in the I/Q domain

The PAM modulation can be made either with a directly modulated laser or with an external modulator. The phase modulation, on the other hand, usually requires an external modulator.

Modulators can be classified into two different categories. The first uses refractive index modulation that can be transformed in amplitude modulation or phase modulation with

tailored interferences. The second one absorbs light with a material whose absorption can be modulated. Mach-Zehnder modulators (see section 4.5.3) and Ring resonator modulators [11–13] belong to the first category and Electro-absorption modulators to the second (see section 4.4).

Photo-receiver

The alter-ego of the light source is the photo-receiver. Where the laser creates light from an injected current, the photo-receiver creates an electrical signal from injected light. They are usually made out of semi-conductor materials, either III-V materials [14, 15] or germanium on silicon [16, 17]. Their most important characteristics are the detection speed, or bandwidth, and sensitivity. While amplitude modulation uses a simple photodiode to make the de-modulation, phase modulation formats require a specific assembly of photodiodes and interferometers to make a coherent receiver (see section 2.9)

Optical amplifiers

Attenuation in an optical fiber is very low, but the distances at play are large enough that the signal needs to be amplified at some point. In the C-band, erbium-doped fiber amplifiers (EDFA) [18] are commonly used for that purpose. They exhibit a very powerful amplification with a flat gain in the C-band. No component with similar properties is commercially available in large quantities and low cost for the O-band. Semi-conductor optical amplifiers (SOA) can therefore cover that segment (see section 4.2). They can also be used in the C-band where compactness or integration is required [19].

Fabrication platform

All these building blocks mentioned above must be designed and fabricated according to the required specifications. No technology is capable of doing every function well for a low cost with a small footprint. Each technology has its advantages and drawbacks. A few of these are listed on table 1.2. Most platforms are able to perform only one or two functionalities. For instance, the lithium niobate platform can only provide modulators, with a large size and high unitary cost.

The only platform that can provide every function is the III-V platform. It can assemble on the same chip all the required functions in any optical network. Multiple integrated devices were created on that platform with for instance a laser source integrated with an EAM-based I/Q modulators [20] or multiple wavelength PN-junction based I/Q modulators [21]. These performances prove the efficiency and viability of that platform for complex devices. The main drawback is the unitary cost of the samples that remains relatively high.

The silicon platform on the other hand shows a lot of potential as it has all the building blocks available, except the light source and amplification, all that with a very low unitary cost and small footprint.

	Discrete Silica optics		III-V	Lithium Niobate	Silicon Nitride	Thick Si	Thin Si
Unitary cost	--	--	-	-	-	+	+++
Typ. Dimension	10cm	1cm	0.1cm	1cm	1cm	1cm	0.1cm
Possible integration	no	no	yes	no	yes	yes	yes
Light source	yes	no	yes	no	no	no	no
Modulator	yes	no	CD ² & EAM	EO coeff ¹	no	CD ²	CD ²
Photodiode	yes	no	yes	no	no	yes	yes

TABLE 1.2: Comparison of the different fabrication platforms for optical communications. 1 - EO coeff. = Electro-optic coefficient , 2 - CD = Carrier depletion

1.2 Silicon photonics

Several technologies have been developed to fill the needs of today's optical networks. Silicon photonic is one of the latest candidates which shows great promise.

1.2.1 Why Silicon Photonics ?

Silicon foundries were initially developed for the micro-electronic industry. They are able to create some of the core parts of any computer or smartphone such as the processor. In order to meet the huge market demand, technologies were developed to always decrease the unitary cost of every of these components. The consequence is a fabrication process with a very good yield and huge wafer sizes, up to 300mm in diameter. The idea of silicon photonics is to capitalize on all that knowledge and adapt the existing processes to the fabrication of photonic components.

Moreover, the very high index contrast that exists between the two main materials of that platform, silicon and silica, makes it possible to create waveguides with a very strong confinement (see section 2.1) and low losses as well as bends with very small curvatures (see section 2.2). These characteristics make silicon the perfect platform for passive components

and integrated circuits.

1.2.2 The light source challenge

On the other hand, silicon is a semi-conductor with indirect band-gap. As such, light emission is nearly impossible with that material. Studies have been performed on heavily doped and strained Germanium in order to transform it into a direct band-gap material [22]. But so far, the only reliable solution to have an on-chip light source is to mix silicon with a III-V material, either by flip-chip [23–26], direct epitaxy [27] or by hybrid integration. This last solution is the one implemented by our team at III-V lab/Leti [28–30] and by UCSB/intel [31].

With III-V on silicon hybrid integration, a wafer or a die made out of III-V material is bonded to the silicon wafer with a very thin silicon oxide boundary that permits optical mode transfer between the silicon and the III-V parts. With this kind of process, one can for instance create a laser with the gain section in the III-V and the filtering part in the silicon (see section 4.3).

1.3 Fabrication process

The components are fabricated at two different foundries : one to deal with the silicon process and one to deal with the InP process. Figure 1.6 gives a summary of the process flow. The silicon wafer is fabricated in a specific foundry with the process described in section 1.3.1. At the same time, InP wafers are epitaxiated with the required layer structure. The InP wafer is then bonded on the silicon wafer via molecular bonding. The silicon wafer is cut around the InP wafer and the III-V substrate is removed. Then comes the III-V process in another dedicated foundry.

Most of the silicon wafers used in this thesis are fabricated at the foundry at Leti in Grenoble. The rest of the III-V process is made at III-V lab in Palaiseau.

Some of the wafers are designed without the III-V material part. In that case, the backend process including the fabrication of heaters and metal connexions is realised at Leti.

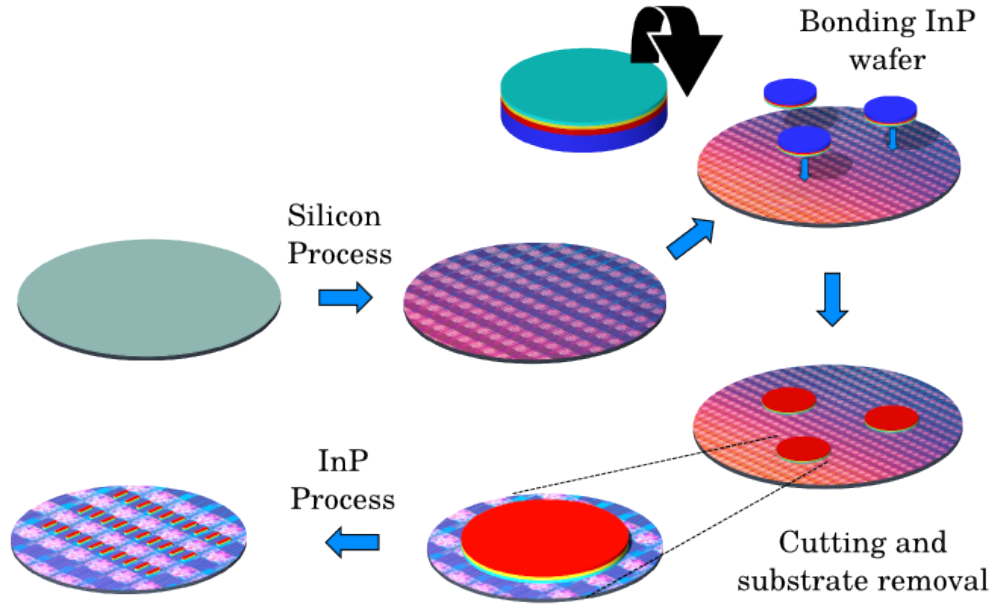


FIGURE 1.6: Hybrid III-V on silicon fabrication process flow

1.3.1 The silicon process

The whole silicon process is compatible with the complementary metal-oxide semiconductor (CMOS) platform used for microelectronics. It starts with a silicon wafer, usually 200mm in diameter, with a thin silicon layer on top of a buried oxide. In order to provide the best accuracy in structure definition, a dielectric mask is used to define the different levels of the waveguides. The lithography is made with deep UV at 193nm and the etching with partial reactive ion-etching (RIE). Some parts of the silicon waveguides are then submitted to a dopant implantation. These are for instance used to create the junctions in silicon modulators. The surface is finally encapsulated with silica by means of high density plasma deposition (HDP). The surface is then planarised with a chemical-mechanical planarisation (CMP). That last step is there to ensure a good flatness and smoothness of the interface, necessary condition for a good bonding with the InP wafer. Figure 1.7 gives a simplified representation of the process described above.

Figure 1.8 shows scanning electron microscope (SEM) images of a few fabricated devices. Fig. 1.8a is a Bragg grating, which are often used as mirrors in lasers. Fig. 1.8b shows a ring resonator (see section 2.6). These can be used to create wavelength division multiplexers (see section 3.1) or filter out Fabry-Perot modes in a laser cavity (see section 4.3). The power splitter used for that ring is a directional coupler (see section 2.5.2) Picture 1.8c and 1.8d are of a fiber grating coupler. Those are used to couple light in and out of the plane to a vertically-aligned fiber. The zoom on the grating in figure 1.8d is well defined, witness to the good fabrication process.

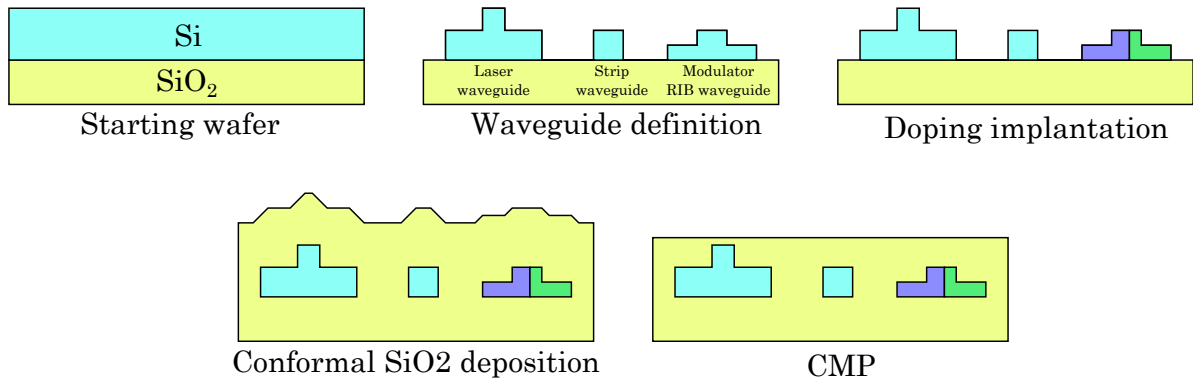


FIGURE 1.7: Simplified silicon process

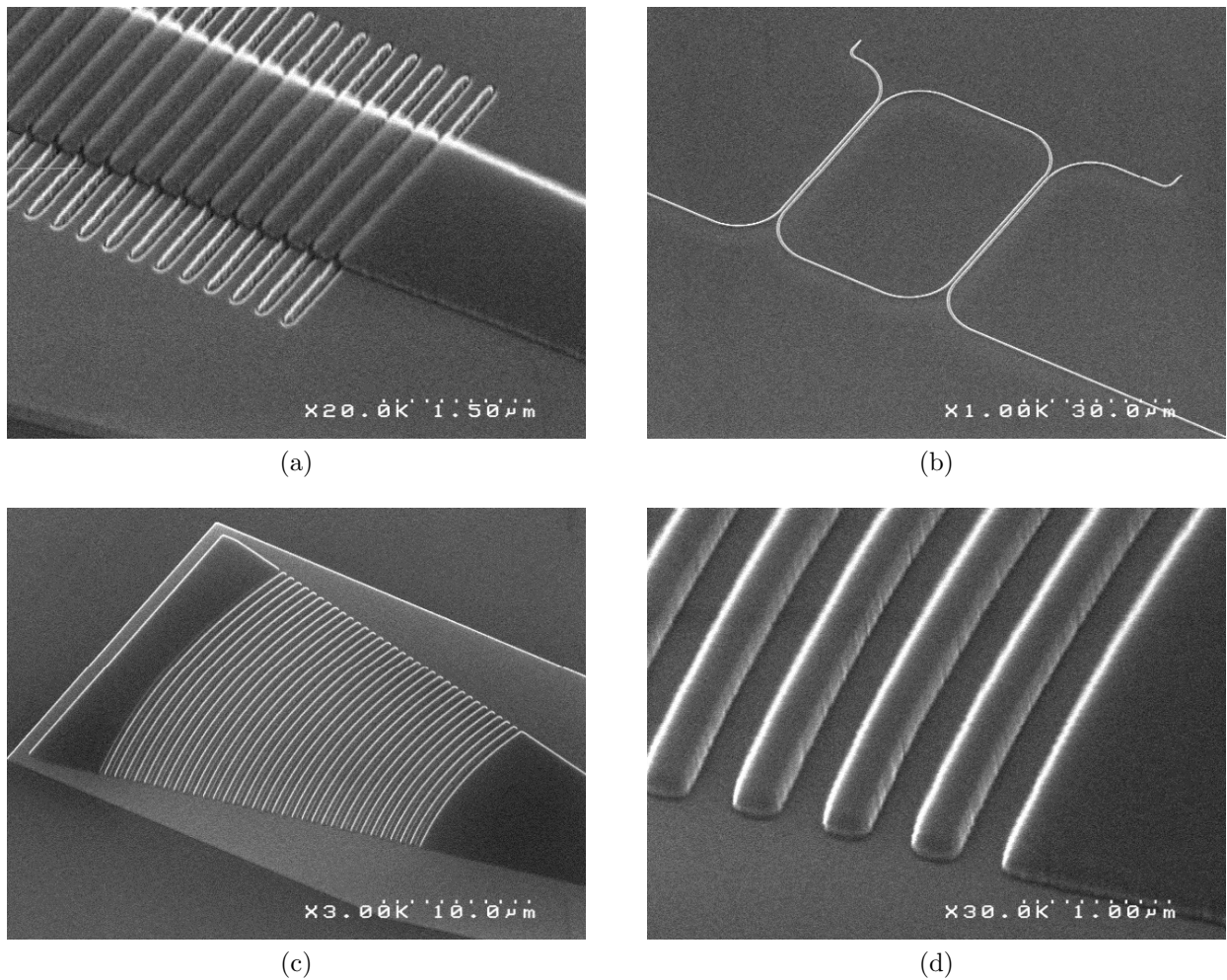


FIGURE 1.8: Scanning electron microscope image of fabricated devices on the silicon platform (a)bragg grating used as a mirror (b) ring resonator (c) Fiber grating coupler (d) Zoom on the grating of the FGC

1.3.2 The III-V process

The III-V process requires a different platform than the silicon one, with specific III-V equipments and processes. These steps are made at III-V lab. Once the bonding is done, the InP substrate is removed. The next step is a succession of lithography and etching in order to define the active sections. The heaters are made out of a thin layer of NiCr on top of an allumine buffer. The total resistance of the heater is usually designed to be around 100Ω . The next step is the first metal deposition. It is used to create heater contacts and the N-doped region contact. The whole stack is then buried in BCB. Vias are later made in the BCB to reach the first contacts. A second metallisation is deposited on top of the BCB. It is also used to link the top level to the bottom level through the aforementioned vias. A schematic of the process described above is presented in figure 1.9

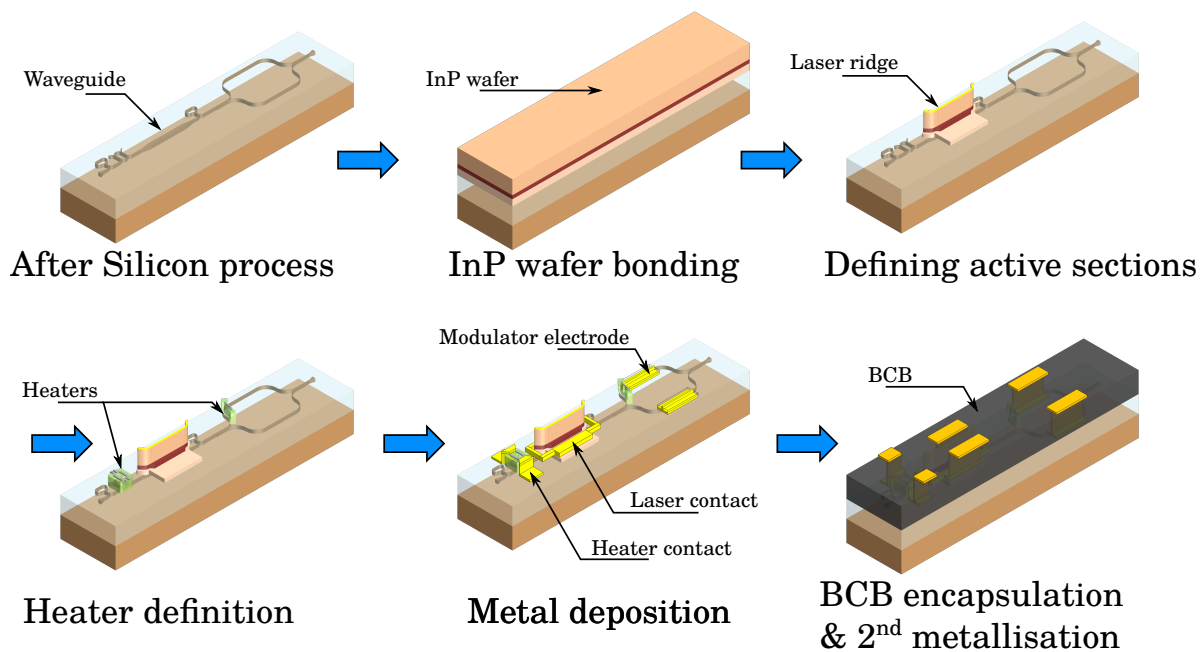
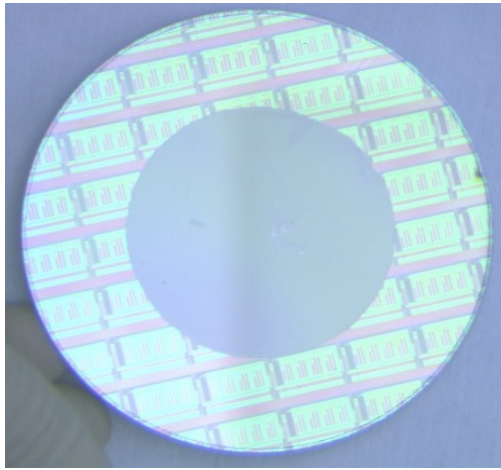
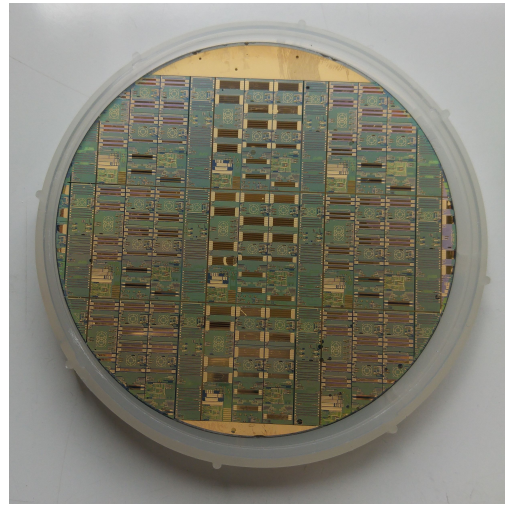


FIGURE 1.9: Simplified III-V process

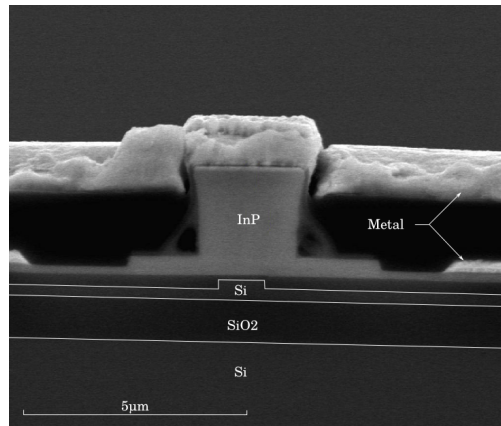
Figure 1.10 shows various images of the III-V process. Figure 1.10a shows a wafer photograph taken after the bonding step: the silicon wafer is already processed and a smaller InP wafer is bonded on top. Picture 1.10b shows a wafer at the end of the fabrication process. Figure 1.10c shows a SEM image of the gain section. One can distinguish the InP mesa on top of the silicon waveguide. The two different levels of metal are also visible on the picture. Figure 1.10d shows a top view with optical microscope of a tunable laser.



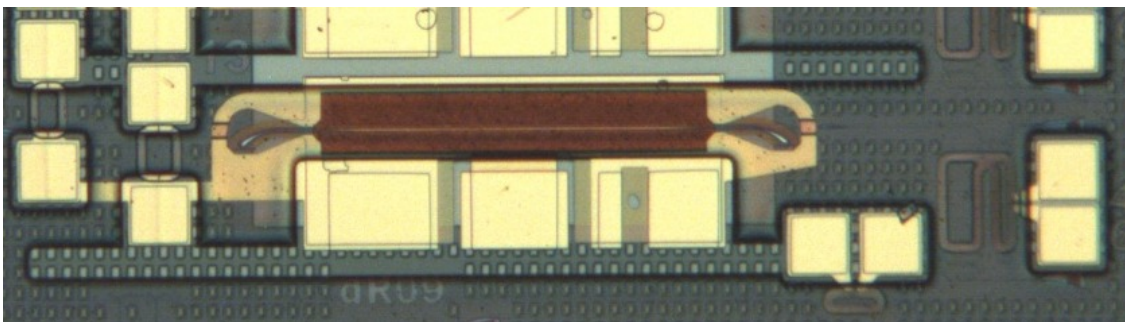
(a)



(b)



(c)



(d)

FIGURE 1.10: (a) Photograph of a silicon wafer with bonded InP wafer on top (b) Wafer after InP process (c) SEM image of an active section (d) Optical microscope image of a laser

1.4 Measurement setups

This section will describe the setups that were used to perform most of the measures presented in this thesis. There are two main categories of measures that correspond to two different setups. The first one has a light source integrated in the component (typ. lasers) and therefore has only one output fiber. The other one does not have an integrated light source and needs a second fiber to inject light in the component (typ. SOA, passive devices...). On top of that, metal probes can be added to the setup to electrically inject some parts of the device.

Light coupling out of the wafer is made with a fiber grating couplers (FGC) for all the measured samples throughout the thesis. In such a configuration, the fiber is set vertically with a 10° tilt angle. With fibers in such a position, wafer-scale testing becomes possible : every sample can be measured directly on the wafer without having to separate or cleave them first. FGCs are therefore compatible with automatic probers that are used in micro-electronics with minimal adaptation.

Figure 1.11a shows a macroscopic photograph of the setup used to make measurements of lasers and samples with an integrated light source. A vertical fiber and probes are disposed around the device, ready for measurement. Figure 1.11b shows a schematic representation of a tunable laser with fiber and probes in position.

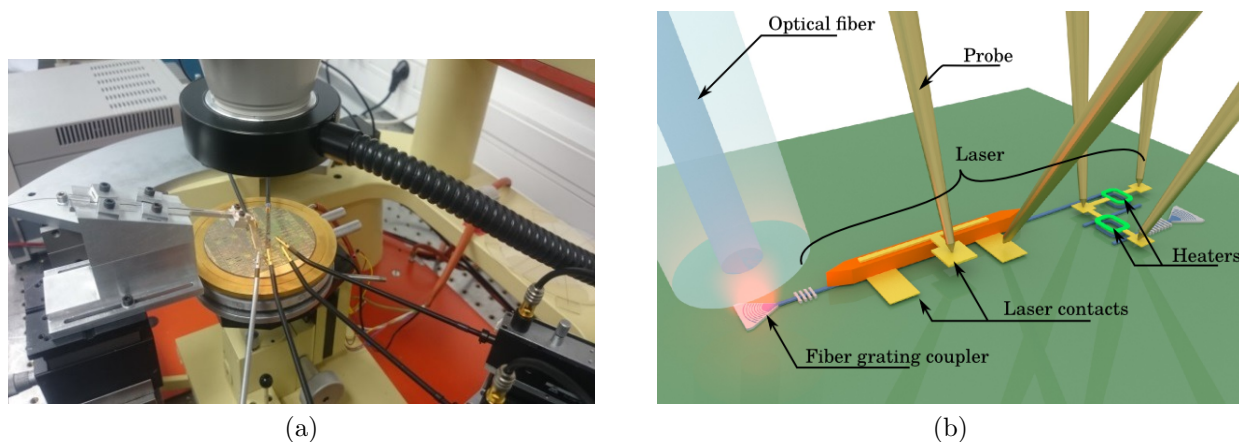


FIGURE 1.11: (a) Photograph of a manual prober with wafer, optical fiber and probes in position (b) Schematic of a laser with fiber and probes in position. Not to scale.

Figure 1.12a shows a setup with an input fiber and an output fiber. As for the previous setup, light is injected and collected with vertical fibers. Figure 1.12b shows a schematic of a multimode interferometer (MMI) under test.

In the case of passive device testing, the light source is usually an EDFA in the C-band and a large gain bandwidth SOA in the O-band. The latter source requires a polarisation controller and an isolator before the fiber grating coupler in order to work properly.

On the receiving side, the light is directed to a variety of measuring instruments such as power-meter and optical spectrum analyser (OSA).

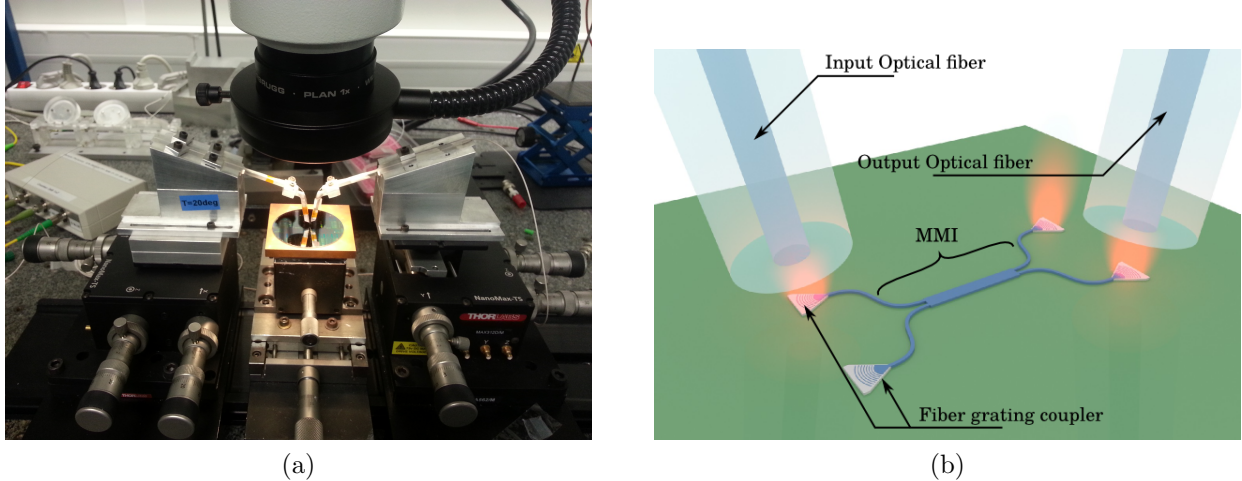


FIGURE 1.12: (a) Photograph of a bench with a wafer to be tested, optical fibers are in position (b) Schematic of a multimode interferometer (MMI) with fibers in position. Not to scale.

1.5 Aim of the thesis

This thesis evolves around the notion of integration. Having multiple functions on the same chip is the key towards low-cost and small-size devices. Having only one chip that integrates a light source, a modulator and an amplifier is much smaller and will have a lower power consumption than discrete devices assembled to form the same function.

The main difficulty relies in assembling the different functions in the same fabrication process with good performances, high yield and minimum parasitic interaction between the basic building blocks.

This thesis will therefore concentrate on three goals :

- Design and characterisation of all the basic building blocks that are necessary in the elaboration of integrated components. This task will analyse the possible parasitic effects and will try to optimise the building blocks with their integration in complex devices in mind.
- Design and characterisation of complex circuits based on the aforementioned building blocks. Two devices will be specifically studied. First the dual polarisation I/Q modulator for data bitrates up to 25Gbaud/s (see section 4.6). The second device is the coherent receiver, which is the receiving-end counterpart of the I/Q modulator.
- Design and characterisation of wavelength multiplexer/demultiplexer with in mind their integration in future work, for instance in multiple wavelength I/Q modulators.

1.6 Conclusion

Technology has enabled the creation of the internet and is always progressing to meet the ever-increasing demand. Silicon photonics and specifically the hybrid III-V on silicon platform could be a key technology to meet the needs of some markets. This platform is indeed capable of creating every kind of device from the passive building blocks to the light source and modulators. The main asset of that technology is the use of the mature microelectronics fabrication platform, unlocking very large wafers sizes and low fabrication costs. The other advantage is the high index contrast between silicon and silica that permits a small chip footprint and the integration of multiple functions on that same chip.

The different challenges announced in this chapter will be studied in the rest of the thesis. Chapter 2 is dedicated to basic passive structures, with the exception of wavelength (de)-multiplexers, which will be treated separately in chapter 3. These passive elements are necessary for all the circuitry and basic functions such as filtering or power splitting. The last chapter studies active components followed by their integration in I/Q modulators and coherent receivers. A general conclusion is drawn at the end of the thesis.

References

- [1] M. K. WELDON. *The Future X Network: A Bell Labs Perspective*. Crc Press, 2016.
- [2] R. MUNROE. *What if? Serious Scientific Answers to Absurd Hypothetical Questions*, pp192-194. John Murray Publisher, 2014.
- [3] Y. R. ZHOU et al. “Field Trial Demonstration of Real-Time Optical Superchannel Transport up to 5.6 Tb/s over 359km and 2Tb/s over a Live 727km Flexible Grid Link using 64GBaud Software Configurable Transponders”. In : *Optical Fiber Communication Conference*. Optical Society of America. 2016, Th5C–1.
- [4] A. GHAZISAEIDI et al. “65Tb/s Transoceanic Transmission Using Probabilistically-Shaped PDM-64QAM”. In : *ECOC 2016–Post Deadline Paper (2016)*.
- [5] V. CISCO. “The Zettabyte Era: Trends and Analysis”. In : *Updated (02/06/2016)*, <http://www.cisco.com/c/en/us/solutions/collateral/service-provider/visual-networking-index-vni/vni-hyperconnectivity-wp.html> ().
- [6] *40-Gigabit-capable passive optical networks (NG-PON2): General requirements*. ITU-T G.989.1. International Telecommunication Union. Mar. 2013.
- [7] *100G OTN TRANSPONDER*. Infinera. 2016.
- [8] *The OSI model*. URL : <https://osi-model.com> (visité le 19/12/2016).
- [9] G. P. AGRAWAL et N. K. DUTTA. *Semiconductor Lasers, second edition*. KLUWER ACADEMIC PUBLISHERS, 1993.
- [10] A. J. WARD et al. “Widely tunable DS-DBR laser with monolithically integrated SOA: design and performance”. In : *IEEE Journal of selected topics in quantum electronics* 11.1 (2005), p. 149–156.

- [11] Q. XU et al. “Micrometre-scale silicon electro-optic modulator”. In : *nature* 435.7040 (2005), p. 325–327.
- [12] M. PANTOUVAKI et al. “50Gb/s Silicon Photonics Platform for Short-Reach Optical Interconnects”. In : *Optical Fiber Communication Conference*. Optical Society of America. 2016, Th4H–4.
- [13] K. XU et al. “56 Gbit/s DMT Signal Generated by an Integrated Silicon Ring Modulator”. In : *CLEO: Science and Innovations*. Optical Society of America. 2016, STu1G–7.
- [14] H. ITO et al. “InP/InGaAs uni-travelling-carrier photodiode with 310 GHz bandwidth”. In : *Electronics Letters* 36.21 (2000), p. 1.
- [15] M. ANAGNOSTI et al. “Record Gain x Bandwidth (6.1 THz) Monolithically Integrated SOA-UTC Photoreceiver for 100-Gbit/s Applications”. In : *Journal of Lightwave Technology* 33.6 (2015), p. 1186–1190.
- [16] L. VIVIEN et al. “42 GHz waveguide germanium-on-silicon vertical PIN photodetector”. In : *2008 5th IEEE International Conference on Group IV Photonics*. Sept. 2008, p. 185–187.
- [17] H. CHEN et al. “- 1 V bias 67 GHz bandwidth Si-contacted germanium waveguide pin photodetector for optical links at 56 Gbps and beyond”. In : *Optics Express* 24.5 (2016), p. 4622–4631.
- [18] E. DESURVIRE et al. *Erbium-doped fiber amplifier*. US Patent 5,005,175. Avr. 1991.
- [19] P. KASPAR et al. “Packaged hybrid III-V/silicon SOA”. In : *2014 The European Conference on Optical Communication (ECOC)*. Sept. 2014, p. 1–3.
- [20] G. de VALICOURT et al. “Monolithic integrated InP transmitters using switching of prefixed optical phases”. In : *Journal of Lightwave Technology* 33.3 (2015), p. 663–669.
- [21] R. NAGARAJAN et al. “InP photonic integrated circuits”. In : *IEEE Journal of Selected Topics in Quantum Electronics* 5.16 (2010), p. 1113–1125.
- [22] K. GUILLOY. “Germanium déformé pour l’émission de lumière”. Thèse de doct. Université de Grenoble Alpes, 2016.
- [23] K. NEMOTO, T. KITA et H. YAMADA. “Narrow spectral linewidth wavelength tunable laser with Si photonic-wire waveguide ring resonators”. In : *The 9th International Conference on Group IV Photonics (GFP)*. 2012.
- [24] J. DALLESASSE et S. B. KRASULICK. *Method and system for template assisted wafer bonding*. US Patent 8,222,084. Juil. 2012.
- [25] C.-C. LIU et al. “The microstructure investigation of flip-chip laser diode bonding on silicon substrate by using indium-gold solder”. In : *IEEE Transactions on components and packaging technologies* 26.3 (2003), p. 635–641.
- [26] S. TANAKA et al. “High-output-power, single-wavelength silicon hybrid laser using precise flip-chip bonding technology”. In : *Optics express* 20.27 (2012), p. 28057–28069.

- [27] A. Y. LIUA et al. “Quantum dot lasers on silicon”. In : (2014).
- [28] M. LAMPONI et al. “Low-threshold heterogeneously integrated InP/SOI lasers with a double adiabatic taper coupler”. In : *IEEE photonics technology letters* 24.1 (2012), p. 76–78.
- [29] A. LE LIEPVRE et al. “Widely wavelength tunable hybrid III–V/silicon laser with 45 nm tuning range fabricated using a wafer bonding technique”. In : *The 9th International Conference on Group IV Photonics (GFP)*. 2012.
- [30] G.-H. DUAN et al. “Hybrid III–V on Silicon Lasers for Photonic Integrated Circuits on Silicon”. In : *IEEE Journal of selected topics in quantum electronics* 20.4 (2014), p. 158–170.
- [31] A. W. FANG et al. “Electrically pumped hybrid AlGaInAs-silicon evanescent laser”. In : *Optics express* 14.20 (2006), p. 9203–9210.

Chapter 2

Passive Building Blocks

PASSIVE building blocks (BB) are very important in any fabrication platform, but even more so on the silicon photonic platform. As explained in section 1.2, silicon photonics present many advantages, one of them is a high index contrast with low losses, which enables highly confined waveguides. This confinement with subsequent small footprint and small bend radii makes this platform excellent for photonic integrated circuits (PIC) [1]. But optical waveguides are not the only necessary components in order to achieve a full integration platform. Other components are required such as power splitter, guide crossings or ring resonators. With all these elementary building blocks, one can design more complex functions integrating many of these passive building blocks.

This chapter will discuss these building blocks, starting with the basic waveguides and bends, followed by periodic structures, guide crossings and power splitters, which are necessary in the design of the ring resonators, Mach-Zender and integrated isolators studied in the next sections. A design of a Hybrid 90, necessary for a coherent receiver, in the form of a multimode interferometer is presented in the last section of this chapter.

2.1 Optical waveguides

2.1.1 Definition

Optical waveguides are the elementary component of any silicon photonic circuit. Their goal is to transport light from point A to point B with minimum losses, minimum reflection and with a good control of the phase. A single mode behaviour is usually required, but not for every application. There are two main types of waveguides, the strip waveguide and the rib waveguides. A schematic is presented in figure 2.1. The slab waveguide is also presented but is different from the previous ones as the light is only guided in one direction instead of two. It acts as a semi-free propagation region. One of its main uses is to expand a light beam, which is very useful in the design of wavelength (de)multiplexer, presented later in chapter 3.

The strip waveguide is a rectangle of silicon surrounded by silica. As such it has the

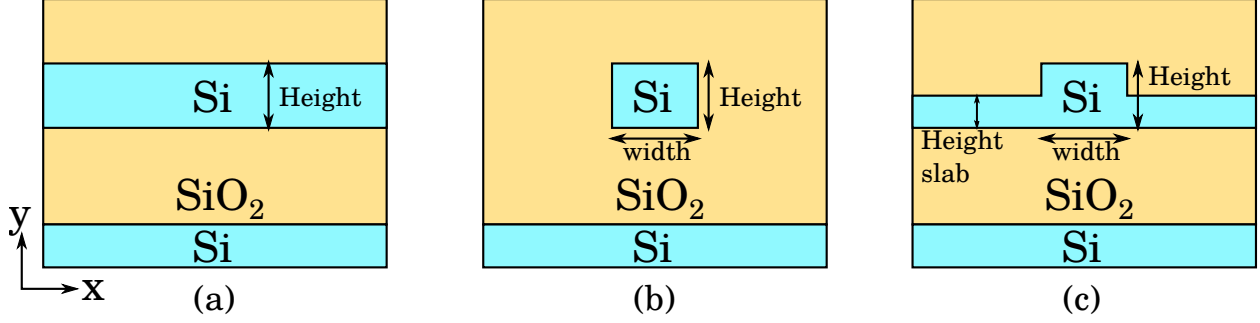


FIGURE 2.1: Schematic view of (a) a slab waveguide (b) a strip waveguide and (c) a rib waveguide

strongest confinement of all presented waveguides. Its main advantage is its great robustness to fabrication with only 2 variables : height and width. It can also make very sharp bends with radius as low as a few microns. On the other hand, it suffers from higher losses than the rib waveguide, with propagation losses around 4dB/cm (see section 2.1.5).

The rib waveguide on the other hand present a partially etched guide with a slab beneath. It is much less confined than the strip waveguide, providing lower propagation losses. The main drawback is the necessity to create advanced bends with large radius in order to achieve reasonable losses, as discussed later in section 2.2

A waveguide such as the aforementioned strip and rib waveguides can guide light in a number of “modes”. These modes represent the natural propagation waveforms and have a specific electrical and magnetic field distribution. These modes form a complete basis, meaning that any light distribution propagation in the waveguide can be described as a linear combination of natural modes :

$$\vec{E} = \sum_{i=0}^{\infty} A_i \cdot \vec{E}_i \quad (2.1)$$

with coefficient A_i extracted from the overlap integral of the incoming field with the considered mode :

$$A_i = \int_S \vec{E} \wedge \vec{H}_i^* \cdot d\vec{S} \quad (2.2)$$

The modes are normalised and orthogonal between themselves, as described in equation 2.3, where E_i and H_j are the electric and magnetic fields of respectively mode number i and j . $\delta_{i,j}$ is the Kronecker symbol.

$$\int_S \vec{E}_i \wedge \vec{H}_j^* \cdot d\vec{S} = \delta_{i,j} \quad (2.3)$$

In the waveguides we are studying, the dominant part of the electric field is usually parallel or perpendicular to the substrate. These modes are called respectively *TE* and *TM* modes. For instance, a TE mode will have $\vec{E} \simeq E \cdot \vec{u}_x$ with \vec{u}_x in the horizontal plane. The

mode with the highest index is called the fundamental mode. The TE and TM mode with the highest effective index are called TE^0 or TM^0 respectively. they usually have one lobe whereas higher order modes have many of those (see figure 2.2).

Power can be exchanged from one mode to another when the waveguide has its geometry perturbed, such as in a bent waveguide. In such cases, the bend modes have a different field profile than the straight one. Light propagating in the straight TE^0 mode will have a non-zero overlap with the bend TE^1 mode : there will be a power exchange between the two modes. Part of the straight TE^0 power will be transferred to the bend TE^1 mode. Most of the time, the waveguides are therefore required to be single mode with only the TE^0 mode available, with eventually the presence of the TM^0 mode in order to avoid power exchange between different modes.

The two main parameters that can characterise a waveguide mode are its effective index and group index. The effective index, n_{eff} , is the equivalent of the refractive index for a guided mode. It takes into account the different materials in which the optical mode has to propagate and gives back an averaged propagation constant in the form of an effective index, n_{eff} . The group index on the other hand takes into account the material and waveguide dispersion. It is defined by the following relation , with λ the wavelength :

$$n_g = n_{eff} - \lambda \cdot \frac{dn_{eff}}{d\lambda} \quad (2.4)$$

There are various methods used to calculate that effective index. The ones I used are the Finite Difference Mode (FDM)[2] method and Film Mode Matching (FMM)[3] method which have been implemented by the Fimmwave commercial software [4]. The FDM method is a pure numerical solver and is usually faster and always finds the required modes, whereas the FMM method is a semi-analytical method that calculates 1D modes in simplified vertical structures and then regroups them numerically to create the final waveguide. It is slower than FDM and does not always converge, but is more accurate.

2.1.2 Guide denomination

In order to give a clear definition of guides, the following rule will be applied to denominate all guides for the rest of the thesis :

$$type\ H - H_{slab}\ Wx\ @y.y \quad (2.5)$$

with type the kind of guide, H its height in nm and W its width in μm . H_{slab} is optionnal and gives the slab height for a rib waveguide. The guide is studied at a wavelength of $y.y$ For instance, 'rib 300-150 W0.45 @1.54' denotes a rib waveguide of width $0.45\mu m$ with a height of $300nm$ and a slab of $150nm$ at a wavelength of $1.54\mu m$.

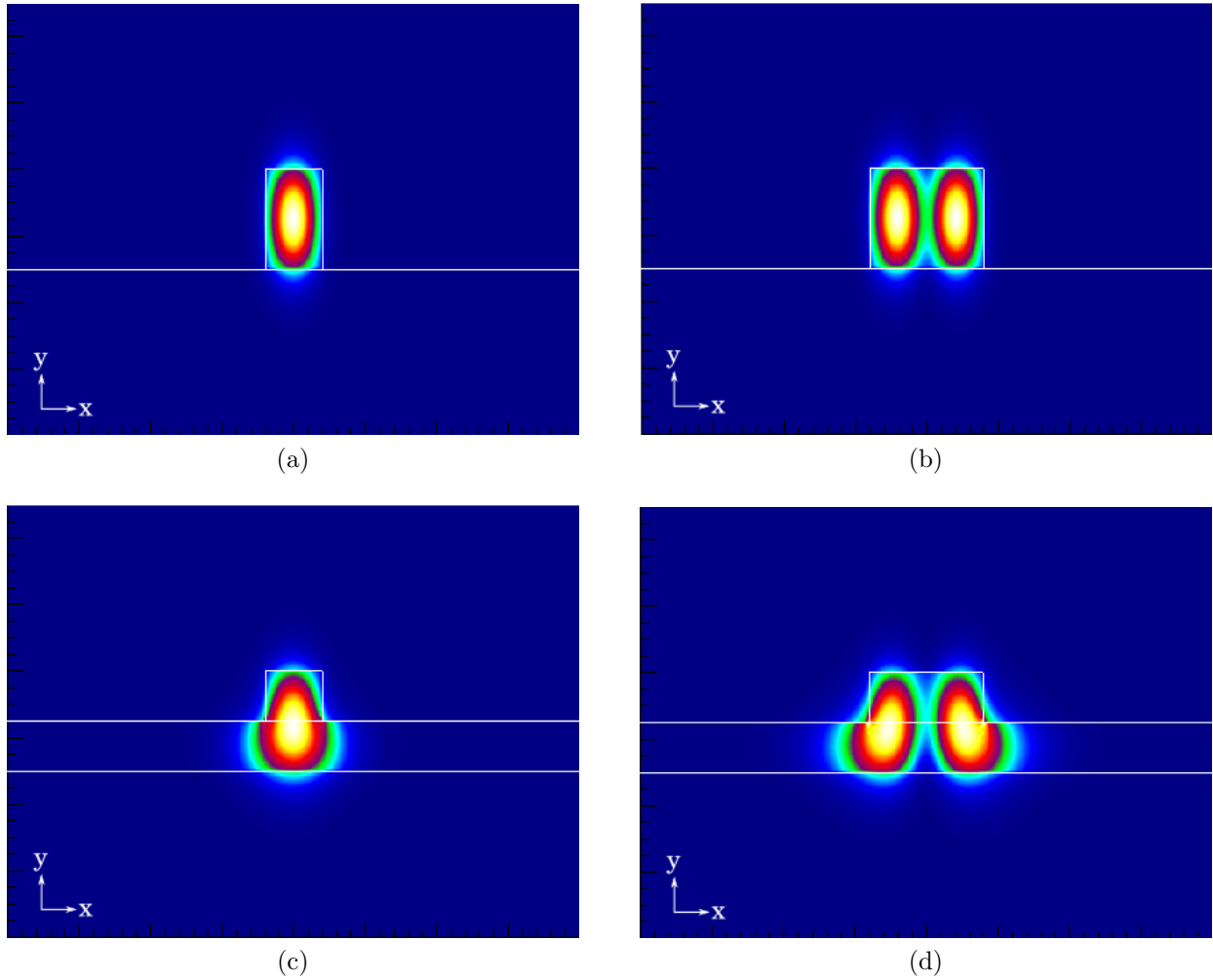


FIGURE 2.2: Intensity mode profile of a (a) TE^0 mode in strip 300 W0.4 @1.54 (b) TE^1 mode in strip 300 W0.8 @1.54 (c) TE^0 mode in rib 300-150 W0.4 @1.54 (d) TE^1 mode in rib 300-150 W0.8 @1.54

2.1.3 Strip waveguide characteristics

Strip waveguides are mostly used for their very high confinement, which in turn enables extremely small bends. This can in turn be very useful for devices such as ring resonators with a very large free spectral range (see section 2.6).

n_{eff} and n_g

The effective and group index for the three main modes in a strip waveguide are presented in figure 2.3 as a function of waveguide's width. The waveguide height is set at 300nm and the wavelength at $1.54\mu\text{m}$

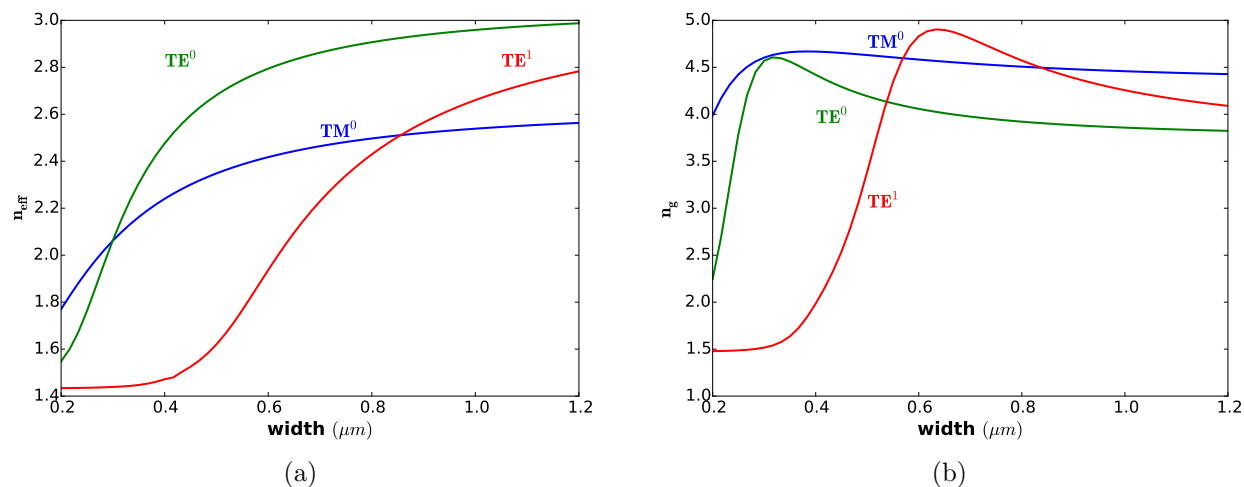


FIGURE 2.3: (a) Effective index (b) Group index of the 3 main modes of a strip waveguide in function of width for a strip 300 @1.54

The TE^0 and TM^0 modes always coexist, but there is no problem as it is very unlikely to have power transfer from one to the other. On the contrary, the TE^0 mode would be likely to exchange power with the TE^1 mode, inside a bend for instance. The TE^1 mode is not guided for a width lower than $W = 0.4\mu\text{m}$: the effective index of the mode is very close to that of Silica, meaning that the mode is not guided inside the silicon. To be on the safe side, the chosen value at this wavelength is set at $0.38\mu\text{m}$ and thus ensures a good rejection of the TE^1 mode.

Wavelength and Temperature variations

The next simulation takes into account the variation of effective index of the TE^0 with respect to wavelength and temperature. The results are presented in figure 2.4.

Wavelength has a large impact on the effective index. This is partly due to the silicon refraction index change with wavelength, but mostly to the change of the electric field with respect to wavelength. The mode at longer wavelengths will be less confined with more field

in the silica cladding, leading to a reduced index compared to shorter wavelengths. The immediate consequence is the large dispersion in silicon waveguides, with a group index very different from the effective index.

Temperature variations are mainly due to the variation of the refractive index in silicon and silica with respect to temperature. The two materials both have a positive thermo-optic coefficient, thus giving an increased effective index with higher temperature.

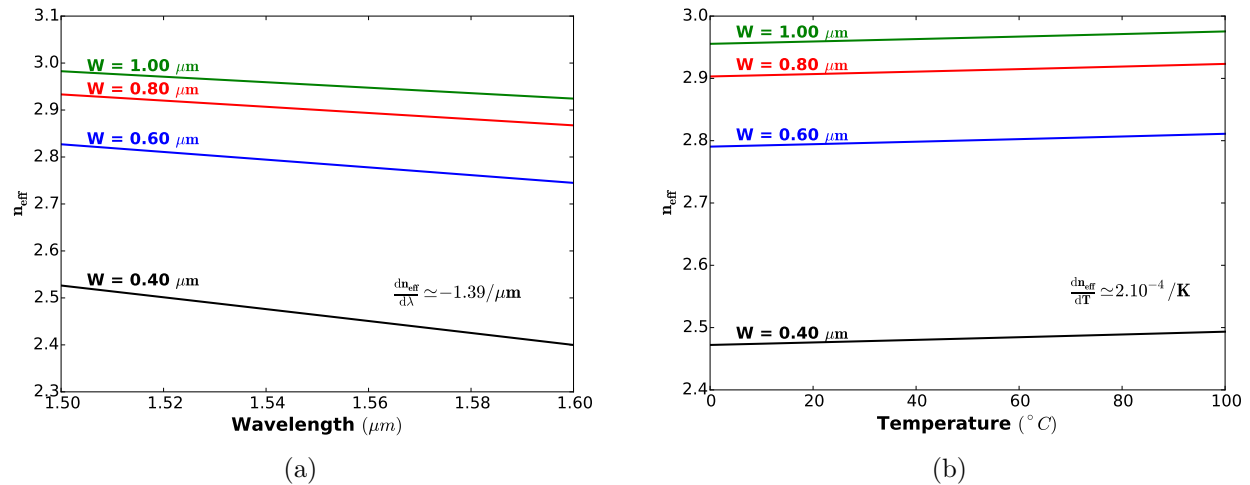


FIGURE 2.4: Variation of n_{eff} with (a) wavelength (b) temperature for TE^0 mode in a strip waveguide of width W and height 300nm

The variations with either wavelength or temperature are very smooth, almost linear. The slopes are measured to be $\frac{dn_{eff}}{d\lambda} \simeq -1.39/\mu m$ and $\frac{dn_{eff}}{dT} \simeq 2.10^{-4}/K$ for $W = 0.4\mu m$.

2.1.4 Rib waveguide characteristics

Rib waveguides have a lower confinement in the silicon than strip waveguides as the optical mode can be “at ease” in the slab region. The field at the interfaces is thus much lower, reducing losses due to interface imperfections. They are mostly used to propagate light across large distances ($typ > 1mm$) because of their relatively low propagation losses.

n_{eff} and n_g

Similar simulations can be made with a rib waveguide. Results are presented in figure 2.5. This guide has a height of 300nm and a slab thickness of 150nm. The main difference with the strip waveguide is the strong rejection of the TM^0 mode for widths lower than $1\mu m$

The TE^1 mode is cut below a width of $0.5\mu m$. The chosen width at $1.54\mu m$ is therefore $0.45\mu m$ for the single mode behaviour.

Wavelength and temperature variations can be simulated just as for the strip waveguide, with similar variations and conclusions. Values were obtained as follows : $\frac{dn_{eff}}{d\lambda} \simeq -0.75/\mu m$ and $\frac{dn_{eff}}{dT} \simeq 2.10^{-3}/K$.

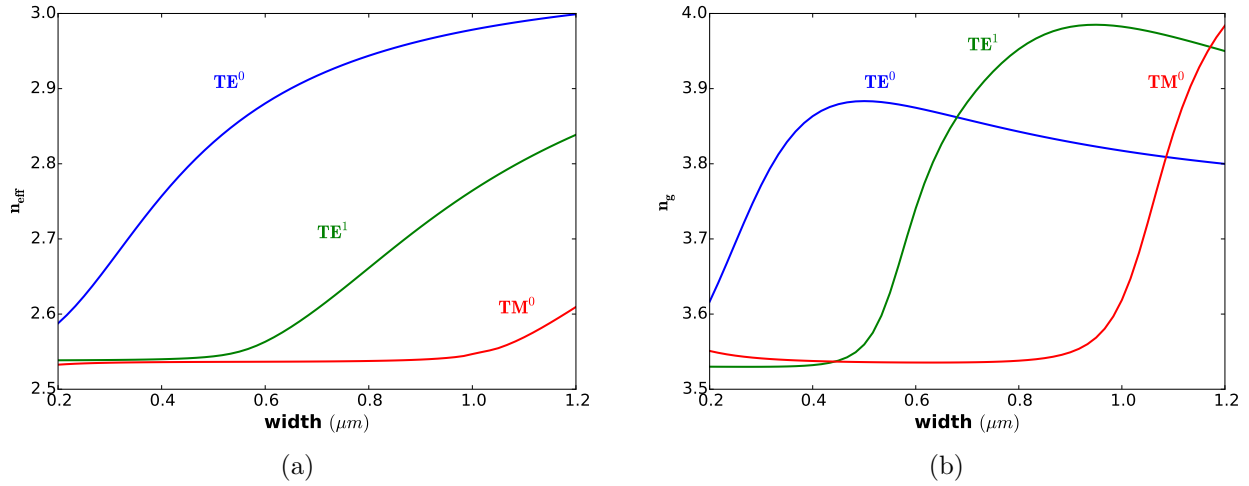


FIGURE 2.5: (a) Effective index (b) Group index of the 3 main modes in a rib 300-150 @1.54 as a function of width

But more interesting is the variation of n_{eff} with the slab height with guide height constant. The rib waveguide is very sensitive to that parameter, a change of 5 nanometers in thickness having repercussions on the second decimal. Moreover and contrary to variations with wavelength and temperature, the slope is also very dependant on the guide width. This specificity makes the rib waveguide much harder to get accurate performances, especially for applications that require a good control of the phase such as interferometers.

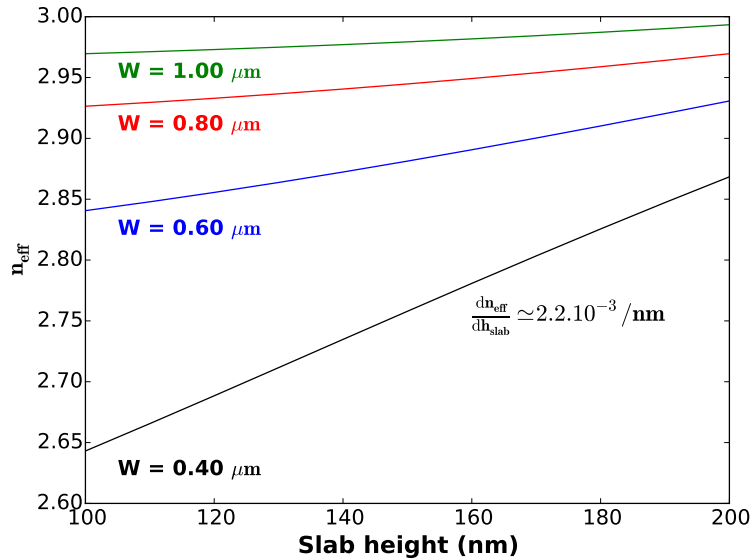


FIGURE 2.6: Variation of n_{eff} of TE^0 mode with slab height for a rib 300-150 W0.45 @1.54

2.1.5 Propagation losses

The propagation losses in an optical waveguide are mainly due to the roughness of the silicon-silica interface [5, 6]. The rugosity creates scattering, mode mismatch and reflections. The stronger the electric field amounts at the interface, the stronger the losses will be. There are thus two methods to reduce the losses. One can for instance deconfine the mode so as to lower the intensity of electric field at the interface. This is the method adopted by the rib waveguide. The drawback of a low-confined mode is its spatial extension and subsequent need for very large bend radius. The other way is to reduce the guide rugosity, but that can only be improved with better fabrication control.

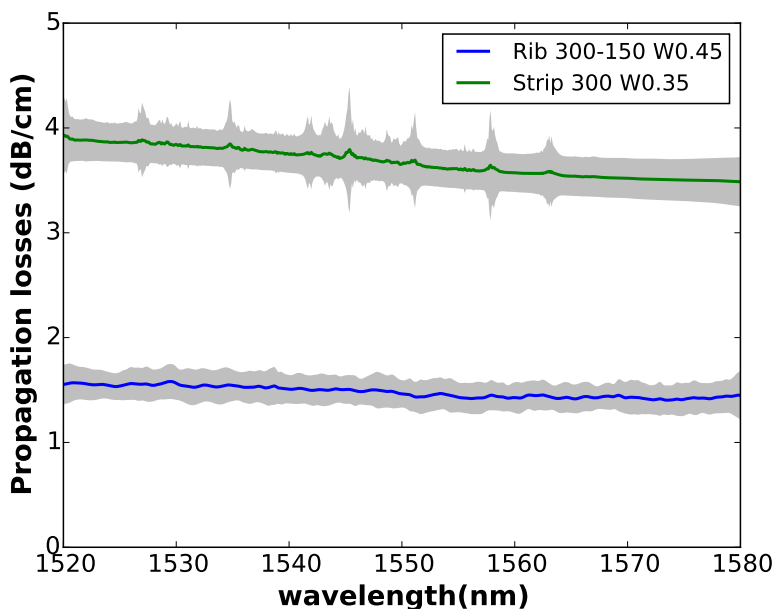


FIGURE 2.7: Measured propagation losses for a strip 220 W0.5 and a rib 220-100 W0.45 in the C-band averaged over 60dies. The grey area represent the standard deviation over the 60 dies.

Figure 2.7 shows the measured losses for a strip 250 W0.35 and a rib 300-150 W0.45 in the C-band. 60 dies from the same wafer were measured. The grey area represents the standard deviation observed for each wavelength. The measure for each guide follows these steps :

- Measure guides of various, large lengths (typ. $> 10mm$)
- Make a linear interpolation for each wavelength on the losses for different lengths. The slope gives the propagation losses.
- Get the mean value and standard deviation for each wavelength across the different measured dies. In this case, the statistic is made on 60 dies from the same wafer.

The propagation losses for the rib waveguide are, as expected, lower than for the strip waveguide, with an average value around 1.4dB/cm. They are also more stable with respect to wavelength. This can be explained by a very qualitative approach : the strip waveguide is more sensitive to wavelength, being completely confined. The mode has no choice but to adapt to the wavelength , thus modifying the field near the interface. Whereas in the rib, the mode can expand in the slab region to relax constraints.

2.2 Bend guides & bends

In the previous section, straight optical waveguides were analysed. This section will focus on guiding light in bends : what kind of bend is best depending on the size of the bend.

2.2.1 bend modes

When light goes through a bent section, the optical mode's profile changes. The mode is somehow "compressed" against the outer part of the guide, which causes it to leak power (radiative losses). For more theoretical background, see [7–9]. The less confined a mode is, the more it will be affected by the section's curvature.

The Fimmprop software [4] can simulate bend modes and extract the radiative losses. This simulation requires the implementation of Perfect Matched Layers (PML)[10] so that leaked radiation is absorbed and not reflected, as would be the case with a standard "Electric wall" border condition that is commonly used for other simulations.

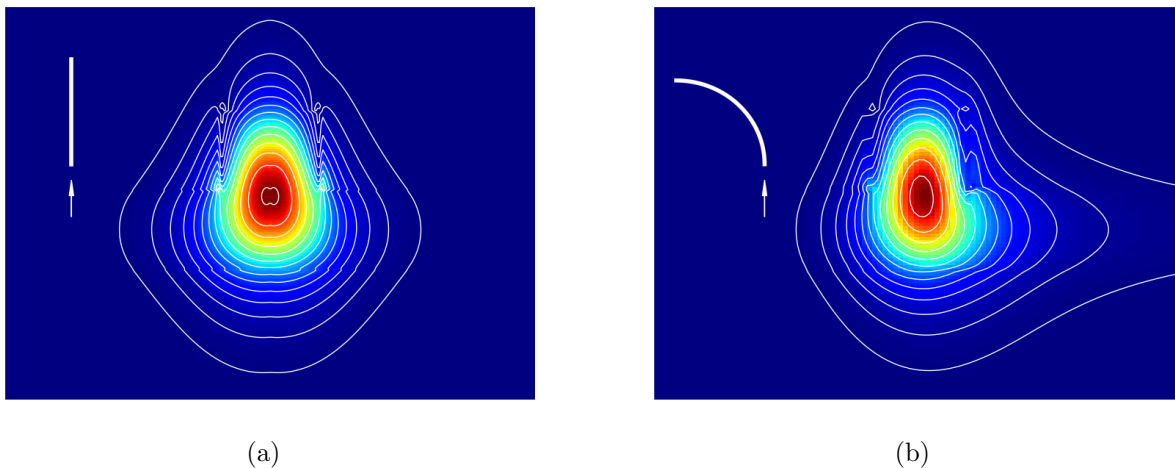


FIGURE 2.8: Intensity mode profile for (a) a straight rib 300-150 W0.45 @1.54 (b) a bent rib 300-150 W0.45 @1.54 with radius $R = 10\mu m$

Figure 2.8 the intensity profile in a straight guide and in a bend section. The curvature was chosen especially sharp in order to enhance the "compression" effect to make it clearly

visible. The field in the straight guide is completely symmetric whereas it is deformed in the bend guide

2.2.2 Different types of guides & their parametrisation

There are different shapes of bend that can be created. The aim of this section is to describe the different configurations and how they are parametrised, from the simple circular bend to the more complex clothoid bend. All bends will be normalised to have the same input and output as a $\pi/2$ arc-circle of radius R , so as to be replaced in the layout with minimum effort. The important parameters are the position and curvature κ , with the curvature defined as the reverse of the curve radius $\rho : \kappa = 1/\rho$. ρ can be expressed as a function of parametric coordinates $x(t), y(t)$ and their first and second derivative, respectively $x'(t), y'(t)$ and $x''(t), y''(t)$ [11] :

$$\rho(t) = \frac{(x'(t)^2 + y'(t)^2)^{3/2}}{x'(t).y''(t) - y'(t).x''(t)} \quad (2.6)$$

Circular bends

The circular bend is basically an arc-circle with the following parametric equation :

$$t \in [0, \pi/2] : \begin{cases} x(t) = R. \cos(t) \\ y(t) = R. \sin(t) \\ \rho(t) = R \end{cases} \quad (2.7)$$

For a circle, the curvature is a constant. Which means that there is a discontinuity in curvature when going from a straight waveguide to a circular bend.

Hyberbolic cosine bends

The hyberbolic bend uses a hyberbolic cosine as primitive form :

$$t \in [-s, s] : \begin{cases} x(t) = t \\ y(t) = \cosh(t) \end{cases} \quad (2.8)$$

With $s = \sinh^{-1}(1) = \ln(1 + \sqrt{2}) \simeq 0.88$

From the starting function 2.8, a rotation of $3.\pi/4$ is first applied with a rotation matrix :

$$\begin{pmatrix} \cos(\pi/4) & -\sin(\pi/4) \\ \sin(\pi/4) & \cos(\pi/4) \end{pmatrix} \cdot \begin{pmatrix} x(t) \\ y(t) \end{pmatrix} = \begin{pmatrix} -\frac{\sqrt{2}}{2} \cdot (t + \cosh(t)) \\ \frac{\sqrt{2}}{2} \cdot (t - \cosh(t)) \end{pmatrix} \quad (2.9)$$

The curve is then offset so that $x(t_{max}) = 0$ and $y(t_{min}) = 0$:

$$\begin{cases} x(t) = -\frac{\sqrt{2}}{2} \cdot (t + \cosh(t)) + offset_x \\ y(t) = \frac{\sqrt{2}}{2} \cdot (t - \cosh(t)) + offset_y \\ x(s) = 0 \\ y(-s) = 0 \end{cases} \quad (2.10)$$

$$\Rightarrow \begin{cases} x(t) = -\frac{\sqrt{2}}{2} \cdot (t + \cosh(t) - K) \\ y(t) = \frac{\sqrt{2}}{2} \cdot (t - \cosh(t) + K) \\ K = s + \sqrt{(2)} \end{cases} \quad (2.11)$$

The final step is to scale the curve so that all curves have the same initial and final position, with $x(t_{min}) = R$ and $y(t_{max}) = R$:

$$\begin{cases} x(t) = scale \cdot (-\frac{\sqrt{2}}{2} \cdot (t + \cosh(t)) + K) \\ y(t) = scale \cdot (\frac{\sqrt{2}}{2} \cdot (t - \cosh(t)) - K) \\ x(-s) = R \\ y(s) = R \end{cases} \quad (2.12)$$

The final parametric equation gives :

$$t \in [-s, s] : \begin{cases} x(t) = \frac{R}{2 \cdot s} \cdot (K - t - \cosh(t)) \\ y(t) = \frac{R}{2 \cdot s} \cdot (K + t - \cosh(t)) \\ \rho(t) = R \cdot \cosh(t)^2 \end{cases} \quad (2.13)$$

with :

$$\begin{cases} s = \sinh^{-1}(1) \simeq 0.88 \\ K = (s + \sqrt{(2)}) \end{cases} \quad (2.14)$$

The different steps explained above are presented in a schematic in figure 2.9. The processus explained above is the same for all the other types of bends : first rotation, then offset and finally rescaling.

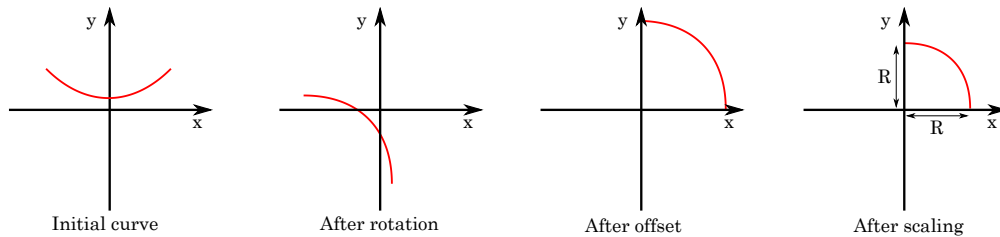


FIGURE 2.9: Schematic of the different operations applied to the hyperbolic cosine curve.

This bend is smoother than the circular bend, with a curvature equal to $\kappa = 0.5 \cdot R$ at the beginning of the bend, which is twice as low as for the circular bend.

Sine bends

The hyperbolic bend uses a sinus as primitive form :

$$t \in [0, \pi] : \begin{cases} x(t) = t \\ y(t) = \sin(t) \end{cases} \quad (2.15)$$

Which gives after a rotation of $-\pi/4$, offset and rescaling :

$$t \in [0, \pi] : \begin{cases} x(t) = R \cdot \frac{1+\cos(t)}{\pi} \\ y(t) = R \cdot \left(\frac{-1+\cos(t)}{\pi} + 1 \right) \\ \rho(t) = -R \cdot \frac{\sqrt{2}}{\pi} \cdot \frac{(1+\cos(t))^2}{\sin(t)} \end{cases} \quad (2.16)$$

This function is of \mathcal{C}^∞ class and has a null curvature at the beginning. As such, it has to be the smoothest function among all the studied shapes. On the other hand, the maximum curvature of $\kappa \simeq 2.3$ is very high, which can create larger radiative losses.

Clothoid bends

A clothoid is a curve parametrised through an integral

$$\begin{cases} x(t) = k \cdot \int_0^t \cos(u^2) \cdot du \\ y(t) = k \cdot \int_0^t \sin(u^2) \cdot du \end{cases} \quad (2.17)$$

Its specificity is that the curvature is proportional to the curve absciss, thus null for $t = 0$. The full bend is obtained by taking this function for half the 90° bend, and making a mirror image. The final clothoid bend has the following parametric expression :

$$t \in [0, t_c] : \begin{cases} x(t) = R \cdot \left(1 - a \cdot \int_0^t \cos(u^2) \cdot du \right) \\ y(t) = R \cdot \left(a \cdot \int_0^t \sin(u^2) \cdot du \right) \\ \rho(t) = \frac{a}{2 \cdot t} \end{cases}$$

$$t \in [t_c, 2 \cdot t_c] : \begin{cases} x(t) = R \cdot \left(a \cdot \int_0^{\tilde{t}} \cos(u^2) \cdot du \right) \\ y(t) = R \cdot \left(1 - a \cdot \int_0^{\tilde{t}} \sin(u^2) \cdot du \right) \\ \rho(t) = \frac{a}{2 \cdot \tilde{t}} \\ \tilde{t} = 2 \cdot t_c - t \end{cases} \quad (2.18)$$

With :

$$t_c = \text{sqr}t(\pi)/2$$

$$a = \left[\int_0^{t_c} \sin(u^2) du + \int_0^{t_c} \cos(u^2) du \right]^{-1}$$

The various shapes and curvatures for a bend size $R = 1$ are displayed in figure 2.10. The definition interval of the bend was shifted to fit in the $[0, 1]$ interval.

The bends can be separated in two groups : the ones with a discontinuity in curvature at t_{min} and t_{max} , namely the circular and cosh bend, and the ones without, the sine and

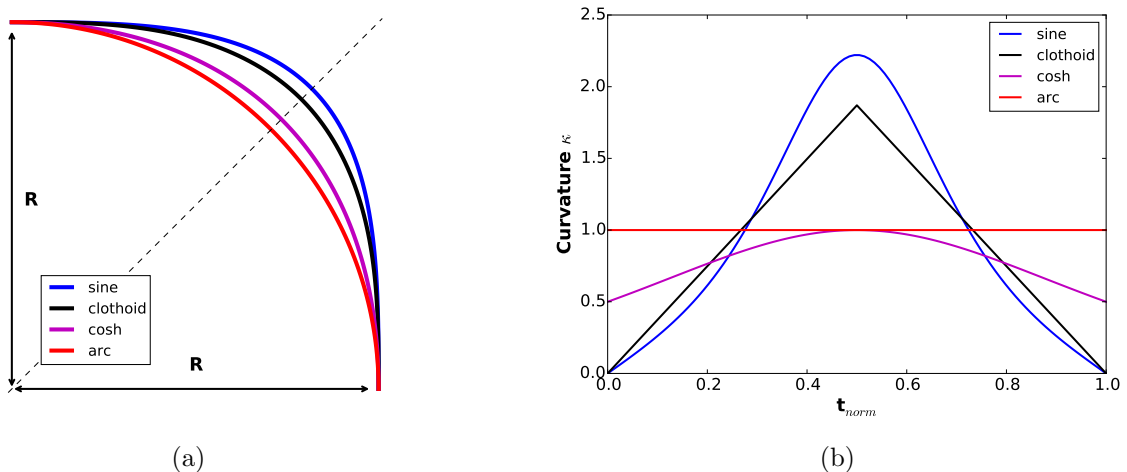


FIGURE 2.10: (a) aspect of the different bends (b) Curvature for different bends with radius $R = 1$. The parameter t was rescaled for each bend to fit it in the $[0, 1]$ window

clothoid bend. The ones with discontinuity will suffer from transition losses between a straight waveguide and the bend. On the other hand, the ones without discontinuity have a maximum curvature radius greater than that of a simple circle, which can cause much higher radiative losses. From this simple reasoning, we can expect that there will be a trade-off between radiative loss and transition loss.

2.2.3 Simulation setup

In order to simulate the losses for each of these bends, two different simulations were performed. One simple 2D simulation with only radiative losses and one 3D propagation simulation that includes curvature variations and transition losses.

2D fimmwave structure

The first simulation is simply a 2D fimmwave structure with PML boundaries with the bend radius parameter set to the right value. From this simulation, we get the lineic radiative losses coefficient α . The loss per bend can then be extracted with the following formula :

$$Loss \text{ per bend } [dB] = -10 \cdot \log_{10}(e^{-\alpha \cdot (\frac{\pi}{2} \cdot R)}) \simeq -6.81 \cdot \alpha \cdot R \quad (2.19)$$

3D fimmprop structure

The fimmprop software is unable to simulate a bend with a continuously varying curvature. The bend was discretised in multiple circular bend sections with a different curvature for each section, starting and ending with a straight guide. There is one notable exception

with the circular guide which needs only 3 sections, one for the bend and two for the straight sections. An example of layout for the sinus guide is displayed in figure 2.11.

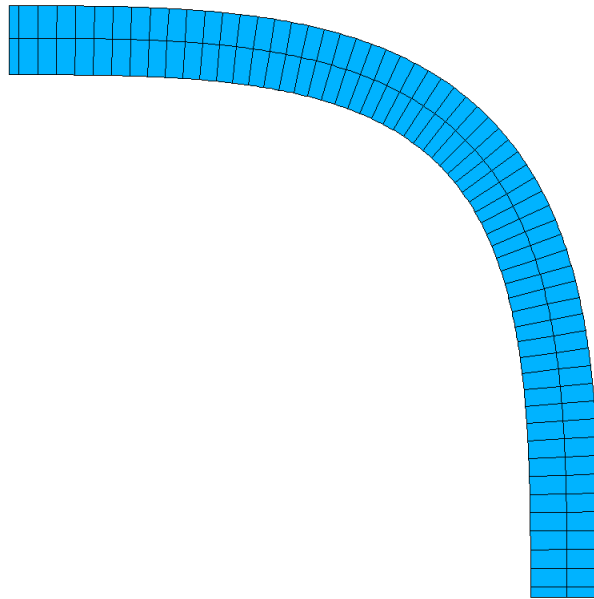


FIGURE 2.11: Layout of the fimmprop simulation with different sections highlighted for a sine bend

A stability study was made to determine the necessary conditions for the simulation to be accurate. Simulations were made to determine the minimum number of sections and the minimum number of points that are required to stabilise the simulation. The results are presented in figure 2.12. The simulation is stable and accurate for a number of sections greater than 60 and a number of points greater than 300.

2.2.4 Simulation results

One of the interesting curves in that kind of simulation is the variation of the power coupled in the fundamental mode as the light propagates from one end of the bend to the other. The slope gives an estimation of where the losses are the largest. These profiles are displayed in figure 2.13 for a circular bend and for a sine bend.

The profile for the circular bend presents a heavy drop at the transition with a low, constant radiative loss in between. On the other hand, the sine curve present no transition losses, as expected, but suffers from high radiative losses, especially at the sharpest curvature, at the center of the bend. The two bends were intentionally chosen with small radii in order to emphasize the loss effect while remaining in a stable simulation.

Simulations for each bend and for various radii were performed. The aggregated results are presented in figure 2.14 with the pure radiative losses also displayed for reference purpose.

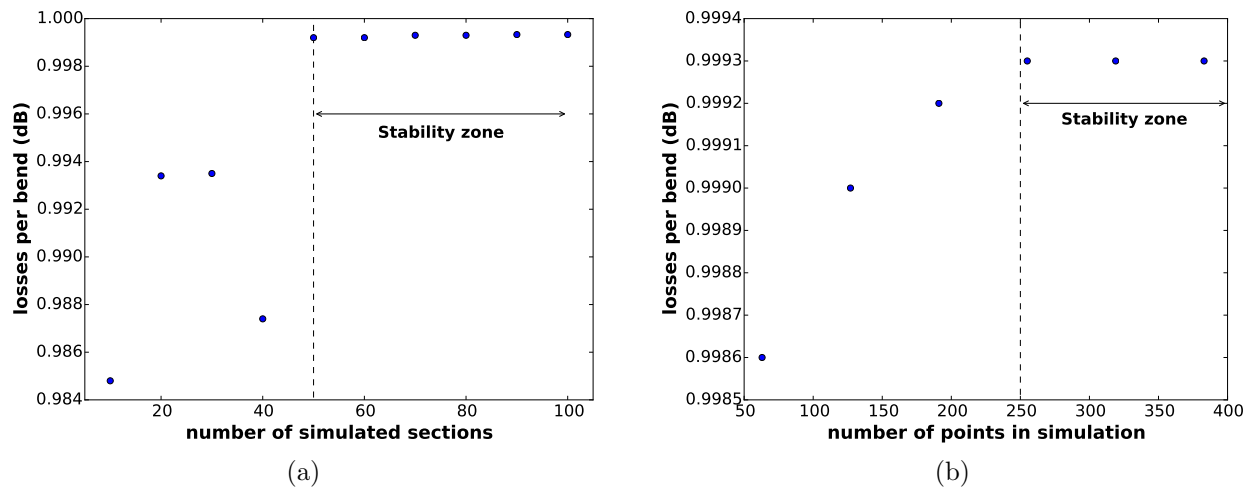


FIGURE 2.12: Convergence study for (a) The number of sections (b) The number of points in section

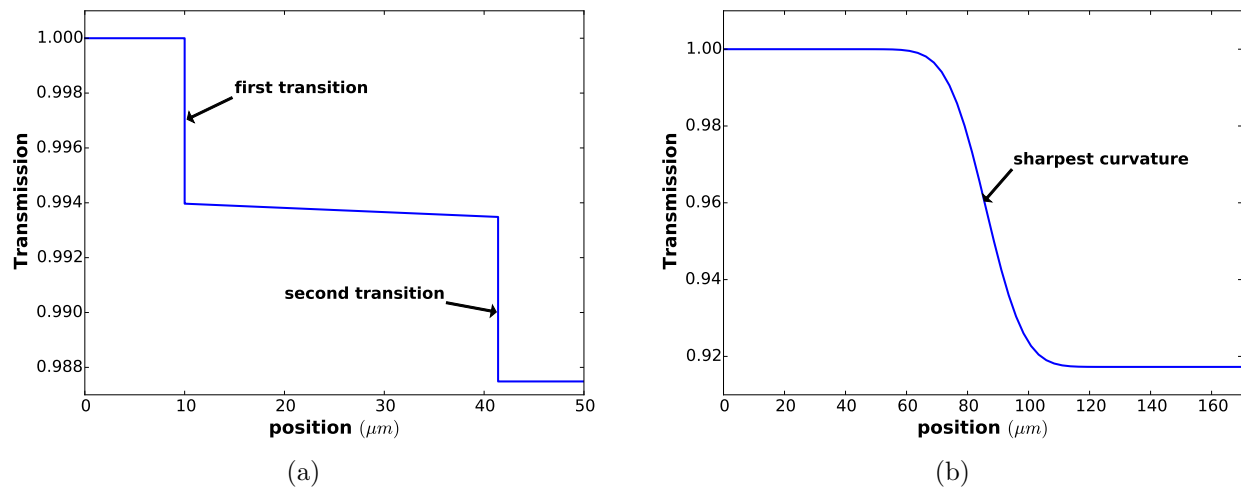


FIGURE 2.13: Power in the fundamental mode for (a) a circular bend rib 300-150 R20 W0.45 (b) a sine bend rib 500-300 R100 W0.55

The pure radiative represent the losses for a circular bend with no transition losses. The figure represents the loss per bend in function of the bend size as described in figure 2.10a.

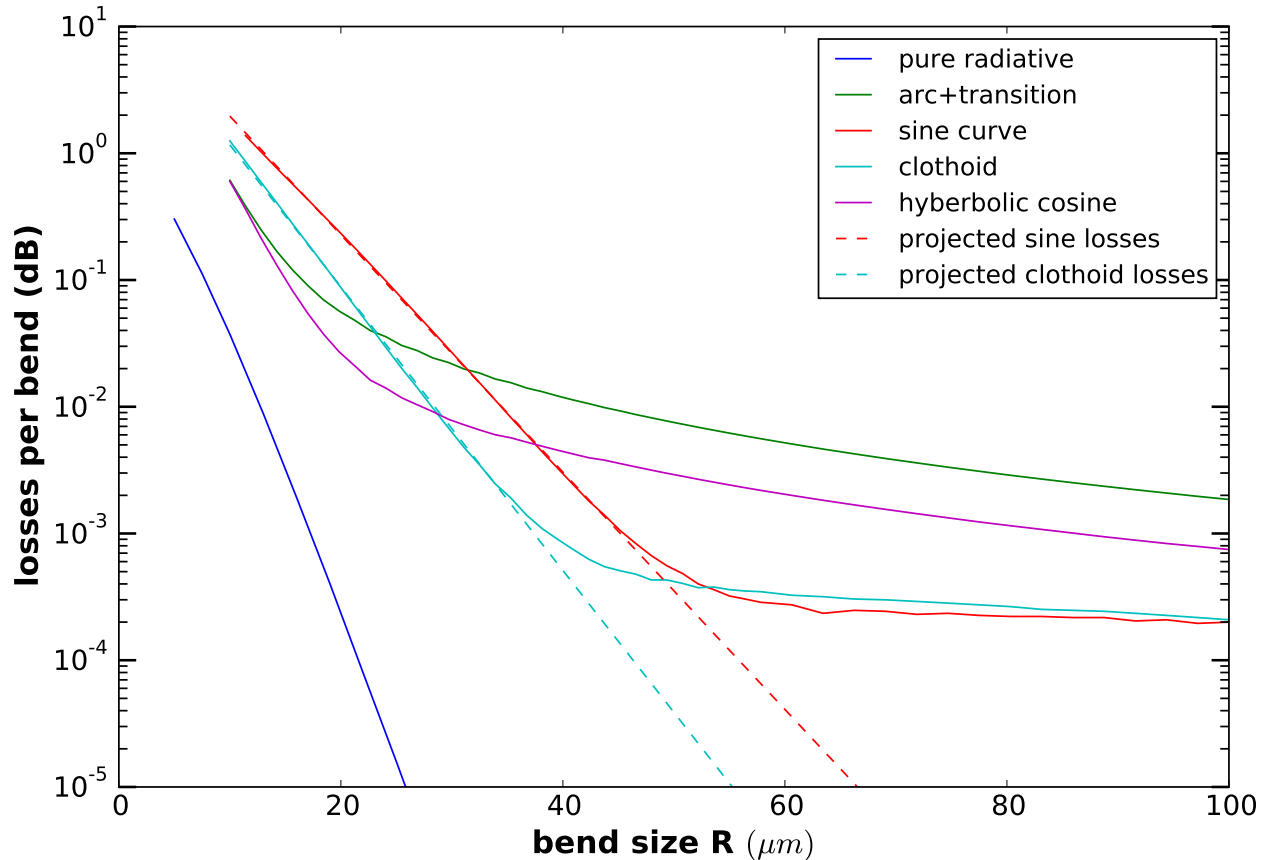


FIGURE 2.14: Losses for different bends in function of radius for a rib 300-150 W0.45 @1.54

Two groups of bends can be distinguished. The circular and the cosh bend on one side, the clothoid and the sine bend on the other side. The circular and cosh bends have a similar behaviour : their losses are dominated by radiative losses for small sizes but the transition losses become greater at larger sizes. The slope for large size is very small, which means that taking a large size has little effect on the losses. Also to be noted is that the cosh bend is always better than the circular bend. Indeed, the cosh bend has a transition twice as smooth as the arc and keeps a curvature always lower. It is therefore always advantageous to use a cosh in place of an arc circle.

The sine and clothoid bend have a similar behaviour but very different from the previous group. Both present a floor for large radius, but this floor is an artifact of simulation and not physical. The accumulated error across the numerous sections is precisely equal to the loss value in that floor. The correct physical losses are the ones interpolated from the losses at low radius as shown with the dashed curves. There are no transition losses as for the previous group. The losses are dominated only by the radiative part. The sine bend has a lower slope than the clothoid bend, which is in turn lower than the pure radiative. This is

due to their respective maximum curvature : a low curvature will make a steeper slope, and the sine bend has the largest one. Because of that, clothoid and sine bend have higher losses than the cosh bend for smaller sizes.

A similar simulation was performed on a strip 220 W0.45 with a circular bend, including transitions. The results are displayed in figure 2.15. The behaviour is very similar to the circular bend with a rib waveguide but the size of the bend is much smaller. The strip bend has acceptable losses down to a size smaller than $5\mu m$

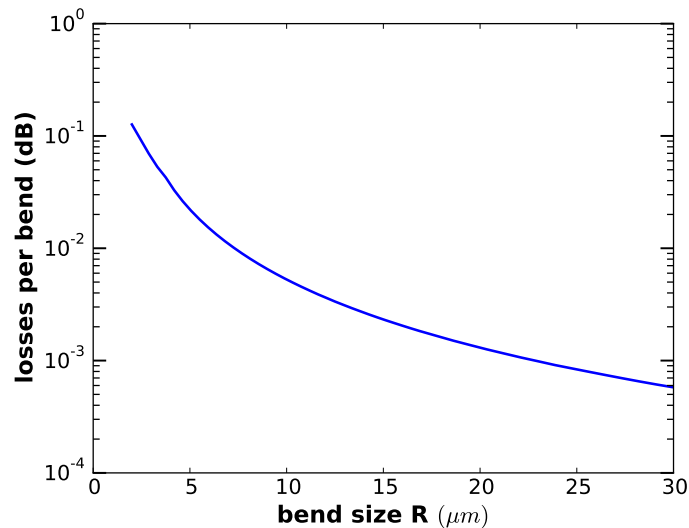


FIGURE 2.15: Simulated bend loss for a strip 220 W0.45 circular bend with transitions

In conclusion, depending on the maximum practical radius and the maximum acceptable losses, the bend to choose will be either a cosh bend (for $R < 30\mu m$) or a clothoid bend (for $R > 30\mu m$).

2.2.5 Experimental results

Measures were made on bends that were designed before these simulations were implemented. The results in the C-band and in the O-band are presented in figure 2.16. Due to the variety of implemented designs, a different approach was used in each case.

The arc circle R50 rib 220-100 W=0.4 sample consists of a structure with 204 circular bends of 90° . The measured spectrum was normalised by FGC and then divided by 204. The simulation losses are approximately 3-4 times lower than experimental losses. Two different effects were identified that could explain that gap. The first is that the simulation doesn't take into account the linear propagation losses due to waveguide roughness. The other effect could be responsible for the "wave" shape of the curve : part of the optical power lost in the bend could be re-injected in the waveguide after a reflection against an interface. A simulation was able to reproduce that shape by having mirrors instead of PML as simulation

boundary.

For the Clothoid R56 rib 500-300 $W=0.56$, several very long guides with the same length but with a different number of bends were measured. A linear interpolation was made for each wavelength as a function of the number of bends in order to extract the loss per bend at that wavelength. The signal at the output was very weak and noisy due to the high losses at each bend ($\approx 1\text{dB}/\text{bend}$). The measured value is very close to the one predicted by simulation.

For the Arc circle R20 rib 300-150 $W=0.35$ in the O-band, three samples were measured with respectively 16,32 and 48 turns. Due to the high losses for each bend, the spectrum was very noisy. An averaged spectrum was made for each of the three samples. A linear interpolation was then made on the losses as a function of the number of turns. The slope extracted for each wavelength gives the curve in figure 2.16b. The simulation losses are about two times lower than the experimental ones.

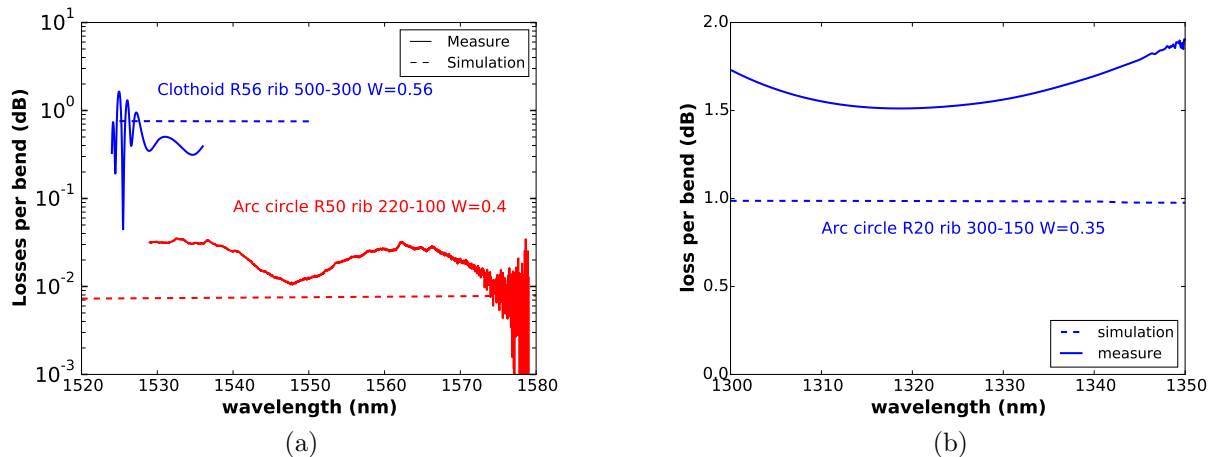


FIGURE 2.16: Measured bend losses (a) in the C-band (b) in the O-band

Measurements were also performed with $50\mu\text{m}$ clothoid and 30μ cosh bends with a rib 300-150 $W0.45$ geometry. But the bend losses were much lower than the standard propagation losses. As a result, the bend loss signal is lost in the noise from the propagation losses and could not be extracted. But the conclusion remains good : the shape of the bends is good enough for the bend loss to be meaningless in front of other losses.

2.3 Periodic structures

Periodic structures can be etched in a silicon waveguide, leading to reflections and interferences. These structures can be tuned to realise various functions. The most commonly used devices are the Bragg grating and the Fiber Grating Coupler (FGC)

2.3.1 Bragg Gratings

A Bragg grating is a periodical change of the effective index in the propagation region, in other words a periodical alternance of low and high index propagation regions. This alternance creates reflexions, and the periodicity produces well defined interferences at specific wavelengths. Such a device is often used to create mirrors.

The reflectivity can be expressed, for a uniform Bragg grating of the 1^{rst} order for small Δn as [12, 13] :

$$r = \frac{-\kappa \cdot \sinh(\alpha \cdot L)}{\alpha \cdot \cosh(\alpha \cdot L) - i \cdot \delta \cdot \sinh(\alpha \cdot L)} \quad (2.20)$$

with :

$$\alpha = \sqrt{\kappa^2 - \delta^2} \quad (2.21)$$

$$\kappa = \frac{\pi}{\lambda} \cdot \Delta n_{eff} \quad (2.22)$$

$$\delta = 2 \cdot \pi \cdot n_{eff} \cdot \left(\frac{1}{\lambda} - \frac{1}{\lambda_D} \right) \quad (2.23)$$

where Δn_{eff} is the index modulation amplitude, n_{eff} the average effective index over a period and $\lambda_D = 2 \cdot n_{eff} \cdot \Lambda$ the "design" wavelength and Λ , the grating period.

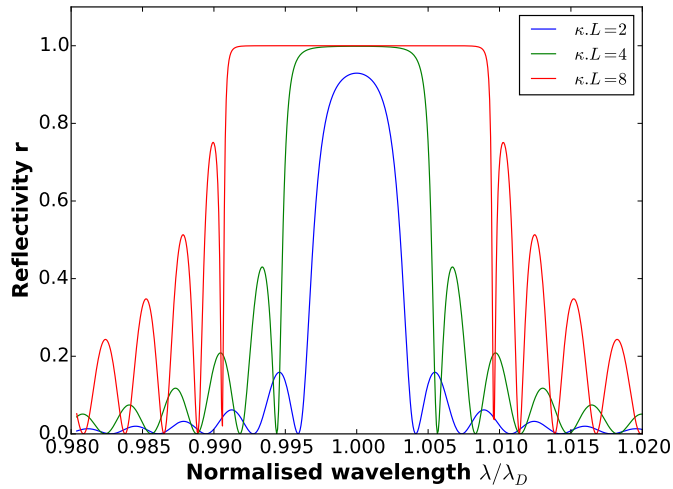


FIGURE 2.17: Simulated reflectivity of a bragg grating in function of normalised wavelength for various $\kappa \cdot L$ product, with L constant.

Figure 2.17 gives the simulated reflectivity of a Bragg mirror in function of normalised wavelength $\frac{\lambda}{\lambda_D}$ for various values of $\kappa \cdot L$ with L set as a constant.

2.3.2 Fiber Grating Coupler

Fiber grating couplers (FGC) are a very important building block : they are used to couple light from the silicon wafer to a vertically mounted fiber as demonstrated previously in figure 1.11b. They are based on a Bragg grating with a period designed to have constructive interferences at a specific angle, thus extracting light out of the silicon plane. The base relation for these couplers is the following :

$$n_{eff} = n_{top} \cdot \sin \theta_c + m \cdot \frac{\lambda}{\Lambda} \quad (2.24)$$

with n_{eff} the average effective index of the grating, n_{top} the refractive index of the material in the free propagation region (typ. air), Λ the grating period and m the diffraction order of the grating. θ_c is the angle, with the vertical as reference, at which the light at wavelength λ is emitted.

Figure 2.18a and 2.18b shows the insertion losses of respectively 1D and 2D FGC versus wavelength.

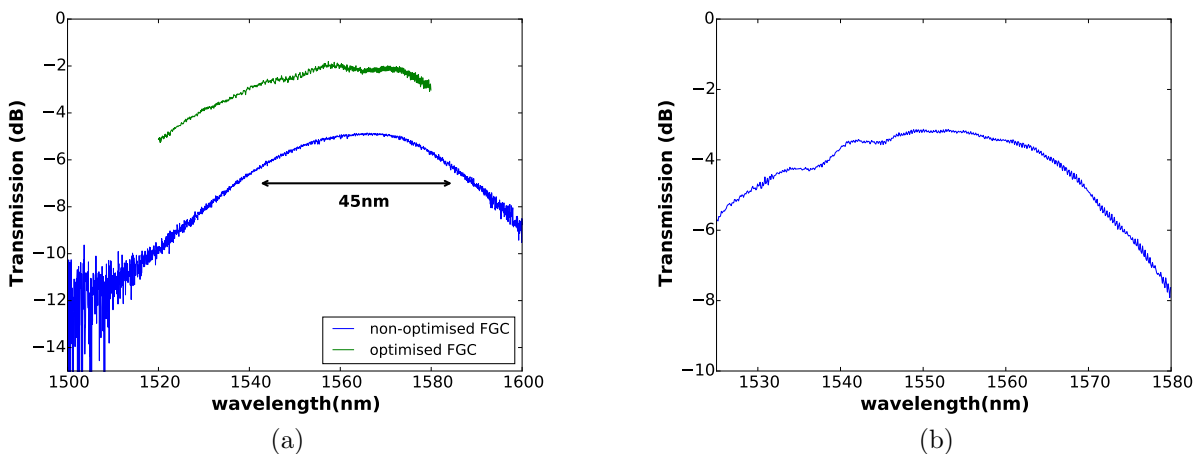


FIGURE 2.18: (a) Measured spectrum of 1D fiber grating couplers (b) Measured spectrum of a 2D fiber grating coupler

The FGC used in most designs throughout this thesis is not optimal because they are from an older conception, with minimum insertion losses around 5dB per coupler. Optimisations were realised in parallel with our work at Leti. The most recent FGC exhibit, when properly measured, minimum losses lower than 2dB. The 3dB bandwidth for both FGC is around 45nm. The 2D coupler have higher losses, around 3.5dB for the optimised coupler.

The optimisation process of the FGC was made with several variables tuning. The most important effects are :

- the thickness of the buried oxide layer
- the coupler's geometry with an apodisation of the grating

- Measurements made with a fiber cleaved at 10° in order to have the fiber as close to the sample as possible

In addition to the relatively high losses, FGC have a reflectivity around 1%, which can be problematic for reflection-sensitive devices such as SOA.

2.4 Waveguide crossings

Most integrated circuits have a simple path from a set of points to another and don't require waveguides to cross. But some are more complex and have some topology issues. Contrary to electronics, routing light on different levels can be very challenging. On the other hand, waveguides crossings can be efficient with limited crosstalk [1]. The main difficulty in such a device is to tailor the mode profile at the crossing so that the losses are the lowest possible with a minimal crosstalk on the other waveguides. People have tried to do it with the help of MMI [14], but the most straightforward solution remains to have a simple crossing with a rib waveguide. Figure 2.19 gives a schematic of such a crossing. The light is injected at the input side and must be coupled to the through waveguide with smallest possible coupling to the cross waveguide.

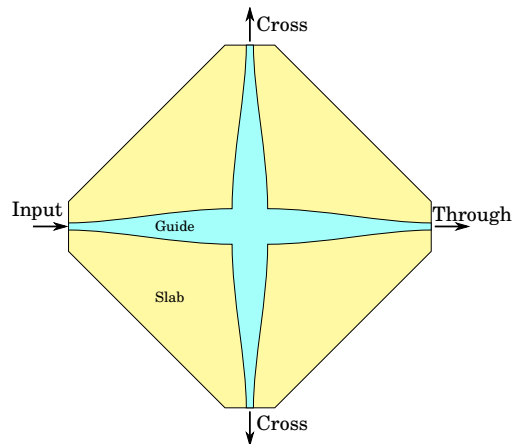


FIGURE 2.19: Schematic of a waveguide crossing

In crossings, a guide with low confinement is more likely to propagate unperturbed by the crossing and therefore have low insertion losses. A low-confinement waveguide will extend over a very large area. The diffraction experienced at the crossing will therefore be limited compared to a highly-confined mode. With a limited diffraction, the mode shape will be very similar before and after the crossing and will therefore re-couple without trouble to the through waveguide. This is the reason why rib, and preferably very shallow rib, are used instead of strip waveguides in the design of crossings.

In order to optimise the insertion losses, different profiles were tested for the taper in the crossing. The two most efficient ones were found to be a linear taper and an S-shaped taper. The two configurations were simulated with Fimmprop [4]. The length and width of each

taper were optimised to get the lowest possible insertion losses with a reasonable footprint. Figure 2.20 shows the intensity profile through the crossing for the linear taper and S-shaped taper with respective simulated transmission at $1.54\mu m$. The S-shaped taper has a width that can be expressed as :

$$W(l) = W_0 \cdot (1 - \sin^2(\frac{\pi}{4} \cdot \frac{l}{L_{max}})) + W_{L_{max}} \cdot \sin^2(\frac{\pi}{4} \cdot \frac{l}{L_{max}}) , l \in [0, L_{max}] \quad (2.25)$$

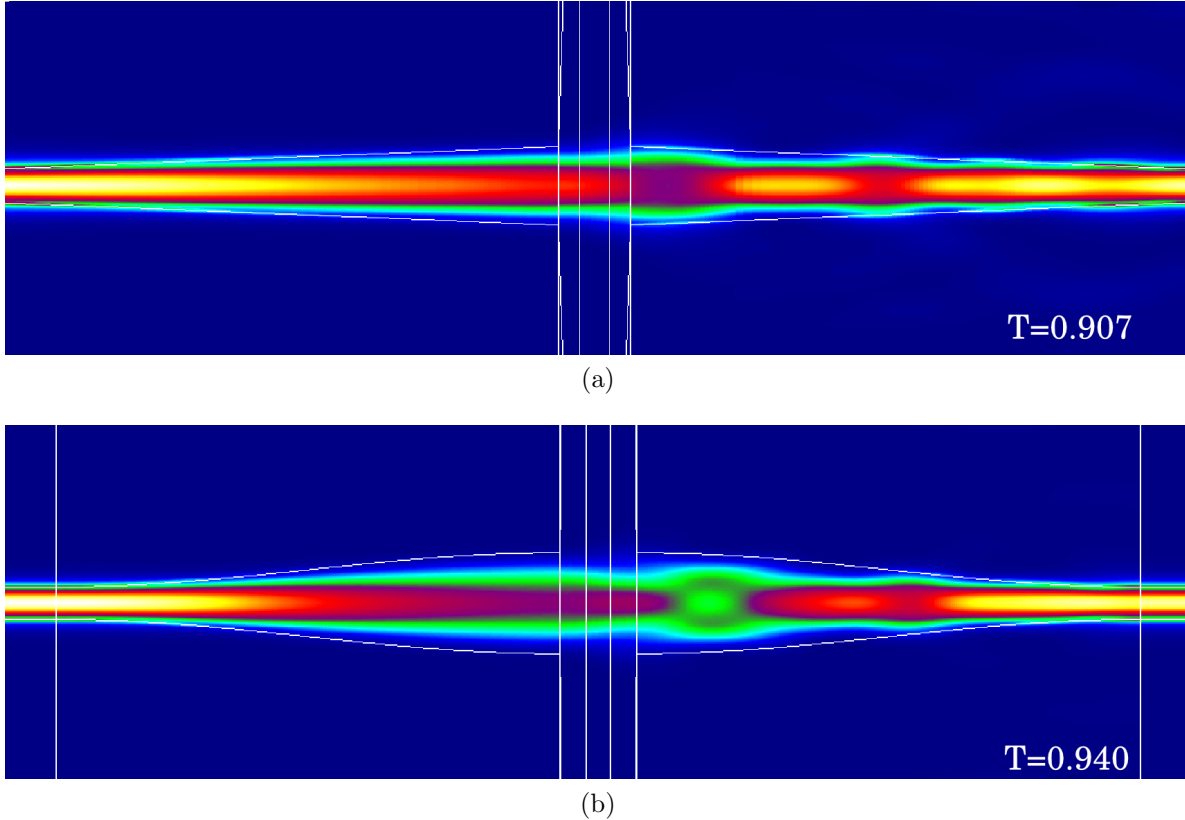


FIGURE 2.20: Simulated intensity profile across (a) a linear taper crossing (b) a S-shaped taper crossing

According to simulation, the S-shaped taper is always better than the linear taper. It is interesting to note that the tapers are quite large at the end ($1.4\mu m$). With such a large guide, diffraction is less important than with a smaller guide. On the other hand, higher order modes are excited, which can lead to extra-losses.

Devices were measured around $1.54\mu m$. The results are shown in figure 2.21. The samples were made of 30 cascaded crossings. The resultant spectrum was normalised by the vertical grating coupler's spectrum and then divided by 30 to get the losses per crossing. Light was injected in the device with an EDFA. The relatively low source power level combined with a very good crosstalk of the sample makes it impossible to measure a crosstalk spectrum above the OSA noise level. A power difference between the through port and the cross port was

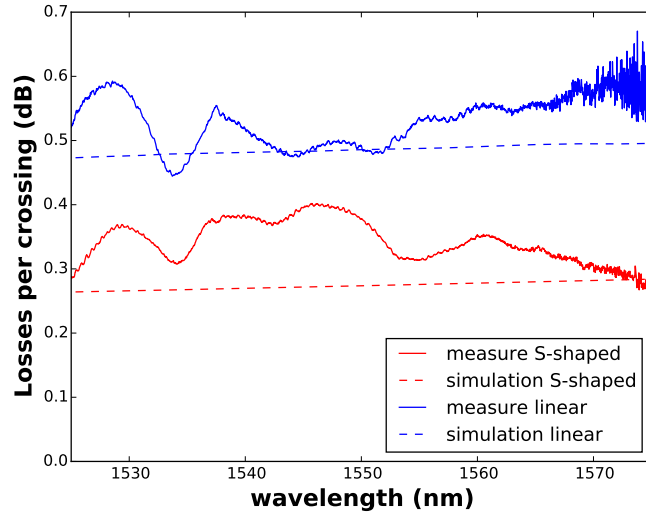


FIGURE 2.21: Simulated and measured losses for the linear taper and S-shaped taper with a rib 300-150nm geometry

however measured greater than 40dB for both the linear and S-shaped tapers. The S-shaped taper is always found to be better than the linear taper on insertion losses and similar in crosstalk, as was expected from the simulation. The S-shaped taper will therefore be used where a crossing is required.

The best measured losses for the S-shaped crossing are around 0.3 dB/crossing. They are still higher than the 0.2 dB/crossing reported in [1]. This can be explained : the ribs presented here are rib 300-150 whereas the ones used in the publication are rib 220-150. The last one is shallower than the one depicted here. The modes are therefore less confined and will be less affected by the crossing, and thus have lower insertion losses.

The simulated wavelength dependency was added to the plot and fit well with the measurement. The simulation is therefore accurate enough to predict losses in crossings and could be used to further optimise the taper profile.

2.5 Power splitter

Power splitters are an essential building blocks in any photonic circuit. They split the light into different waveguides with the desired power repartition. These are used for instance in the creation of interferometers such as Mach-Zender interferometers (see section 2.7). The most common designs of power splitters are the Y-junction [15] (or similarly the X-junction), multimode interferometers (MMI) and directional couplers (DC). In this thesis, only MMI and DC are studied. Each of these designs have their own characteristics that make them more suitable for some applications than for others.

2.5.1 Multimode Interferometer

The multimode interferometer takes advantage of a very large propagation section that can sustain multiple modes and not only the TE^0 mode as is the case for a normal waveguide. Each of these modes propagates at a different velocity. There exists a relation between the effective index of all the modes. This specific configuration can refocalise an input image after a certain length into one of multiple self images [16] as described in figure 2.22.

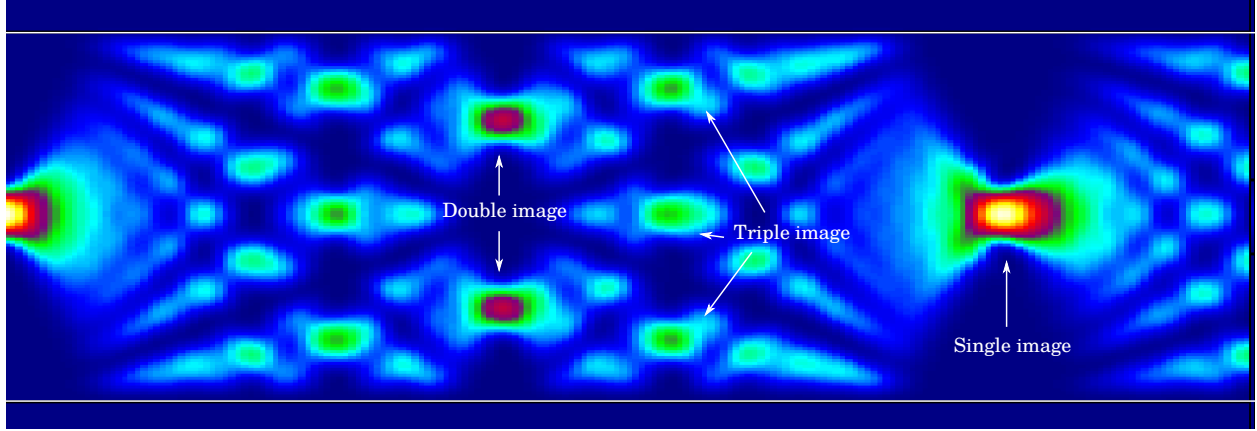


FIGURE 2.22: Self imaging in a multimode interferometer

The length of self imaging depends on the slab index of the MMI and its width. For a $N \times N$ MMI, the shortest theoretical coupling length is [17] :

$$L = \frac{1}{N} \cdot 3 \cdot L_c \quad (2.26)$$

with

$$L_c = \frac{\pi}{(\beta_0 - \beta_1)} \simeq \frac{4}{3} \cdot n_s \cdot \frac{W_{eq}^2}{\lambda} \quad (2.27)$$

Where β_0 and β_1 are the propagation constant for the first two modes. For more details on the calculations, please refer to [17]. In the case of strong guiding such as here, $W_{eq} \simeq W$ with W the MMI width.

In this section, a 2X2 MMI will be studied. The notations are described in figure 2.23. W_i/n corresponds to the width of the input/output guides and offset to their position.

The most used configuration throughout this thesis is the 2X2 geometry used as a 3dB power splitter. We could use a 1X2 MMI for that purpose, but this configuration was preferred because of its additional input/output. With it, we can have an auxiliary input/output on all designs. It can then be used for testing or monitoring purposes.

The intensity field across the device as simulated by the fimprop software is presented in figure 2.24. The MMI has a width of $5\mu m$ for a length of $104\mu m$. As expected, the input guide is imaged twice after a predetermined distance. The input and output widths are designed to optimise the overlap with the free propagation region. The optimal offset position is set by the theory, but its position was nonetheless optimised by simulation.

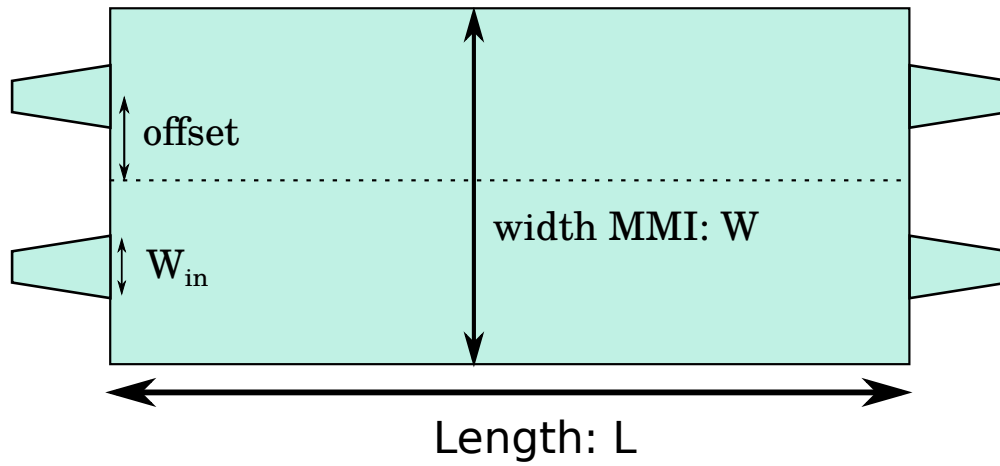


FIGURE 2.23: Schematic of a 2X2 MMI

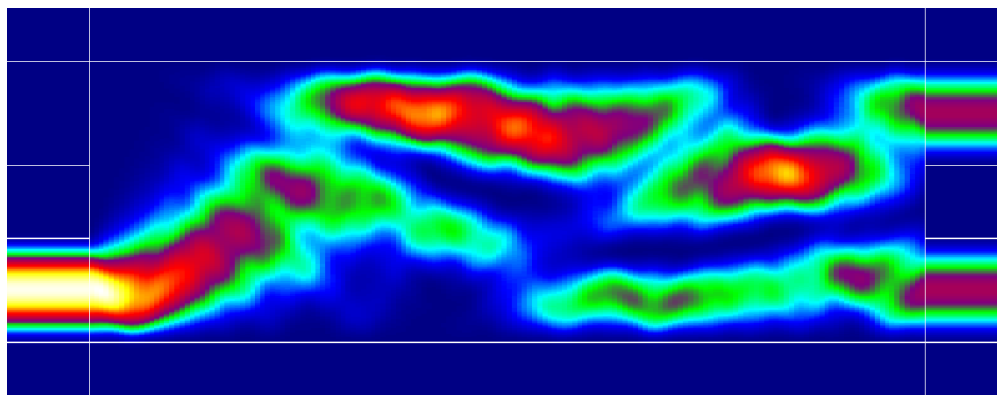


FIGURE 2.24: Intensity repartition in a 2X2 MMI at $1.5\mu m$

Tapering the input/output waveguides in the layout is necessary in order to adapt the guide from the single mode behaviour to the large waveguide that enters the MMI. Its effect was studied in simulation and proven to have limited impact on the final results. Therefore all following simulations were made with straight waveguides at input/output.

One of the primary goal of a power splitter is to be wavelength-resilient and, in this specific case, as perfectly balanced as possible. A wavelength scan was performed with the transmitted power as monitored variable. Results are displayed in figure 2.25. The insertion losses for this device are lowest at the optimised wavelength around $1.54\mu m$. The power balance is usually good on the whole window with only a few percent difference in power between the two channels. The insertion losses on the other hand tend to be higher far from the optimised wavelength, with as much as 10% power loss at the extremity of the simulated wavelength range.

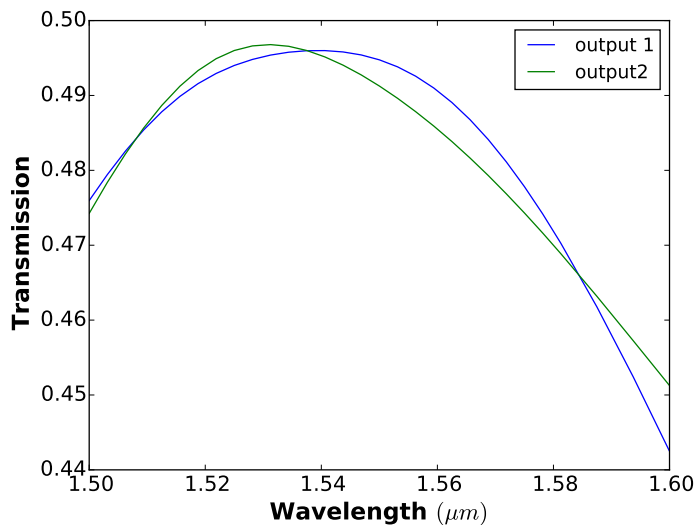


FIGURE 2.25: Simulated transmission coefficient as a function of wavelength for the two outputs of a 2X2 MMI

Figure 2.24 shows the results when light comes from one input and is split to two waveguides. But the reverse case with coherent light injected at both inputs must also be studied. The case where the two signals are in phase is simple : light will be split equally between the two outputs (see Fig. 2.26a). The case where the two signals are in phase quadrature is more interesting as the light will couple to only one of the output (see Fig. 2.26b). This comes from the fact that the MMI creates a $\pi/2$ dephasing between the two outputs.

A MMI similar to the one described here was fabricated and measured with a silicon thickness of 220nm with a width of $7\mu m$ and a length of $61\mu m$ (see Fig. 2.27). The device has higher losses than expected by the simulation, but the power balance remains very good with a relative imbalance better than 5% in transmission. The minimum in imbalance is around $1.52\mu m$ compared to the simulated $1.54\mu m$. The spectrum also shows long period oscillations with a relatively high amplitude. This ripple is caused by reflections with a typical

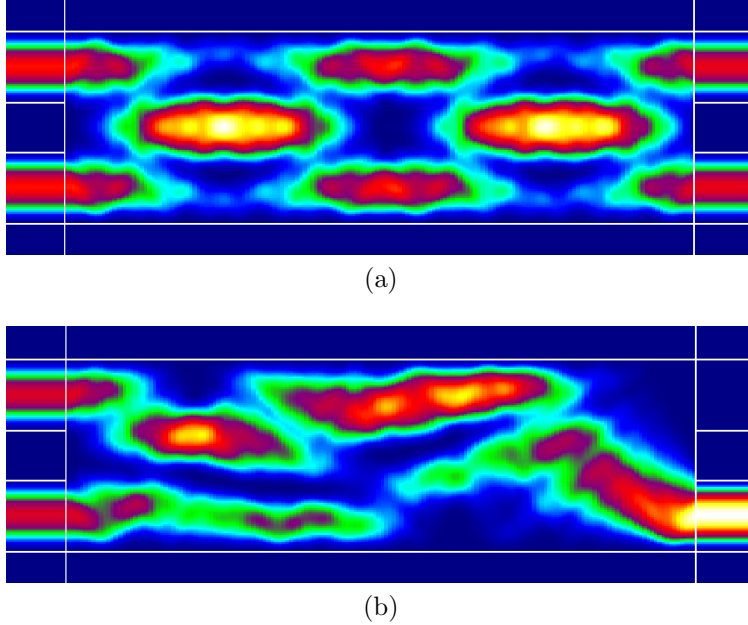


FIGURE 2.26: Intensity repartition across the MMI when (a) both input have the same phase (b) inputs are in phase quadrature

length of $L_{cav} \simeq 50\mu m$, which coincides with the MMI length. We can thus deduce that the device has an internal reflectivity of about 3–5%. This reflectivity is quite high and could be the cause of an important feedback susceptible to perturbate reflection-sensitive components such as SOA. A more sophisticated simulation with smooth transition from waveguide to optimal width could help to mitigate this problem [18]. Simulated power was added to the plot. For this simulation, the guide height was adjusted to fit the measurement and extra-losses were artificially added to reach the same power level.

Even though only the 2X2 MMI case was presented in this section, one can design them to have an arbitrary number on inputs and outputs. The case of a 4X4 MMI designed for coherent receiver will be discussed later in section 2.9.

The advantages and drawbacks of a MMI as a power splitter are numerous. The MMI are more suitable for applications that require a very good balancing of power, such as Mach-Zender interferometers. Its robustness to fabrication makes it a really interesting component for integration. On the other hand, parasitic reflections can be problematic when combined to feedback-sensitive elements such as SOAs.

2.5.2 Directionnal couplers

Directional couplers (DC) are another category of power splitter. They use mode coupling to transfer light from one guide to the other [19]. When two guides are close enough, the unperturbed 'natural' modes intertwine and the actual mode basis of the coupled waveguides are "supermodes" with power in both guides, one symmetric and one anti-symmetric, with

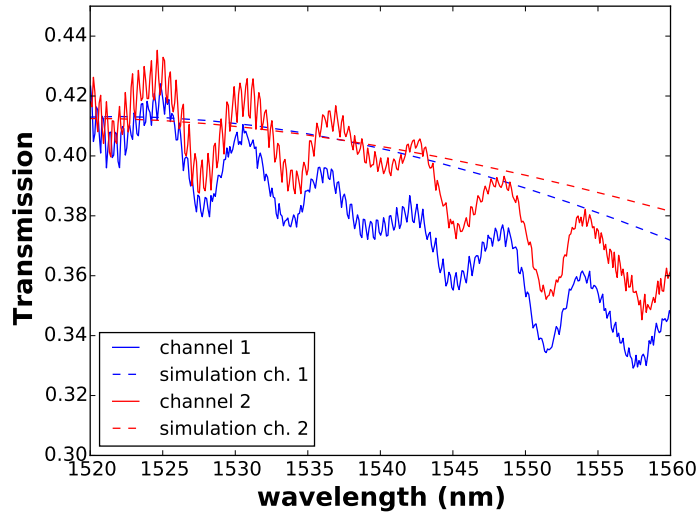


FIGURE 2.27: Transmission of a 2X2 MMI with $L = 61\mu m$, $W = 7\mu m$ on the 220-100nm platform

different effective index (see Fig. 2.28). Light coming from one waveguide will be expressed as a linear combination of the two fundamental modes. As they have different effective index, each mode will propagate at a different speed and the resulting interference will be light slowly beating between the two guides.

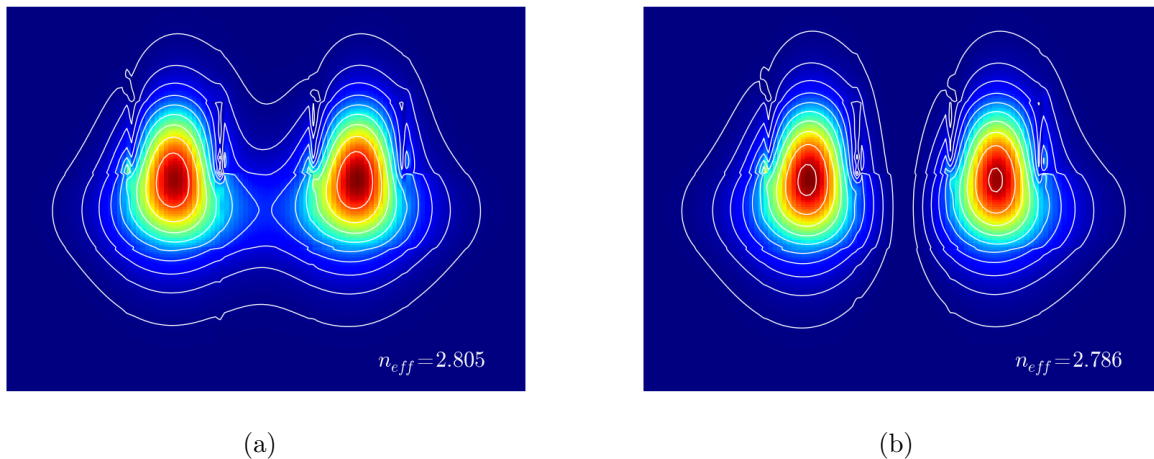


FIGURE 2.28: Power repartition in the (a) symmetric and (b) anti-symmetric supermodes of a directionnal coupler with rib 300-150 W0.45 @1.54 guides and a 400nm gap between

Coupled mode theory

The coupled mode theory gives a theoretical approach to the coupled waveguides problem. It makes the approximation of the perturbation theory : the field distributions in the coupling region are not very different from the ones with no interaction [19]. With this approximation, the optical field can be expressed as a linear combination of the two unperturbed modes :

$$E(x, y, z, t) = a(z).E_a(x, y).exp(i.(\omega.t - \beta_a.z) + b(z).E_b(x, y).exp(i.(\omega.t - \beta_b.z) \quad (2.28)$$

With β_l and E_l the propagation constant and electric field for guide $l \in [a, b]$. The $a(z)$ and $b(z)$ are linked through the differential equation, in the case of identical waveguides [20] :

$$\begin{cases} \frac{da(z)}{dz} = \kappa.b(z) \\ \frac{db(z)}{dz} = \kappa.a(z) \end{cases} \quad (2.29)$$

with κ the coupling coefficient. In our specific case, $\kappa = \frac{\Delta n.\pi}{\lambda}$ with Δn the index difference of the two supermodes. Equation 2.29 can be solved as :

$$\begin{cases} a(z) = a(0).cos(\kappa.z) - i.b(0).sin(\kappa.z) \\ b(z) = -i.a(0).sin(\kappa.z) + b(0).cos(\kappa.z) \end{cases} \quad (2.30)$$

Power is injected at one of the input ($a(0) = 1$ and $b(0) = 0$). The power coupled at two outputs of the directional coupler is then equal to :

$$\begin{cases} P_1 = |a(z_{max}).a^*(z_{max})| \\ P_2 = |b(z_{max}).b^*(z_{max})| \end{cases} \quad (2.31)$$

$$\Rightarrow \begin{cases} P_1 = a^2(0).(1 - \sin^2(\kappa.L)) \\ P_2 = a^2(0).sin^2(\kappa.L) \end{cases} \quad (2.32)$$

For more on coupled mode theory and calculation, please refer to [20, 21].

Simulation

Nowadays, calculations of coupled waveguides are much easier with the help of simulation tools. Instead of analytically calculate the mode profiles with all the necessary approximations, extracting the coupling coefficient and calculate the output power by hand, computers can give a rigorous mode profile and extract the effective index and make the whole propagation. The simulation can also help with the transition phase : as the two guides are approached before the straight part, light begins to couple from one guide to the other with a varying coupling strength. Simulation can take that effect into account as well. Figure 2.29 shows a schematic of the simulated structure with Width the guides widths, Length the length of the straight coupling region, Spacing the distance between the two waveguides and Curve Radius the radius of the approach bends.

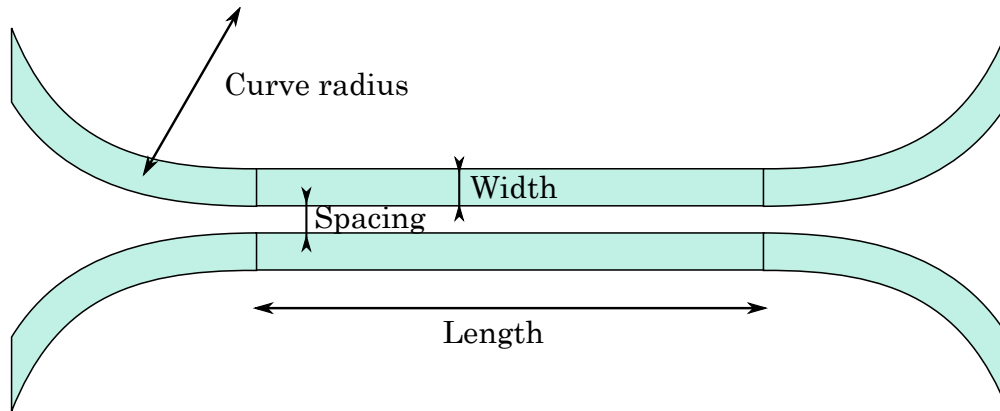


FIGURE 2.29: Schematic of a directional coupler

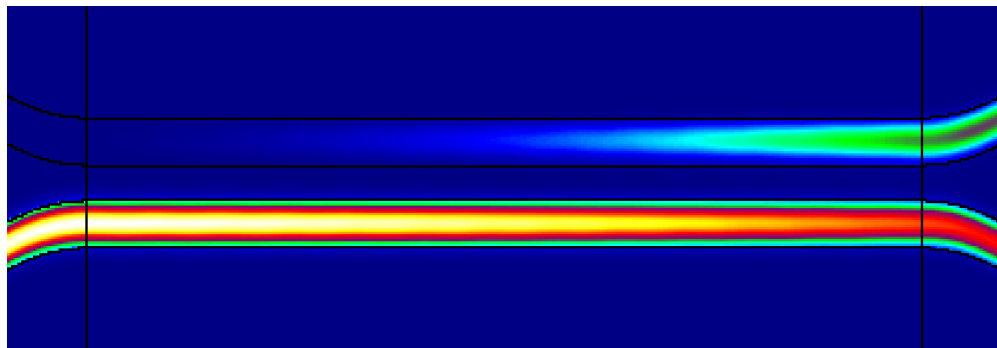


FIGURE 2.30: Propagation across a strip 300 W0.38 @1.54 directionnall coupler.

Figure 2.30 shows the intensity distribution across a strip DC. Due to the light beating with a sinusoidal variation as described in equation 2.32, the power repartition between the two guides can be arbitrary : one only need to tune the coupling length to get the desired ratio. This effect is clearly illustrated by figure 2.31a where the light is transferred from one output to the other as the coupling length is increased. On the other hand, this device comes with a large wavelength dependency as the coupling depends on field repartition of the unperturbed modes which is in turn dependant on wavelength. That effect is most important for a 50-50 coupler, as shown in figure 2.31b and can be very problematic in the case of devices that require to operate on a large bandwidth. In this simulation, the power at one output vary more than 50% on a 100nm wavelength window.

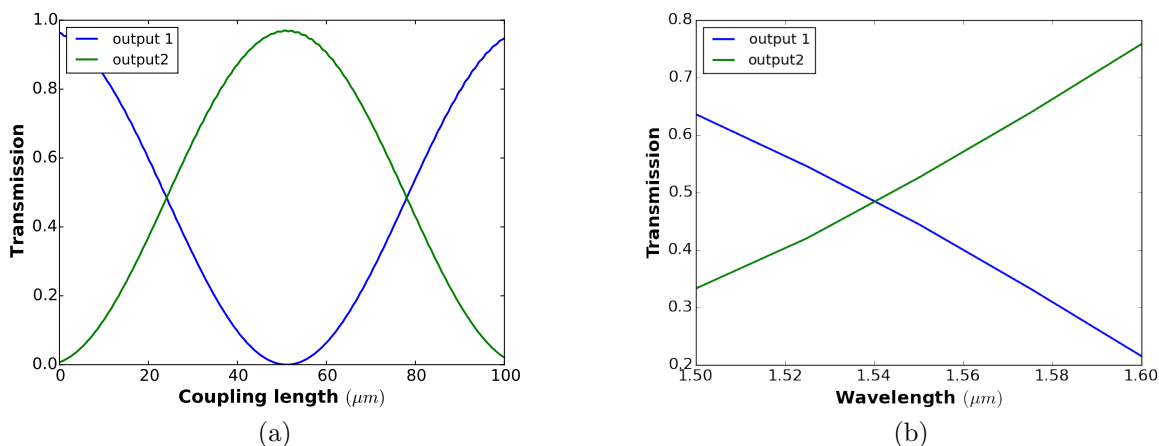


FIGURE 2.31: Transmission in both outputs with a scan on (a) length at $\lambda = 1.54\mu\text{m}$ (b) wavelength for a 50-50 distribution for a strip 300 W0.38 DC.

A 50-50 DC with a rib geometry was designed and measured during this thesis. The design flow was identical to what was presented for the strip DC above, only with a rib waveguide instead. The simulation performances were very similar to what was presented in figure 2.31. The Measurement results are plotted in figure 2.32. A simulation was also performed with small variations on the slab's height in order to understand the difference between the measured results and the simulation of the same device. The most notable difference is the crossing point : the 50-50 behaviour is obtained at 1510nm instead of the designed 1540nm. The new simulation fits the measure very well. It was made with a rib 220-105 instead of a rib 220-100. The device is thus very sensitive to fabrication variations as a difference of 5nm in slab's height can shift the optimal working point of the device by 30nm. On the other hand, the new simulation shows a very good fit with the experiment, which shows the validity of the simulation. That tool can now be used to optimise the robustness of the device to wavelength and fabrication variations.

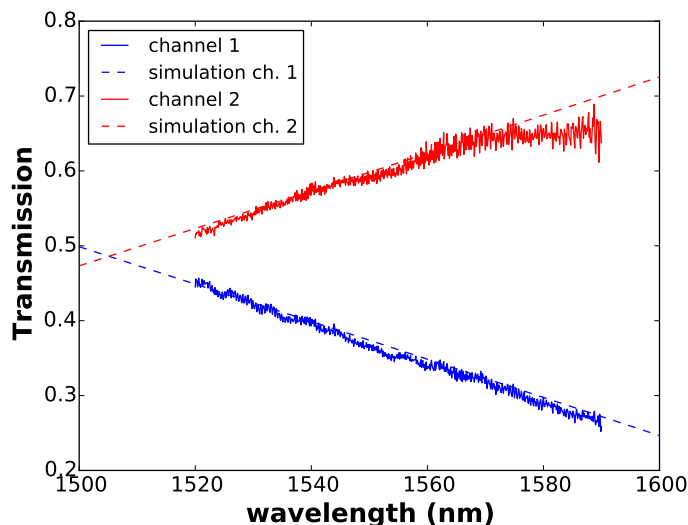


FIGURE 2.32: Measured and simulated response of a 50-50 Rib 220-100 W0.4 spacing 0.4 directional coupler after normalisation by grating couplers. Simulation parameters were tweaked to fit the measures. Simulated slab's height is 105nm instead of 100nm.

Overview of power splitters

MMI and DC are the two types power splitter and their properties makes them suitable to be integrated in more complex components. Each situation has its specific requirements, and those two designs can cover most of them.

Table 2.1 gives an overview MMI and directional coupler as power splitters. Their advantages and drawbacks are discussed, along with applications they are mostly used for.

	Advantages	Drawbacks	Used in
MMI	<ul style="list-style-type: none"> - Very good power balancing - Robust to fabrication - good wavelength insensitivity. - any number of input/output 	<ul style="list-style-type: none"> - Extra insertion losses - Parasitic reflections 	<ul style="list-style-type: none"> - Mach-Zender interferometers - Hybrid 90°
DC	<ul style="list-style-type: none"> - No losses - Can make any arbitrary power repartition 	<ul style="list-style-type: none"> - Wavelength sensitive - Fabrication sensitive 	<ul style="list-style-type: none"> - Ring resonators - Power splitter close to lasers an SOA

TABLE 2.1: Comparaison of MMI and Directionnal couplers as power splitters

2.6 Ring resonators

Ring resonators are devices where light enters a circular resonator. In that resonator, interferences will occur with equally-spaced constructive interferences. The resulting transfer function can be used for many applications like filtering [22], wavelength multiplexing (see section 3.1), laser cavity filtering (see section 4.3), modulators [23–25] and routing [26, 27].

The silicon photonic platform is well adapted to all applications requiring ring resonators because of the very high index contrast that enables very small curvatures with low losses (see section 2.2.2), and thus rings with perimeters in the range of $20\mu m$, which are not available on many other platforms [22].

Theory

In a ring resonator, the phase difference after one turn in the ring can be expressed as :

$$\theta = \frac{2 \cdot \pi \cdot n_{eff} \cdot L}{\lambda} \quad (2.33)$$

with λ the wavelength, n_{eff} the effective index of the guided mode and L the ring perimeter. The condition of constructive interference is then :

$$\theta = 2 \cdot \pi \cdot m \quad (2.34)$$

with m an integer.

The light is coupled to the ring through power splitters, mostly made by directional couplers and eventually multimode interferometers [22]. The relation between the incident electric field and the one at the other ends of the power splitter can be expressed, with the notations from 2.33 :

$$\begin{pmatrix} E_{i1,r} \\ E_{t1,r} \end{pmatrix} = \begin{pmatrix} t & \kappa \\ -\kappa^* & t^* \end{pmatrix} \cdot \begin{pmatrix} E_{i1} \\ E_{t2} \end{pmatrix} \quad (2.35)$$

With t and κ the the through and cross coefficient respectively. A similar equation can be deduced for the second coupler.

In the case of a lossless DC :

$$|\kappa^2| + |t^2| = 1 \quad (2.36)$$

In the case of a symmetric ring with a round trip loss of α , the relation between the different fields inside the ring is :

$$\begin{cases} E_{i2,r} = \alpha_{1/2} \cdot e^{i \cdot \theta_{1/2}} \cdot E_{t1,r} \\ E_{i1,r} = \alpha_{1/2} \cdot e^{i \cdot \theta_{1/2}} \cdot E_{t2,r} \\ \alpha_{1/2} = \sqrt{\alpha} \\ \theta_{1/2} = \theta/2 \end{cases} \quad (2.37)$$

From equations 2.35 and 2.37, one can express the electric field at through and drop ports :

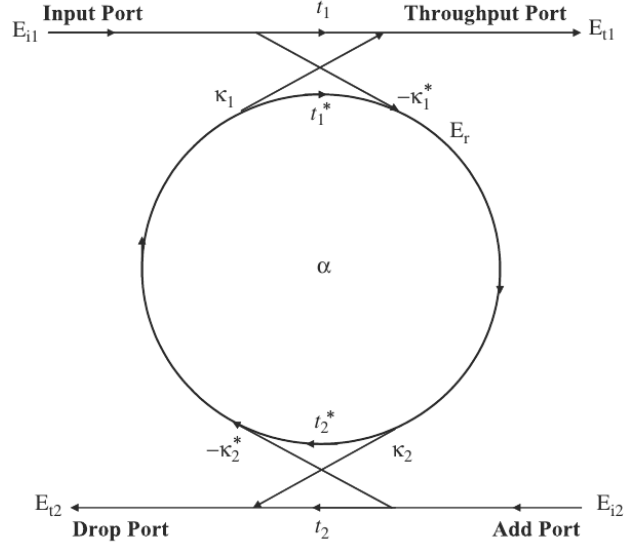


FIGURE 2.33: Schematic of a Ring Resonator with notations used in this section. Reproduced from [28]

$$\begin{cases} E_{t1} = \frac{t_1 - t_2^* \cdot \alpha \cdot e^{i \cdot \theta}}{1 - t_1^* \cdot t_2^* \cdot \alpha \cdot e^{i \cdot \theta}} \\ E_{t2} = \frac{-\kappa_1^* \cdot \kappa_2 \cdot \alpha^{1/2} \cdot e^{i \cdot \theta_{1/2}}}{1 - t_1^* \cdot t_2^* \cdot \alpha \cdot e^{i \cdot \theta}} \end{cases} \quad (2.38)$$

The corresponding spectra for through and drop ports are presented in figure 2.34. The spectrum is periodic with very sharp peaks (on drop port) or very sharp dips (on throughput port) at the position of constructive interferences. From this kind of spectrum, one can define the free spectral range (FSR) and finesse which characterise the spectrum of a ring resonator.

The FSR is defined as the wavelength separation between two adjacent peaks. It can be expressed by the following formula :

$$FSR(\lambda) = \frac{\lambda^2}{n_g \cdot L} \quad (2.39)$$

with n_g the group index of the mode propagating inside the ring. The full width at half maximum (FWHM) can be also be defined, considering a symmetrical ring ($t_1 = t_2$) :

$$FWHM(\lambda) = \frac{\lambda^2}{\pi \cdot L \cdot n_{eff}} \cdot \sqrt{\frac{(1 - t^2 \cdot \alpha)^2}{t^2 \cdot \alpha}} \quad (2.40)$$

With α the round trip losses (a lossless ring will have $\alpha = 1$). From these two equations, one can define the finesse of the ring resonator, defined as the ratio between the FSR and the

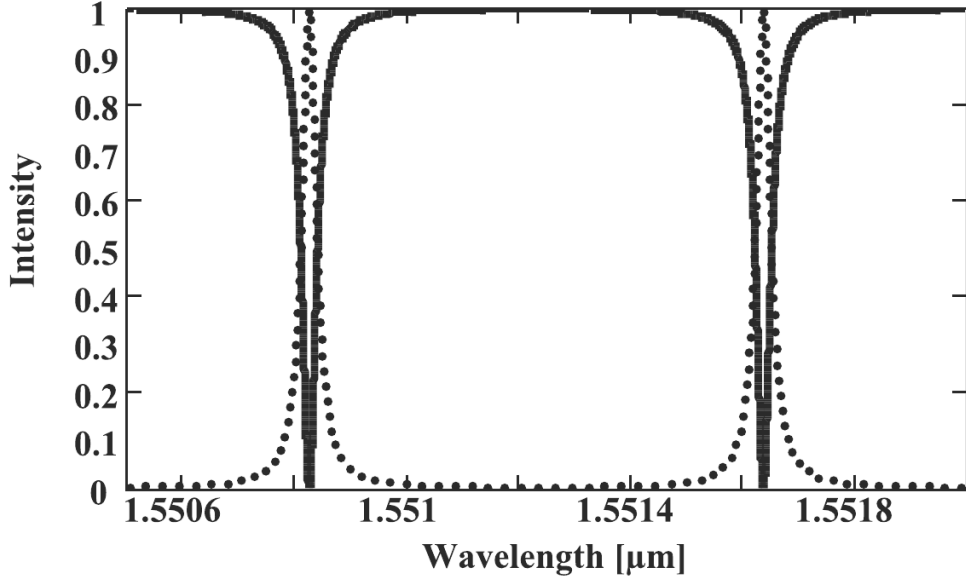


FIGURE 2.34: Spectra of intensity at through port (full) and drop port (dashed). Reproduced from [28]

FWHM, the higher the finesse, the sharper the peaks :

$$\mathfrak{F} = \frac{FSR}{FWHM} = \frac{n_{eff}}{n_g} \cdot \pi \cdot \sqrt{\frac{t^2 \cdot \alpha}{(1 - t^2 \cdot \alpha)^2}} \quad (2.41)$$

From equations 2.38 and 2.41, it can be deduced that the maximum power at the through/drop port as well as the finesse are dependant on two main factors, the transmission coefficient in intensity $T = |t|^2$ and the round trip losses α . The maximum transmission at the drop port for a ring with symmetric couplers with transmission $T = |t_1|^2 = |t_2|^2$ is [28] :

$$P_{max} = |E_{t,max}|^2 = \frac{\alpha \cdot (1 - T)^2}{(1 - \alpha \cdot T)^2} \quad (2.42)$$

A ring with more finesse will have lower maximum power, as well as a ring with higher losses. Figure 2.35 gives a visual representation of these effects. A maximum power of 1 is obtained only for a lossless ring ($\alpha = 1$). For other cases, the maximum power decreases as the finesse increases. That effect is more important for rings with high losses (or equally a low α value).

Measurement

Ring resonators were fabricated and measured. The ring, whose results are presented in figure 2.36 were designed with a rib 300-150 and a FSR of 100 GHz, or 0.563 nm. The transmission coefficient was simulated to be $T = 0.9$. The measured spectrum shows a good

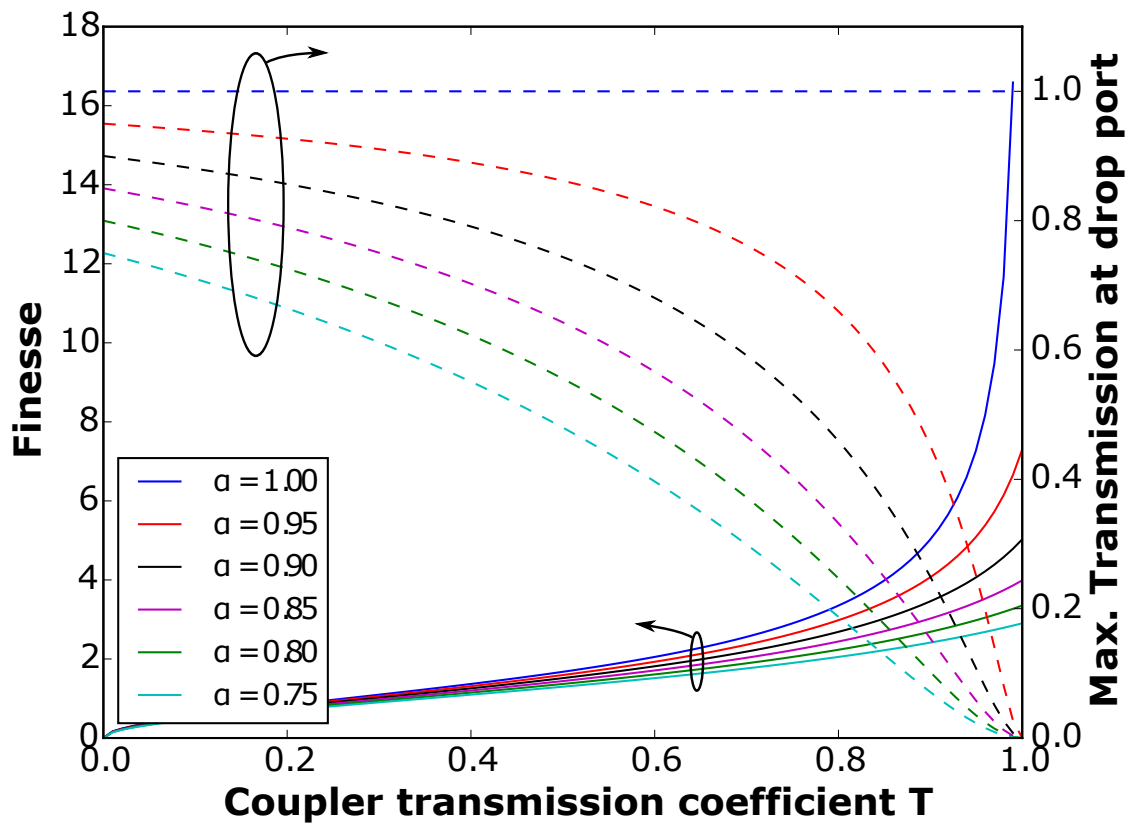


FIGURE 2.35: Finesse and maximum transmission at drop port for various transmission coefficient and round trip losses

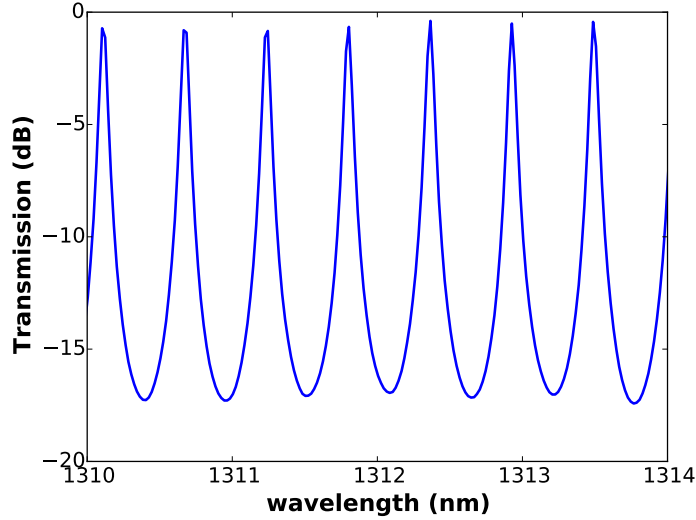


FIGURE 2.36: Measured ring resonator with normalisation by FGC. Guide geometry is rib 300-150 W0.45 with a simulated transmission coefficient $T=0.9$

correspondance with the simulation, with a mean FSR of $FSR = 0.56nm$ and a FWHM of $FWHM = 0.075nm$, giving a final finesse of $\mathfrak{F} \simeq 7.5$. The large value of the measured finesse suggests that the directional coupler has a transmission larger than the designed 0.9, likely around 0.95.

2.7 The Mach-Zehnder interferometer

Mach-Zehnder interferometers (MZI) are another important building block for integrated photonic circuits. They are used both on silicon and other platforms for various applications. A non exhaustive list includes modulators (see section 4.5.3) and isolators (see section 2.8).

The principle of operation relies on interferences : a light beam is split into two different paths, and then recombined. The path difference between the two paths creates interferences that are dependant on the wavelength. A simplified schematic is presented in figure 2.37

Let us consider the case of a perfect 50-50 power splitter. In that case, the electric field amplitude just after the splitter is :

$$E_1 = E_2 = \frac{E_{in}}{\sqrt{2}} \quad (2.43)$$

Just before the recombination of the two beams, in the case where waveguides are of constant shape, the electric field amplitude can be expressed as :

$$E_k = \frac{E_{in}}{\sqrt{2}} \cdot e^{(i \cdot \frac{2 \cdot \pi \cdot n_{eff}}{\lambda} \cdot L_k)} , \quad k = 1, 2 \quad (2.44)$$

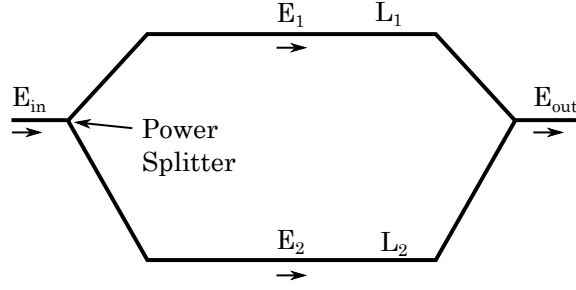


FIGURE 2.37: Schematic of a Mach-Zehnder interferometer

with L_k the length of the selected path. The recombination is made, again with the supposition of the perfect combiner :

$$E_{out} = \frac{E_1}{\sqrt{2}} + \frac{E_2}{\sqrt{2}} = \frac{E_{in}}{2} \cdot (e^{i \cdot \frac{2 \cdot \pi \cdot n_{eff}}{\lambda} \cdot L_1} + e^{i \cdot \frac{2 \cdot \pi \cdot n_{eff}}{\lambda} \cdot L_2}) \quad (2.45)$$

$$\Rightarrow E_{out} = \frac{E_{in}}{2} \cdot e^{-i \cdot \frac{2 \cdot \pi \cdot n_{eff}}{\lambda} \cdot L_1} \cdot (e^{i \cdot \frac{2 \cdot \pi \cdot n_{eff}}{\lambda} \cdot (L_2 - L_1)} + 1) \quad (2.46)$$

The intensity at the output is then :

$$I_{out} = E_{out} \cdot E_{out}^* = \frac{E_{in}^2}{2} \cdot (1 + \cos(\frac{2 \cdot \pi \cdot n_{eff}}{\lambda} (L_1 - L_2))) \quad (2.47)$$

The intensity varies as a cosinus with a dependence in wavelength and effective index. The condition for constructive interference can be easily deduced :

$$n_{eff}(L_1 - L_2) = l \cdot \lambda, \quad l \in \mathbb{Z}^* \quad (2.48)$$

In the case of a low dispersion guide, the effective index has no variation and the intensity depends only on the wavelength. In the case of silicon waveguides, the group index is very different from the effective index. The Free Spectral Range (FSR) is therefore expressed in function of the group index as :

$$FSR = \frac{\lambda^2}{n_g \cdot \Delta L} \quad (2.49)$$

with n_g the group index in the guide and $\Delta L = |L_1 - L_2|$.

Figure 2.38 shows the simulated spectrum of a MZI with a 2X2 power splitter. The intensity of each channel is a square cosinus, but the two output channels have opposed intensities.

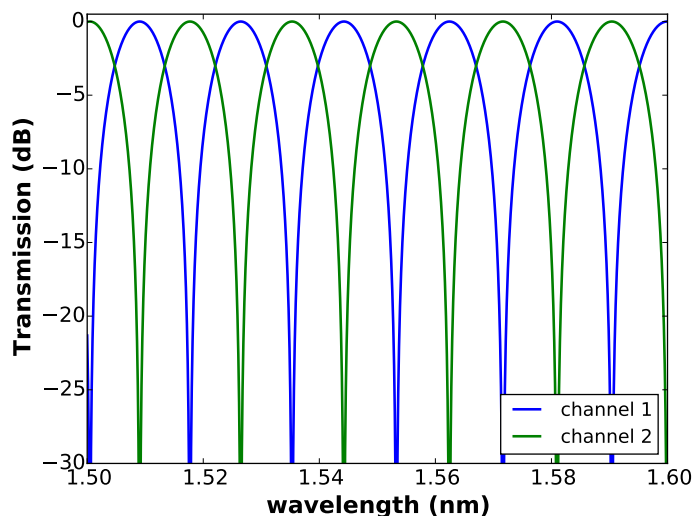


FIGURE 2.38: Simulated spectrum of a MZI for a strip 300-0 W0.4 with $\Delta L = 30\mu m$

2.8 Optical Isolators

2.8.1 Present day commercial optical isolators

The quest for a low-cost integrated version of an optical isolator that is compatible with industrial manufacturing technique is one of the remaining largest challenges in photonics research. Bulk free-space isolators have been commercially available long before the advent and the rise of optical fiber communications and PICs. They are constituted of Faraday rotators that combine a non-reciprocal rotation of the linear light polarization with appropriately placed polarisers at the input and output, as shown in figure 2.39. Bulk isolators are all made of iron garnet materials (mostly doped with elements such as Ce, Bi, La, Pr,... depending on operation requirements). These materials are deposited via Liquid Phase epitaxy on lattice matched transparent garnet substrates (mostly Gadolinium Gallium Garnet). The attractiveness of this material comes from the fact that it combines low optical absorption at telecom wavelengths with a strong magneto-optic (MO) effect. They are still nowadays the only type of optical isolator used in any packaged commercial photonic component. Bulk isolators are very common and mature components that are available in many sizes and with a whole range of performances depending on applications.

The currently available optical isolators that are commonly used in laser and transceiver modules are expected to achieve an isolation ratio in excess of 25dB and insertion losses lesser than 0.3dB. In addition the isolator must not introduce any significant distortion of the output wavefront. Their cost is highly dependent upon volumes purchased but 20-30\$ is not untypical, and this constitutes a significant fraction of the overall material costs in a packaged module. Their impact on the total cost of the photonic component in which they are used is also related to the associated packaging costs which may be as much as

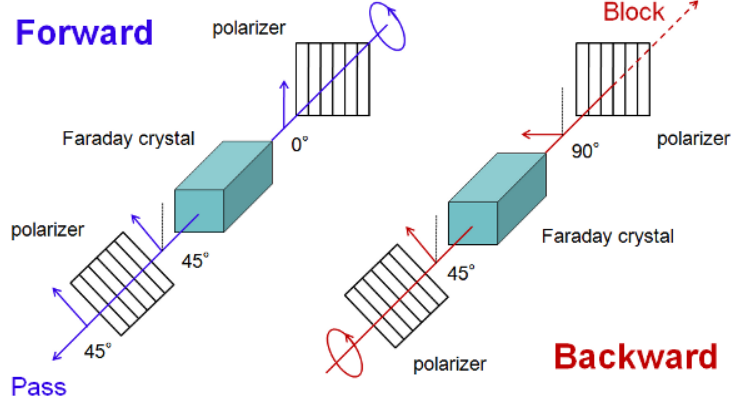


FIGURE 2.39: Schematic of a commercial rotator based on Faraday rotation

20% of the total. Moreover the current lack of a commercially viable integrated isolator has an indirect impact on device performance and cost because cheaper, more flexible and higher performance devices designs would become possible if isolation could be integrated into higher functionality PIC's.

2.8.2 Non Reciprocal Phaseshift

In this thesis, a different aspect of the magneto-optic effect will be studied. The rotation coefficient will be used to create a non-reciprocal phase shift (NRPS). It means that a signal going in the forward direction will not experience the same refractive index in the garnet as the one going in the backward direction. The result over the propagation distance is a phase difference between the forward and backward signals. An interferometric device can then use that phase shift to create constructive interferences in the forward direction and destructive in the backward direction. The devices most commonly used are ring resonators [29] and Mach-Zehnder interferometers [30–32].

The NRPS is caused by a material with non symmetrical dielectric permittivity tensor [30]. In most cases, Cerium doped garnet (Ce :YIG) is used. For a Ce :YIG with a saturation magnetic field applied in the x-direction, the dielectric permittivity tensor takes the following form :

$$\epsilon = \begin{pmatrix} n_{YIG}^2 & 0 & i.\epsilon_{xz} \\ 0 & n_{YIG}^2 & 0 \\ -i.\epsilon_{xz} & 0 & n_{YIG}^2 \end{pmatrix} \quad (2.50)$$

and

$$\epsilon_{xz} = n_{YIG} \cdot \lambda \cdot \theta_F / \pi \quad (2.51)$$

with n_{YIG} the refractive index of Ce :YIG and θ_F the associated Faraday rotation coefficient. in the C-band, $\theta_F \simeq -4500^\circ/cm$.

As shown above, CE :YIG is a good material to create a non-reciprocal phase shift. On the other hand, garnet is not a material of choice for guided optics as structuring it into a waveguide is very challenging. The proposed solution is therefore to use another platform to create optical waveguides and then bond the garnet on top of that structure. The optical mode will experience the non reciprocal effect through the evanescent field leaking from the guiding structure into the garnet. Our structure differs from the other publications as we plan on using direct bonding [33] instead of molecular bonding, with no bonding layer between the silicon and the garnet. The proposed structure is presented in figure 2.40. The non reciprocal phase shift (NRPS) can then be calculated with this formula for a TM mode propagating along the Z-axis with magnetic field along x-axis [30] :

$$NRPS = \beta_{fwd} - \beta_{bwd} = -j \cdot \omega \cdot \frac{\iint g(x, y) \cdot \epsilon_{xz} \cdot E_y^0 \cdot E_z^0 \cdot dx \cdot dy}{\iint E_y^0 \cdot H_x^0 - E_x^0 \cdot H_y^0 \cdot dx \cdot dy} \quad (2.52)$$

with $g(x, y) = 1$ in the doped garnet region and $g(x, y) = 0$ elsewhere.

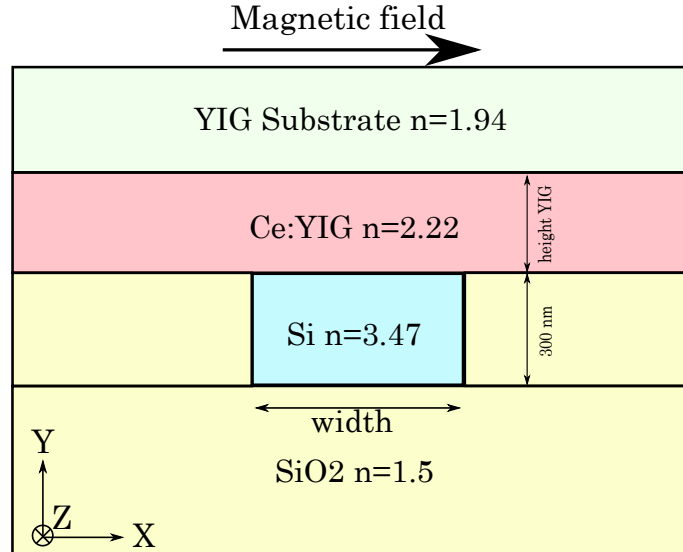


FIGURE 2.40: Schematic of waveguide in an integrated isolator

Due to the preferred direction of the magnetic field in the x-direction, the mode inside the guide must be transverse magnetic in order to be affected by the NRPS. The TM^0 mode will be chosen for all the works presented in this thesis. Figure 2.41a shows the effective index of the main modes with this geometry. The chosen width must be lower than $0.5\mu m$ in order to avoid multimode behaviour.

Figure 2.41b shows the simulated NRPS for the TM^0 mode. The NRPS variation depends on one main effect. The field in a smaller waveguide will be less confined and will have a larger part of its field in the doped garnet region. But a guide even smaller will have part of its field leaking even further, in the YIG substrate region, which lowers the NRPS. The

optimum point for this geometry is around $0.4\mu m$. The final geometry was chosen with a width of $0.5\mu m$ to get a good compromise between propagation losses, NRPS and single mode behaviour.

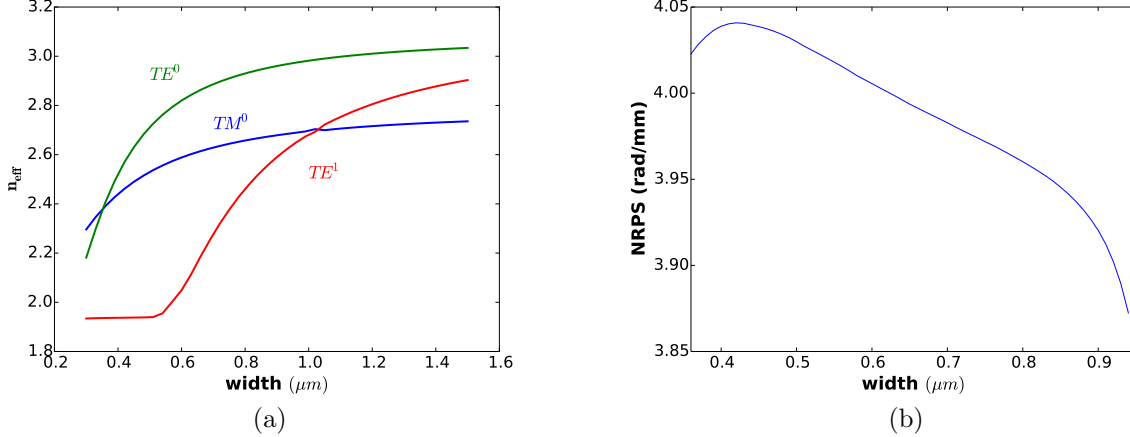


FIGURE 2.41: (a) Effective index of the modes in the guides with garnet on top (b) corresponding NRPS for the TM^0 mode

2.8.3 Mach-Zehnder interferometers as isolators

A Mach-Zehnder interferometer combined with a NRPS can make an isolator : if the phase difference between the forward and backward direction is equal to π , then one can be in constructive interference while the other is in destructive interference. The chosen geometry for the MZ is the same as in [30]. The garnet is bonded only on half of the MZ. A schematic of the configuration presented in figure 2.42. The forward and backwards phase difference at the end of the Mach-Zehnder interferometer can be expressed as :

$$\Delta\phi_{fwd} = \frac{2 \cdot \pi \cdot n_{eff}}{\lambda} \cdot (L_2 - L_1) + (L_1 + L_2) \cdot \frac{NRPS}{2} \quad (2.53)$$

$$\Delta\phi_{bwd} = \frac{2 \cdot \pi \cdot n_{eff}}{\lambda} \cdot (L_2 - L_1) - (L_1 + L_2) \cdot \frac{NRPS}{2} \quad (2.54)$$

The condition for constructive interference in the forward direction and destructive interference in the backward direction is :

$$\Delta\phi_{fwd} - \Delta\phi_{bwd} = \pi \quad (2.55)$$

The length that must be covered by garnet with the right magnetic field must then be equal to :

$$L = L_1 + L_2 = \frac{\pi}{NRPS} \simeq 780\mu m \quad (2.56)$$

In order to simplify the experimentation phase and extraction of the measured NRPS, the MZ was designed with a FSR of 10nm. We therefore have :

$$\Delta L \simeq \frac{\lambda^2}{FSR \cdot \frac{n_{g,c} + n_{g,u}}{2}} = 55\mu m \quad (2.57)$$

with $n_{g,c}$ and $n_{g,u}$ the group index of the covered and uncovered guides respectively

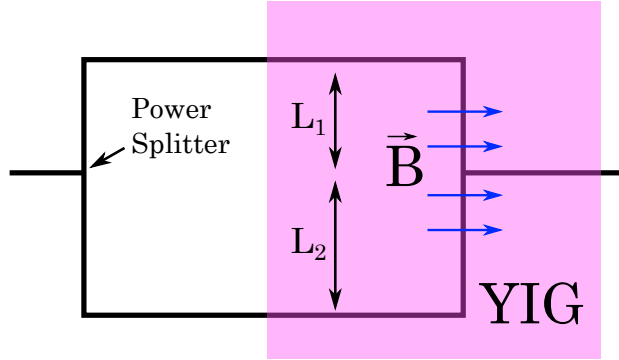


FIGURE 2.42: Schematic of waveguide in an integrated isolator

Because of the presence of garnet, one of the power splitters must be designed separately with the new layers. Several designs were made, using either DC or MMI as power splitter. The transition between the uncovered and the covered guide was also studied. Designs were made with straight transitions and others with transitions tilted at 30° .

Unfortunately, no component with garnet bonded on top were fabricated up to now.

2.9 Multimode Interferometers as Hybrid 90

2.9.1 Use and operation of an hybrid 90

Hybrid 90° are components whose function is to mix a signal with another with appropriate phase difference. The two inputs are commonly referred as the local oscillator (LO) and the signal on which an information is to be decoded. The hybrid 90° introduces an additional phaseshift between the signal and LO that can be used to extract the information encoded in the signal. Hybrid 90° have 4 outputs with dephasing between signal and local oscillator a multiple of $\pi/2$, as described in the schematic figure 2.43.

Hybrid 90 are mostly used in coherent receiver. Each output is linked to a photodiode. The received signal E_l , $l \in [A, B, C, D]$ for each photodiode is :

$$\begin{cases} E_A = E_S \cdot e^{(i \cdot \omega_S \cdot t + \phi)} + E_{LO} \cdot e^{(i \cdot \omega_{LO} \cdot t)} \\ E_B = E_S \cdot e^{(i \cdot \omega_S \cdot t + \phi)} - E_{LO} \cdot e^{(i \cdot \omega_{LO} \cdot t)} \\ E_C = E_S \cdot e^{(i \cdot \omega_S \cdot t + \phi)} + i \cdot E_{LO} \cdot e^{(i \cdot \omega_{LO} \cdot t)} \\ E_D = E_S \cdot e^{(i \cdot \omega_S \cdot t + \phi)} - i \cdot E_{LO} \cdot e^{(i \cdot \omega_{LO} \cdot t)} \end{cases} \quad (2.58)$$

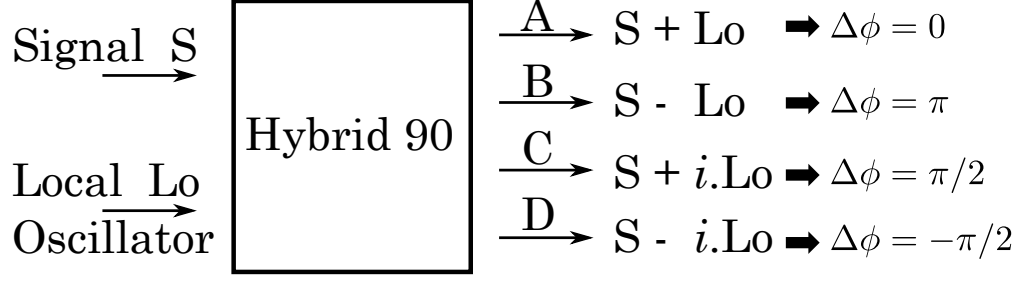


FIGURE 2.43: Schematic of a hybrid 90

With E_k , $k \in [S, LO]$ the optical amplitude of signal, local oscillator and ω_k their associated angular frequency.

The intensity measured for photodiode A is

$$I_A = E_A \cdot E_A^* = (E_S \cdot e^{i(\omega_S t + \phi)} + E_{LO} \cdot e^{i(\omega_{LO} t)}) \cdot (E_S \cdot e^{-i(\omega_S t + \phi)} + E_{LO} \cdot e^{-i(\omega_{LO} t)}) \quad (2.59)$$

$$\Rightarrow I_A = E_S^2 + E_{LO}^2 + 2 \cdot E_S \cdot E_{LO} \cdot \cos((\omega_S - \omega_{LO}) \cdot t + \phi) \quad (2.60)$$

A similar expression can be obtained for the other photodiodes :

$$\begin{cases} I_A = E_S^2 + E_{LO}^2 + 2 \cdot E_S \cdot E_{LO} \cdot \cos((\omega_S - \omega_{LO}) \cdot t + \phi) \\ I_B = E_S^2 + E_{LO}^2 - 2 \cdot E_S \cdot E_{LO} \cdot \cos((\omega_S - \omega_{LO}) \cdot t + \phi) \\ I_C = E_S^2 + E_{LO}^2 + 2 \cdot E_S \cdot E_{LO} \cdot \sin((\omega_S - \omega_{LO}) \cdot t + \phi) \\ I_D = E_S^2 + E_{LO}^2 - 2 \cdot E_S \cdot E_{LO} \cdot \sin((\omega_S - \omega_{LO}) \cdot t + \phi) \end{cases} \quad (2.61)$$

A difference of measured intensity is used to extract the sinusoidal part :

$$\begin{cases} I_{Re} = I_A - I_B = 4 \cdot E_S \cdot E_{LO} \cdot \cos((\omega_S - \omega_{LO}) \cdot t + \phi) \\ I_{Im} = I_C - I_D = 4 \cdot E_S \cdot E_{LO} \cdot \sin((\omega_S - \omega_{LO}) \cdot t + \phi) \end{cases} \quad (2.62)$$

Digital signal processing (DSP) is then used to filter the $(\omega_S - \omega_{LO}) \cdot t$ and extract the in phase and quadrature parts of the the phase.

The key characteristics are the accuracy of the phase shift for each output and the good power balance between two associated outputs. The latter is usually named the Common Mode Rejection Ratio (CMRR). For the in phase part, it can be expressed as :

$$CMRR(k, AB)[dB_e] = 20 \cdot \log_{10} \left(\frac{P_{A,k} - P_{B,k}}{P_{A,k} + P_{B,k}} \right) \quad (2.63)$$

with $P_{j,k}$ the received power at output j with signal injected at input k . The quadrature part has a similar expression, replacing A and B by C and D . The CMRR is expressed in electrical decibel, hence the factor 20 [34].

There are two common designs for the hybrid 90. The first uses a set of four 2×2 combiners such as directionnal couplers or multimode interferometers (MMI) with tailored input/output combinations and phase delays [35]. The other one uses MMI with four output channels [34, 36–38]. In this thesis, only the 4×4 MMI is thoroughly studied.

2.9.2 4×4 Multimode Interferometer

The 4×4 MMI is an excellent candidate for a hybrid 90. Signal and LO are injected at inputs 1 and 3 and get the right phase difference on the outputs as shown in figure 2.44. The two outer channels for the in-phase part and the two inner outputs for the quadrature part.

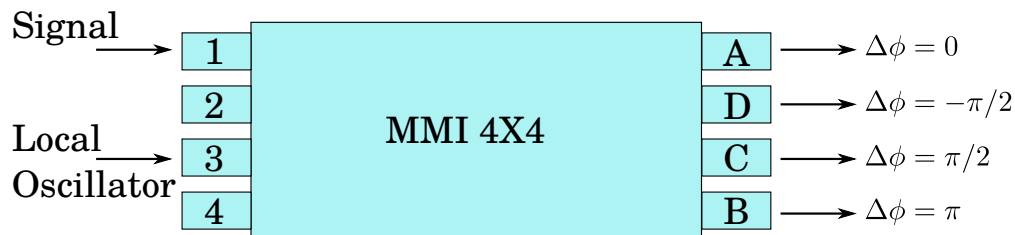


FIGURE 2.44: Schematic of a 4×4 MMI used as hybrid 90

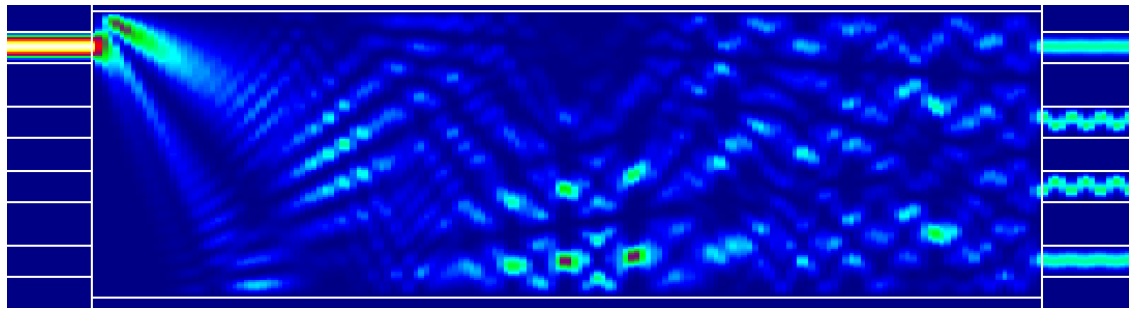
Simulation

Simulations were made on the 4×4 MMI. The main difficulty was to tune all variables so that all channels are getting the same power amount from input 1 and 3. The phase differences were set automatically by the physics of such a device. Figure 2.45 shows the intensity across the device with light injected from input 1 and 3. The MMI is designed with a rib 300-150 geometry.

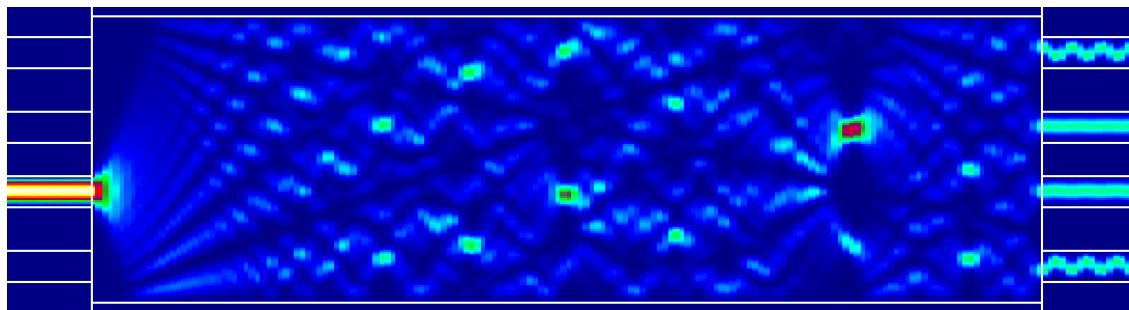
Two different configurations were tested. One is a short MMI with a width $W = 7\mu m$ and a length of $L = 99\mu m$. The second at the other extreme with $W = 23\mu m$ and $L = 1055\mu m$, both in a wavelength window centered at $1.54\mu m$. Both devices were simulated and measured. The goal is to compare their characteristics and decide which shows the best performances for an implementation in coherent receivers. From [34] and [39], we know that a very large MMI will most probably have higher phase error and reduced CMRR. On the other hand, a large device should be less sensitive to fabrication variations.

Figure 2.46 shows the CMRR (with the definition of CMRR from equation 2.63) of both devices as a function of wavelength. The CMRR is better than 30dB on almost the whole bandwidth for the short version and a bit worse, at 25dB, for the long version. Both have a good enough CMRR to be used in coherent receivers.

The phase error is a critical element of any hybrid 90. It is usually admitted that the phase error should be lower than 5° . Figure 2.47 shows the phase error of the two simulated devices. The phase error is defined as the phase difference between the signals coming from input 1 and input 3 compared to the optimal phase difference as defined in figure 2.44. The phase error should be restricted between -5° and $+5^\circ$. Once more, the short MMI is slightly better than the long one, with a phase error always in the acceptable windows, where the long one satisfies the condition on all channels only on a limited bandwidth.

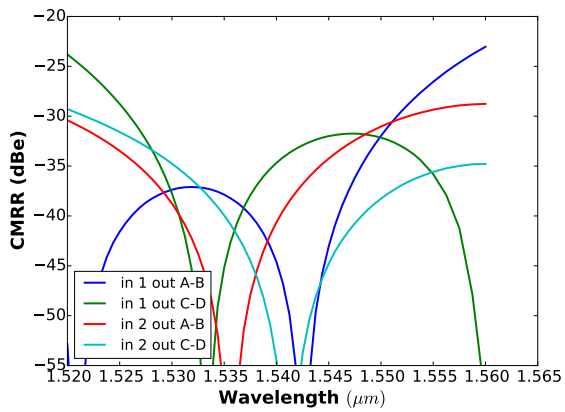


(a)

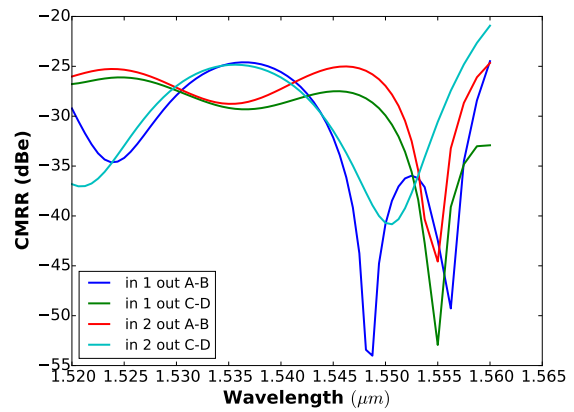


(b)

FIGURE 2.45: Intensity profile across a 4X4 MMI with a length of $1055 \mu m$. Light is injected on (a) input 1 (b) input 3



(a)



(b)

FIGURE 2.46: Simulated CMRR for (a) the MMI with $L = 99 \mu m$ (b) the MMI with $L = 1055 \mu m$

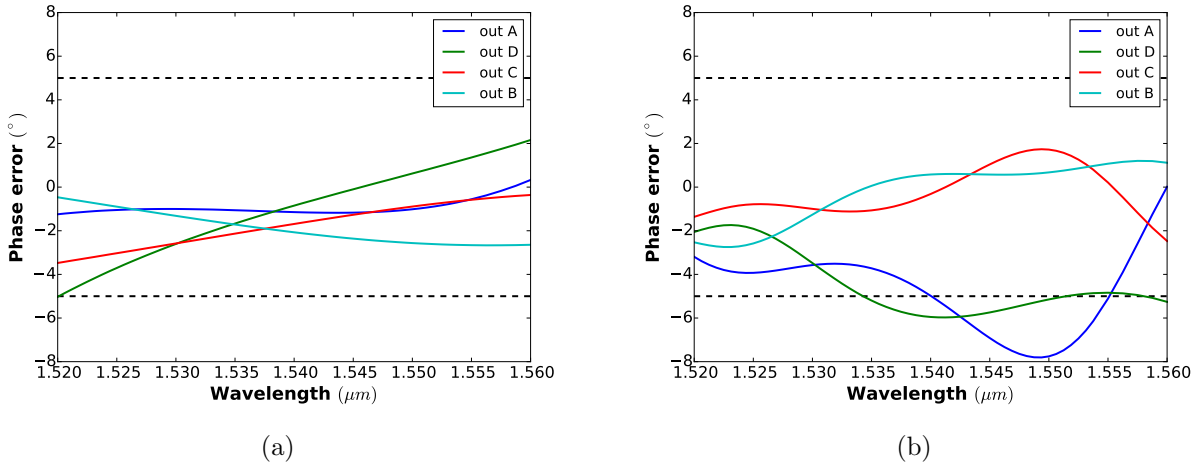


FIGURE 2.47: Simulated phase error for (a) the MMI with $L = 99\mu m$ (b) the MMI with $L = 1055\mu m$

Measure

The simulated devices have been fabricated by Leti. Measures were made with an automated prober on 5 different dies, all coming from the same wafer. The input 1 and 3 were injected with the two paths out of a Mach-Zehnder interferometer with a free spectral range (FSR) around 1 nm, as presented on the schematic figure 2.48a

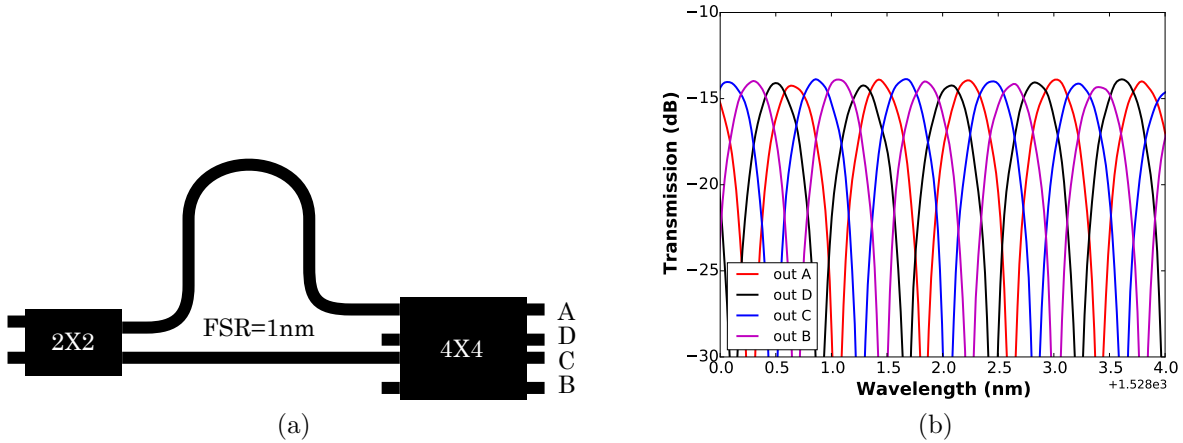


FIGURE 2.48: (a) Setup for measured hybrid 90° device (b) Zoomed spectrum of the "long" device

The phase difference at the end of the Mach-Zehnder interferometer depends on the wavelength. This phase difference is transmitted to the hybrid 90 on input 1 and 3. To that is added the phase shift caused by the MMI itself. As a result, the condition of constructive

interference will be different for each output : the spectra for one output will be shifted a quarter or half FSR from the others. In the ideal case, all maxima have the same intensity and are spaced by exactly a quarter of FSR. Any deviation from that can be tracked to a power imbalance or a phase error in the MMI. Figure 2.48b shows a measured zoomed spectrum of the device.

The procedure used to extract the phase error is the following :

- Detect the maximum of each peak. To increase precision, a fit is made for each peak with a cosine function. The fit is made over many periods to further increase position precision.
- The n^{th} peak of channel A is taken as the reference for calculating the phase differences of all other channels. Peak number $n+1$ is used to get the FSR as $FSR = \lambda_{A,n+1} - \lambda_{A,n}$, with $\lambda_{j,n}$ the wavelength of the n^{th} peak taken from output j
- The relative position of n^{th} peak for the other channels are expressed as a fraction of the FSR : $F_{j,n} = \frac{\lambda_{j,n} - \lambda_{A,n}}{FSR}$
- One full FSR makes a phase difference of 360° . The phase difference is then $\Delta\phi_{j,n} = 360 \cdot F_{j,n}$. The phase error is the difference between the theoretical difference and the measured one

Figure 2.49 shows the phase error for the short and long MMI measured on die #2 in function of wavelength. The phase error mostly remain in the acceptable limits, with the long MMI a bit less stable in wavelength than the short one, with large phase errors at the extremity of the wavelength window.

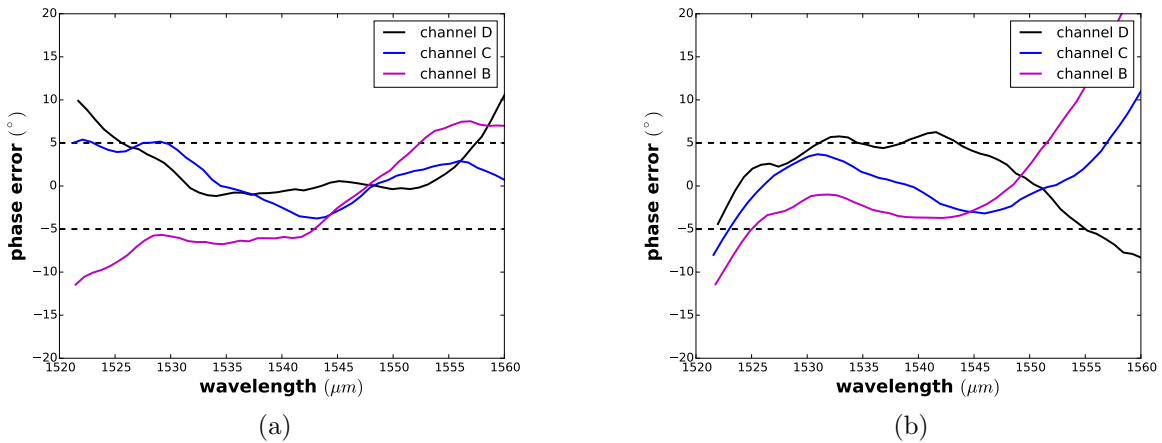


FIGURE 2.49: Measured phase error on die #2 for (a) the MMI with $L = 99\mu m$ (b) the MMI with $L = 1055\mu m$

The procedure used to measure the power imbalance is very similar to the one used to measure phase error :

- Detect the maximum of each peak. To increase precision, a fit is made for each peak with a cosine function. The fit is made over only one period to increase peak maximum determination instead of position contrary to the fit for phase error.
- The n^{th} peak of channel A is taken as reference. Peak number n for the other channels are the ones comprised between the n^{th} and $n + 1^{\text{th}}$ peaks of channel A.
- The CMRR for channel A versus B is then : $CMRR_{A-D} = 20 \cdot \log_{10}\left(\frac{|P_A - P_D|}{P_A + P_D}\right)$. The CMRR for channel B versus C is obtained by substitution. Note that this CMRR is slightly different from the definition in equation 2.63 as the inputs could not be injected separately with the device at hand. The actual CMRR should be slightly better than the one described here.

Power imbalance in function of wavelength for die #2 are presented in figure 2.50. In this specific case, the short MMI is a bit more balanced than the long one, with the CMRR lower than -20dB on almost the whole wavelength range.

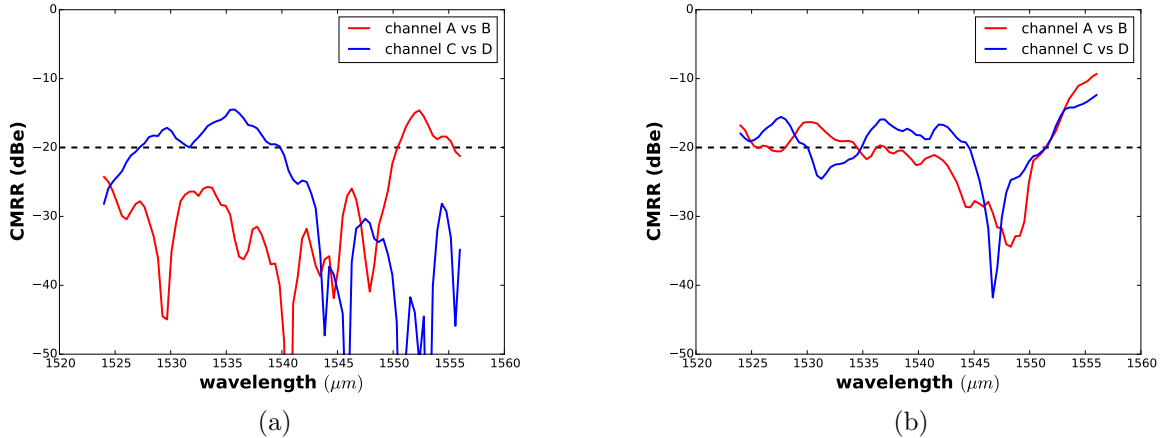


FIGURE 2.50: Measured CMRR on die #2 for (a) the MMI with $L = 99\mu\text{m}$ (b) the MMI with $L = 1055\mu\text{m}$

The results presented above and their conclusion hold for the measured die. But variations from die to die can be very large. In order to characterise those deviations, a short statistical study was made on the five dies that were measured.

Every die received the treatment described above. For each MMI and for each channel, the fraction of the curve that is in the acceptable zone was retrieved. This "acceptable" zone is set at $\pm 5^\circ$ for the phase error and below -20dB for the CMRR. For instance, a measured point with a phase error between -5° and $+5^\circ$ will be counted as an "acceptable point" [34, 36]. Any measured point beyond that windows is considered as a "bad point". The fraction of "acceptable" points for phase error and power imbalance are presented in figure 2.51. For the phase error, the results were averaged on all 3 channels. The error bar indicates the spread from channel to channel.

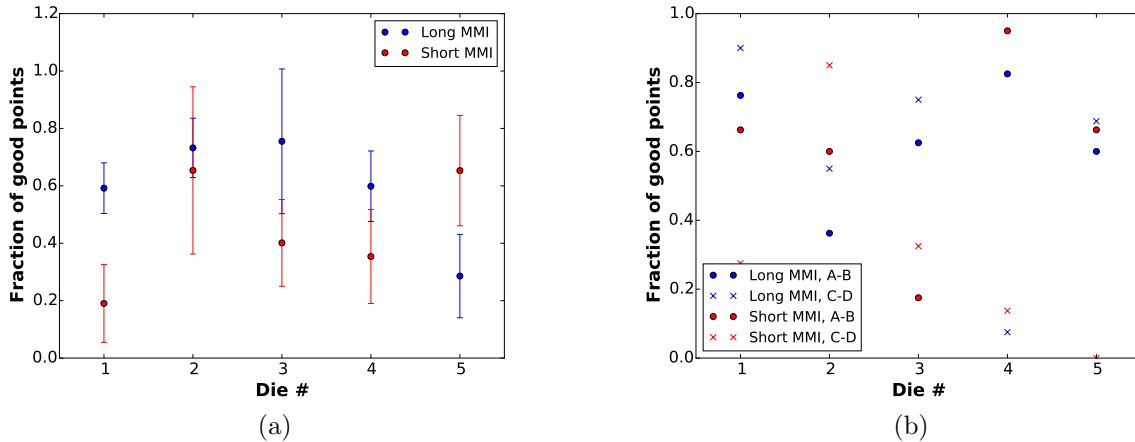


FIGURE 2.51: Statistical analysis on 5 dies of the hybrid 90 MMI. (a) Phase error analysis. The error bars refer to the variation from channel to channel. (b) Power imbalance

The analysis shows that the long MMI has, on average, a better result regarding the phase error and with smaller variations. The short MMI can potentially provide better results than the long one, as described by the simulation and measurement on die #2, but the short design is much more sensitive to fabrication variations. Power imbalance on the other hand shows no real difference between the long and short MMI. They both have large variations in the zone of interest.

Conclusion

MMI are good candidates for the hybrid 90° function. The shorter type of MMI seems at first to give better results than the long one, but a very large discrepancy in results due to fabrication variations mitigates the interest of this design at the time being. For that reason, long MMI are preferred for the integration in coherent receivers. The performances are good enough for real applications, although the spectral bandwidth in which the device works fine might be smaller.

2.10 Conclusion

Throughout this chapter, many passive components have been studied, from the basic waveguide to the more complex hybrid 90°. It was demonstrated that the silicon platform provides a good environment for the fabrication of these passive building blocks. The strong index contrast between silicon and silica was able to provide the perfect waveguide for very compact devices with good performances.

A summary of the main highlights of this chapter is described below :

- Strip and rib waveguides with a characterisation of the propagation losses. Losses are 1.4dB/cm for rib waveguides and below 4dB/cm for strip waveguides.
- Various Bends with a comparison between simulation results and measurement results. The losses in the optimised bends are very small compared to the waveguide propagation losses.
- Waveguide crossings with measured losses lower than 0.3dB per crossing and a crosstalk larger than 40dB.
- Power splitters in the form of multimode interferometers and directional couplers.
- Hybrid 90° in the form of 4×4 MMI. Two designs were compared, both by simulation and measure. The reported performances are compatible with the use in coherent receivers.

Each of these components was designed to be integrated in more complex devices such as coherent receivers, modulators or lasers as will be explained in the next chapters.

References

- [1] W. BOGAERTS et al. “Silicon-on-Insulator Spectral Filters Fabricated With CMOS Technology”. In : *IEEE Journal of Selected Topics in Quantum Electronics* 16.1 (jan. 2010), p. 33–44.
- [2] P. DESIGN. *The FMM solver*. URL : https://www.photond.com/products/fimmwave/fimmwave_features_21.htm (visité le 31/08/2016).
- [3] P. DESIGN. *The FDM solver*. URL : https://www.photond.com/products/fimmwave/fimmwave_features_22.htm (visité le 31/08/2016).
- [4] *Photon Design Fimmwave/Fimmprop version 2.0*.
- [5] F. PAYNE et J. LACEY. “A theoretical analysis of scattering loss from planar optical waveguides”. In : *Optical and Quantum Electronics* 26.10 (1994), p. 977–986.
- [6] K. K. LEE et al. “Effect of size and roughness on light transmission in a Si/SiO₂ waveguide: Experiments and model”. In : *Applied Physics Letters* 77.11 (2000), p. 1617–1619.
- [7] W. BERGLUND et A. GOPINATH. “WKB analysis of bend losses in optical waveguides”. In : *Journal of lightwave technology* 18.8 (2000), p. 1161.
- [8] E. MARCATILI. “Bends in optical dielectric guides”. In : *Bell System Technical Journal* 48.7 (1969), p. 2103–2132.
- [9] M. HEIBLUM et J. HARRIS. “Analysis of curved optical waveguides by conformal transformation”. In : *IEEE Journal of Quantum Electronics* 11.2 (fév. 1975), p. 75–83.
- [10] J. P. HUGONIN et P. LALANNE. “Perfectly matched layers as nonlinear coordinate transforms: a generalized formalization”. In : *JOSA A* 22.9 (2005), p. 1844–1849.
- [11] J. LELONG-FERRAND et ARNAUDIÈS. *Géométrie et Cinématique*. Dunod, 1977.

- [12] L. WELLER-BROPHY et D. HALL. “Analysis of waveguide gratings: application of Rouard’s method”. In : *JOSA A* 2.6 (1985), p. 863–871.
- [13] K. O. HILL et G. MELTZ. “Fiber Bragg grating technology fundamentals and overview”. In : *Journal of lightwave technology* 15.8 (1997), p. 1263–1276.
- [14] H. CHEN et A. W. POON. “Low-loss multimode-interference-based crossings for silicon wire waveguides”. In : *IEEE photonics technology letters* 18.21 (2006), p. 2260–2262.
- [15] Y. ZHANG et al. “A compact and low loss Y-junction for submicron silicon waveguide”. In : *Optics express* 21.1 (2013), p. 1310–1316.
- [16] L. B. SOLDANO et E. C. M. PENNING. “Optical multi-mode interference devices based on self-imaging: principles and applications”. In : *Journal of Lightwave Technology* 13.4 (avr. 1995), p. 615–627.
- [17] P. A. BESSE et al. “Optical bandwidth and fabrication tolerances of multimode interference couplers”. In : *Journal of Lightwave Technology* 12.6 (1994), p. 1004–1009.
- [18] R. HANFOUG et al. “Reduced reflections from multimode interference couplers”. In : *Electronics Letters* 42.8 (2006), p. 1.
- [19] K. OKAMOTO. *Fundamentals of optical waveguides*. Academic press, 2010.
- [20] A. YARIV. “Coupled-mode theory for guided-wave optics”. In : *IEEE Journal of Quantum Electronics* 9.9 (1973), p. 919–933.
- [21] W.-P. HUANG. “Coupled-mode theory for optical waveguides: an overview”. In : *JOSA A* 11.3 (1994), p. 963–983.
- [22] W. BOGAERTS et al. “Silicon microring resonators”. In : *Laser & Photonics Reviews* 6.1 (2012), p. 47–73.
- [23] Q. XU et al. “Micrometre-scale silicon electro-optic modulator”. In : *nature* 435.7040 (2005), p. 325–327.
- [24] M. PANTOUVAKI et al. “50Gb/s Silicon Photonics Platform for Short-Reach Optical Interconnects”. In : *Optical Fiber Communication Conference*. Optical Society of America. 2016, Th4H–4.
- [25] K. XU et al. “56 Gbit/s DMT Signal Generated by an Integrated Silicon Ring Modulator”. In : *CLEO: Science and Innovations*. Optical Society of America. 2016, STu1G–7.
- [26] A. YARIV. “Critical coupling and its control in optical waveguide-ring resonator systems”. In : *IEEE Photonics Technology Letters* 14.4 (2002), p. 483–485.
- [27] A. W. POON et al. “Cascaded microresonator-based matrix switch for silicon on-chip optical interconnection”. In : *Proc. IEEE* 97.7 (2009), p. 1216–1238.
- [28] D. G. RABUS. *Integrated ring resonators*. Springer, 2007.
- [29] M.-C. TIEN et al. “Silicon ring isolators with bonded nonreciprocal magneto-optic garnets”. In : *Optics express* 19.12 (2011), p. 11740–11745.

- [30] S. GHOSH et al. “Ce: YIG/Silicon-on-Insulator waveguide optical isolator realized by adhesive bonding”. In : *Optics express* 20.2 (2012), p. 1839–1848.
- [31] Y. SHOJI et al. “Magneto-optical isolator with silicon waveguides fabricated by direct bonding”. In : *Applied physics letters* 92.7 (2008), p. 071117.
- [32] Y. SHOJI et al. “MZI optical isolator with Si-wire waveguides by surface-activated direct bonding”. In : *Optics express* 20.16 (2012), p. 18440–18448.
- [33] A. TALNEAU et al. “Atomic-plane-thick reconstruction across the interface during heteroepitaxial bonding of InP-clad quantum wells on silicon”. In : *Applied Physics Letters* 102.21, 212101 (2013).
- [34] R. HALIR et al. “High-performance 90 hybrid based on a silicon-on-insulator multimode interference coupler”. In : *Optics letters* 36.2 (2011), p. 178–180.
- [35] R. KUNKEL et al. “First monolithic InP-based 90-hybrid OEIC comprising balanced detectors for 100GE coherent frontends”. In : *Indium Phosphide & Related Materials, 2009. IPRM'09. IEEE International Conference on*. IEEE. 2009, p. 167–170.
- [36] J. FANDINO et P. MUÑOZ. “Manufacturing tolerance analysis of an MMI-based 90 optical hybrid for InP integrated coherent receivers”. In : *IEEE Photonics Journal* 5.2 (2013), p. 7900512–7900512.
- [37] H. YAGI et al. “High-efficient InP-based balanced photodiodes integrated with 90 hybrid MMI for compact 100 Gb/s coherent receiver”. In : *Optical Fiber Communication Conference*. Optical Society of America. 2013, OW3J–5.
- [38] L. ZIMMERMANN et al. “C-band optical 90-hybrids based on silicon-on-insulator 4 × 4 waveguide couplers”. In : *IEEE Photon. Technol. Lett* 21.3 (2009), p. 143–145.
- [39] J. HUANG, R. SCARMOZZINO et R. OSGOOD. “A new design approach to large input/output number multimode interference couplers and its application to low-crosstalk WDM routers”. In : *IEEE Photonics Technology Letters* 10.9 (1998), p. 1292–1294.

Chapter 3

Wavelength Division Multiplexing : passive devices

WAVELENGTH division multiplexing (WDM) is a key technology to increase transmission capacity (see chapter 1) as the data rate is multiplied by the number of multiplexed wavelengths. One of the main factors in this technology is the ability to split and multiplex wavelengths without interaction between channels, all that with limited insertion losses and crosstalk.

There are two main flavours of WDM technology. The first focalises on increasing the number of wavelengths in a limited bandwidth and is thus called dense WDM (DWDM). It has channel spacings expressed in GHz varying from 25GHz[1, 2] to more than 800GHz[3], with a high channel number going up to 256 channels [1, 2]. The most common product however is the 100GHz spacing wavelength multiplexer (WM). They are commercially available at many companies in large quantities [4, 5]. They are nowadays used mostly for metro and long-haul transmissions.

The second category has a reduced number of channels but with an emphasis on robustness. They have a very large channel spacing, usually expressed in nm, and take advantage of flattened transfer function in order to be more resilient to variations in temperature and wavelength shifts. This category is called coarse WDM (CWDM). The most common spacing reported is 20nm in the C-band. That device is also commercially available [6].

In order to realise the wavelength multiplexers necessary for the WDM technology, two effects can be used by integrated photonics. The first way is to use tailored interferences and phase delays in waveguides to create the filtering function. Ring resonators and Mach-Zender interferometers enter in that category. The other one uses diffraction through a free propagation region mixed with tailored phase delays. Arrayed waveguide gratings (AWG) and echelle gratings (EG) are the main candidates of this category.

Table 3.1 and 3.2 shows the performances of a few selected DWDM and CWDM wavelength multiplexers on the InP, silicon and silica platforms. One can see that the InP and Silica platform give outstanding results for both the DWDM and CWDM applications. The performances on thin silicon are still to be improved. This chapter will present some new

results which make the state of the art on this specific platform.

Material	Channel spacing	Insertion losses (dB)	crosstalk (dB)	Channel number	footprint	flat top
Echelle Grating DWDM						
SOI [7]	800 GHz	3	30	4	$400 \times 400 \mu m^2$	no
SOI ¹	100 GHz	2	15	16	$2 \times 1.3 mm^2$	no
InP [8]	100 GHz	5.5	30	48	$2.5 \times 8.8 mm^2$	yes
Silica [2]	25 GHz	4	35	256	$20 \times 40 mm^2$	no
Arayed Waveguide Grating DWDM						
thick SOI [9]	50GHz	5-6	15-25	64	$10 \times 3 mm^2$	no
500nm SOI [10]	100GHz	3	15	40	-	no
SOI [11]	200GHz	3	17	16	$700 \times 400 \mu m^2$	no
InP [12]	200GHz	0	40	8	$2.5 \times 3.5 mm^2$	no
InP [13]	50GHz	-	20	64	$3.6 \times 7.0 mm^2$	no
Silica [1]	25GHz	4.7	40	256	$74 \times 50 mm^2$	no
Other DWDM						
SOI [14]	100GHz	n.a.	18dB	8	$800 \times 200 \mu m^2$	yes
SOI ²	100GHz	3dB	8	15dB	$400 \times 100 \mu m^2$	no

TABLE 3.1: Performances for different designs ; 1 : see section 3.2.3 ; 2 : see section 3.1

Material	Channel spacing	Insertion losses (dB)	crosstalk (dB)	Channel number	footprint	flat top
Echelle Grating CWDM						
thick SOI [15]	8nm	1.7	25	12	$6 \times 5 mm^2$	yes
SOI [16]	20nm	7.5	30	4	$280 \times 150 \mu m^2$	no
SOI ¹	20nm	5	15	4	$200 \times 200 \mu m^2$	yes
Other CWDM						
Polymer [17]	20nm	6	15	5	$25 \times 50 mm^2$	no
SOI [18]	4.5nm	4dB	15dB	8	$1 \times 1 mm^2$	no
SOI [19]	20nm	2dB	13dB	4	$1.2 \times 10^{-3} mm^2$	yes

TABLE 3.2: Performances for different designs ; 1 : see section 3.2.2

This chapter will focus on the design and measurement of wavelength (de)-multiplexer components. The first part will study a practical case of a ring resonator demultiplexer. Part

2 is about EG for both CWDM and DWDM applications. The third part will focus on AWG, including discussion on modelling and measurement results.

3.1 Ring resonators (de)-multiplexer

A ring resonator provides a periodic spectral response with sharp peaks. It is possible to design the ring’s parameters to fix the ring’s wavelength and free spectral range (FSR) (see section 2.6 for more on single ring resonators). The idea is then to use multiple rings, one for each wavelength, with slightly different lengths and therefore wavelength and set them in serial, each ring coupled to a main ”bus” waveguide [20]. Each wavelength is extracted by its respective ring and dispatched to the drop port (see Fig. 3.1). This configuration was reported previously on the SOI platform in [21].

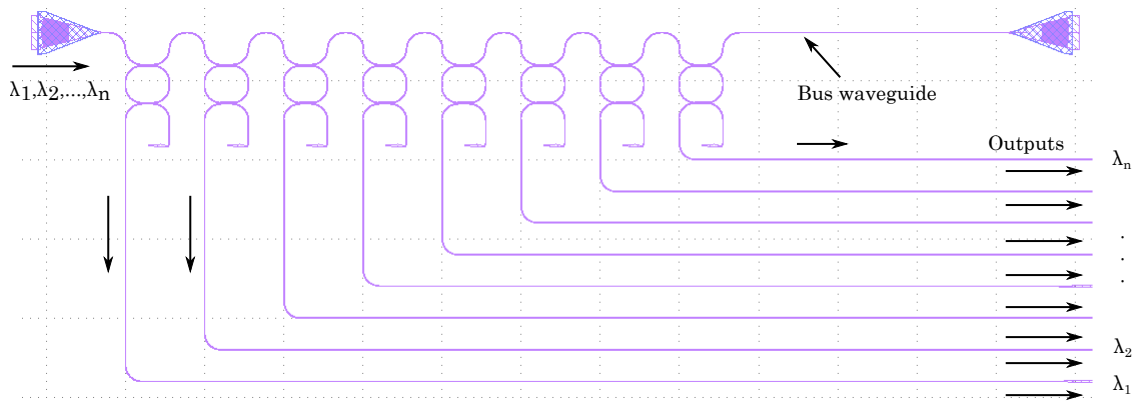


FIGURE 3.1: Layout of a $8 \times 100GHz$ cascaded ring resonator demultiplexer

We fabricated a ring-resonator based demultiplexer with $8 \times 100GHz$ channel spacing. The rings were tuned to have an FSR slightly larger than $800GHz$ with a very high finesse. In order to realise the very low bend radius ($10\mu m$), all rings were realised with strip waveguides with a “racetrack” geometry.

The measured spectra are shown in figure 3.2. The component displays low insertion losses, with all channels at almost $0dB$, along with more than $15dB$ crosstalk. The only exception is for channel 8. This last channel overlaps with the first channel and is therefore very attenuated and with a non-regular shape. This is because the channel spacing between all channels is not $100GHz$ but larger. The inter-channel spacing was measured for each pair of adjacent rings. The aggregated spacing is $121 \pm 22GHz$ compared to the designed $100GHz$. The measured spacing is much larger than the designed spacing with a large standard deviation. As a result, the N^{th} order of the 8^{th} ring coincides with the $N-1^{th}$ order of the first ring. All the power that should have been extracted by the 8^{th} ring was already extracted by the first. Fabrication uncertainties are probably the root of these deviations. A thermal tuning [14] or waveguide trimming [22] of each ring could tune each ring at the exact desired position.

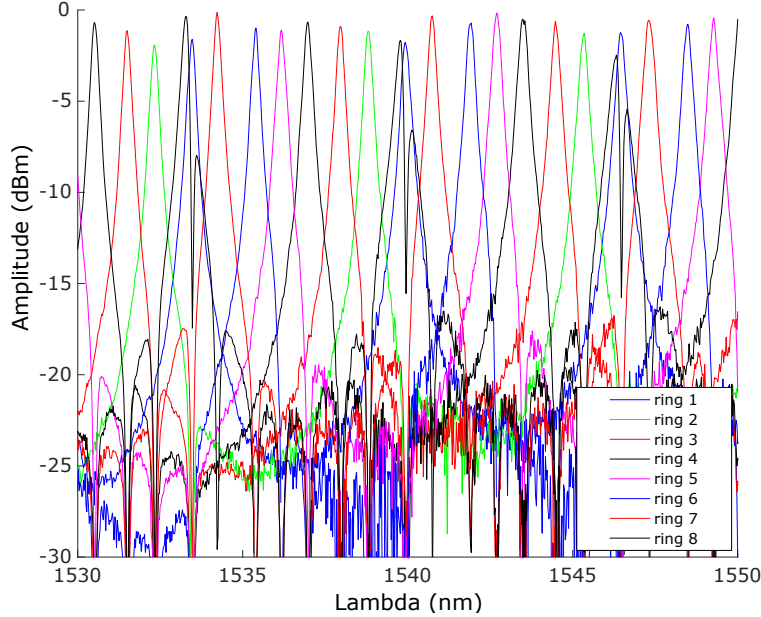


FIGURE 3.2: Measured transmission of $8 \times 100GHz$ cascaded ring resonator demultiplexer without thermal tuning after normalisation by fiber grating couplers.

Flattened top WM that use high-order coupled ring resonator to realise the flattening function have been reported [14, 23]. Thermal tuning is applied on each ring just as in our configuration.

As a conclusion, ring resonators can make an efficient WM with low losses, flattened tops and low channel spacing with a record small footprint. On the other hand, the channel spacing is not always respected because of fabrication uncertainties on waveguide width and silicon layer thickness. Each ring needs to be individually tuned through thermal effects or waveguide trimming, mitigating the interest of such a component for WDM applications.

3.2 Echelle grating

Echelle gratings (EG) are one of the two main kinds of WM using diffraction mixed with interferences from different light paths. It relies on diffraction through a free propagation region (FPR) along with a tailored mirror designed to refocus the beam at a given position dependant on the wavelength. These designs are appreciated for their small footprint and their robustness to fabrication variations. Many designs have been proposed on various platforms such as Silica [2] InP [8] or SOI [3], both for DWDM and CWDM [15, 16] applications

During my thesis, EG design for both DWDM and CWDM applications have been implemented. The results are displayed in section 3.2.3 and 3.2.2 respectively. All calculations and simulations on EGs presented in this section were made with the help of the commercial software eppiprop from the photon design company [24], often complemented with the

fimmprop module from the same company [25].

3.2.1 Theory

The simplest and most common type of EG is the Rowland configuration. In that configuration, the inputs and outputs are placed on a circle, called the Rowland circle, with a radius R and center O . A mirror is placed tangent to the Rowland circle with a radius of $2R$ and center O' . Such a layout focuses any point from the Rowland circle to another point also on that same circle, independent of the wavelength. To determine that point, one must calculate the condition of constructive interference. Notations are presented on schematic 3.3. R is the Rowland circle radius, α and β_l the angles of input and output, respectively represented as point A and B_l . λ is the optical wavelength and n_{eff} the effective index of the propagating mode in the FPR.

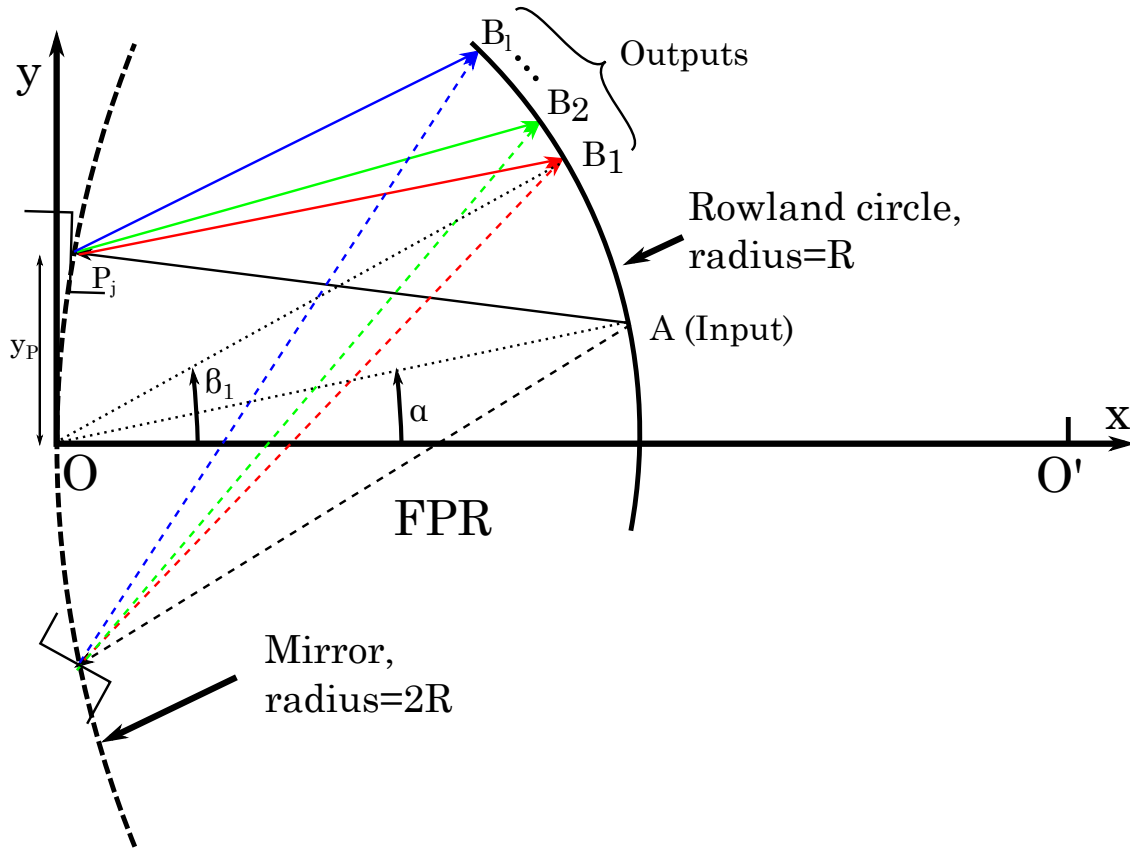


FIGURE 3.3: Schematic of an Echelle grating with ray-optic illustration

The path difference between rays passing by the origin O and point P_j can be expressed as :

$$\Delta L = AP_j + P_j B_l - (AO + OB_l) \quad (3.1)$$

The coordinates of points A and B_l can be expressed in the coordinate system :

$$\begin{cases} x_A = 2.R. \cos^2 \alpha \\ y_A = 2.R. \cos \alpha. \sin \alpha \end{cases} \quad (3.2)$$

$$\begin{cases} x_{B_l} = 2.R. \cos^2 \beta_l \\ y_{B_l} = 2.R. \cos \beta_l. \sin \beta_l \end{cases} \quad (3.3)$$

and the distance square from the center of the grating circle to the point $P_j(x_P, y_P)$:

$$(x_P - 2.R)^2 + y_P^2 = 4.R^2 \quad (3.4)$$

Using the paraxial approximation $y_p \ll R$, the path difference can finally be expressed as :

$$\Delta L = -(\sin \alpha + \sin \beta_l).y_P \quad (3.5)$$

The condition of constructive interference is then :

$$n_{eff}.(\sin(\alpha) + \sin(\beta)).y_P = k.m.\lambda \quad (3.6)$$

with n_{eff} the effective index in the FPR, m the diffraction order and k the grating order. The diffraction order corresponds to the phase difference caused by the facets of the mirror while the grating order corresponds to the phase delay caused by the FPR. Equation 3.6 can be re-written as :

$$n_{eff}.(\sin(\alpha) + \sin(\beta)).d = m.\lambda \quad (3.7)$$

with $d = y_P/k$ which can be interpreted as the distance in the y-direction between adjacent constructive interference points [20].

In order to maximise transmission from the input to the outputs, the mirror is split in multiple facets, each oriented to reflect the light from the input to the output array. The center of each facet is placed at points of constructive interferences and the end of the facet where destructive interferences occur [26]. As such, d can also be interpreted as the grating's period.

Relation 3.6 is however valid only with the paraxial approximation. Further calculations are required to correct aberrations for larger angles [20], which are often required in the realisation of EGs. The full calculation requires to calculate the corrected position of constructive and destructive interferences and then adapt the length and position of each facet in consequence. The resulting setup is called a chirped grating.

In a very pragmatic way, one can say an EG makes an image of the input guide's profile in front of the output guide's array profile, with a position varying as a function of the wavelength. The transmitted power in a given channel is then related to the overlap between the image of the input's profile and the output's profile.

This article from photon design [26] gives a few rules that should be applied in order to achieve the best performances :

- Choose the diffraction order so that the FSR is greater than the spectral range of the device, with $FSR = \lambda/m$ [27].
- Place the input and output as close as possible, at the largest angle possible in order to maximise focalisation point's shift with wavelength. In other words, α and β_i must be very close together and with the largest value possible.
- Use shorter facets so that the wavefront is more homogeneous by choosing a lower diffraction order. The result is a better channel uniformity. But shorter facets are not without drawbacks : more facets means more possibilities for shadowing and extra-reflexions, in addition to being harder to implement and fabricate.
- Make sure the grating is always large enough to reflect most of the incident field.
- Minimise crosstalk between adjacent waveguides, usually by placing them further apart.
- Maximise transmission between the incident waveguide and the FPR. To do so, the waveguide must have a low confinement. This point contradicts with the previous point.

3.2.2 Echelle grating for Dense WDM applications

The main goal of this section is to demonstrate the performances EGs through simulation and experimentation, to prove that EG can solve the challenge of DWDM applications. The main design presented here is aimed at the C-band with 16 channels spaced 100GHz. No echelle grating on the thin SOI platform has been reported earlier and no AWG was able to match the performances presented here.

Design

All notations in this section are defined in previous section 3.2.1. The EG was optimized for 16 channels centered around a wavelength of 1540nm with an inter-channel spacing of 100GHz. In our designs, 6 additional channels were added, 3 on each side, in order to provide a similar environment for all channels during the fabrication process. The Rowland mounting has a radius of $1000\mu\text{m}$. This large radius was chosen in order to enable large RIB waveguides at input and output ($1.5\mu\text{m}$ large). A large guide will have a good overlap with the FPR, thus giving lower insertion losses. But on the other side, light can couple from one guide to the other where guides are tightly spaced, which gives a degraded crosstalk. The waveguide width and separation are optimised in order to achieve low insertion loss and low crosstalk.

The simulation uses a chirped grating designed to reflect the 20th diffraction order of the EG. Each reflecting facet of the EG is a Bragg mirror, but taken as a perfect mirror during simulation. The Bragg mirror is fully etched with a period of 300nm set to have a maximum reflection at 1540nm. Such a grating provides a very large bandwidth ($>100\text{nm}$), and is thus very robust to fabrication variations. The input guide is positioned at an angle $\alpha = 44^\circ$ and the output guides are centered around $\beta_i = 45^\circ$. Our design respects the rule that advises to place *Place the input and output as close as possible, at the largest angle possible..* Inputs and outputs are formed by tapered waveguides. The module Fimmprop in conjunction with Eppipro was used to take into account crosstalk between the different output tapers.

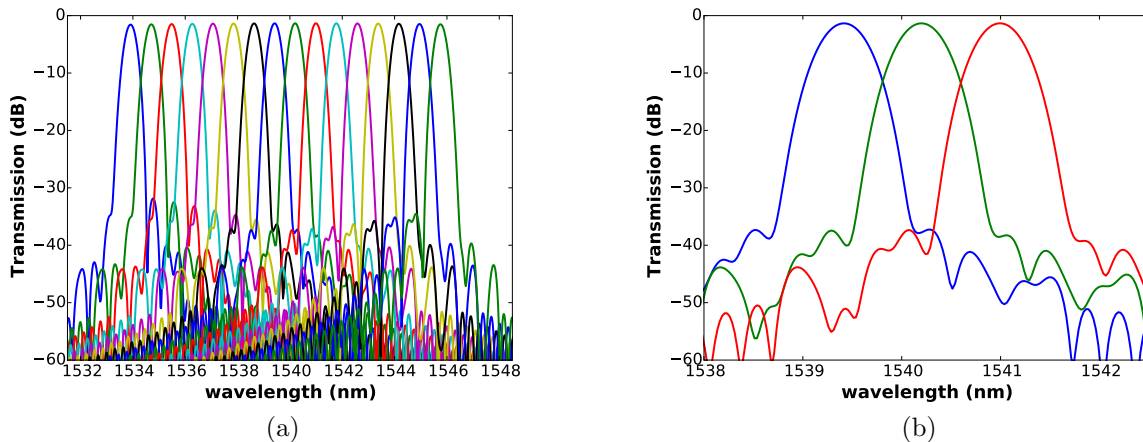


FIGURE 3.4: (a) Simulated EG 16×100 GHz spectrum (b) Zoom on the center channels

The simulation results are shown on Fig.3.4 for 16 channels. Insertion losses have values between -1.45dB and -1.8dB, giving a channel uniformity better than 0.5dB. The crosstalk achieves nearly 29dB for the considered 16 channels.

The fabrication was made in Leti's 300nm silicon platform with the process described in 1.3.1. Figure 3.5a shows a picture of the overall design with optical microscope. Fig.3.5b zooms on the input/output section. Each input and output is linked to a FGC used for measurements. Fig 3.5c shows a scanning electron microscope (SEM) image of the EG, with a zoom in Fig.3.5d. The Bragg-grating used for each facet is clearly visible and well-defined.

Measurement results

Passive testing of the component was made using a 12-inch semi-automated prober in the DEMUX configuration. The light is coupled on one side of the device with single mode fiber set vertically with a 11.5° tilt, whereas the output signal is collected with a 16 fibers array with a $250 \mu\text{m}$ pitch. As visible from the Fig.3.5a, this pitch doesn't match with the output FGC spacing of $50 \mu\text{m}$ chosen initially for more compactness. The channels were thus monitored one-by-one on this section. Automatic alignment calibration routines are used in order to couple a maximum power to each fiber using a laser source Agilent AG8164B and its complementary photodetector 81634B. Every channel was normalized by the FGC spectral response in order to obtain the transfer function from the EG only.

The measured transmission responses are shown in Fig. 3.6a. Insertion losses are below 2 dB for all channels, with a uniformity better than 1 dB across the whole spectrum. The crosstalk in an EG is very sensitive to the non-uniformity of the thickness of the silicon guiding layer in the free propagation region [28], which explains the measure of 13-15 dB crosstalk instead of the 27 dB from the simulations and the shift of the spectrum from the designed 1540nm to 1543nm. In our EG, the free propagation region has a diameter of $2000 \mu\text{m}$. The variations of the thickness of the silicon guiding layer in the FPR can therefore

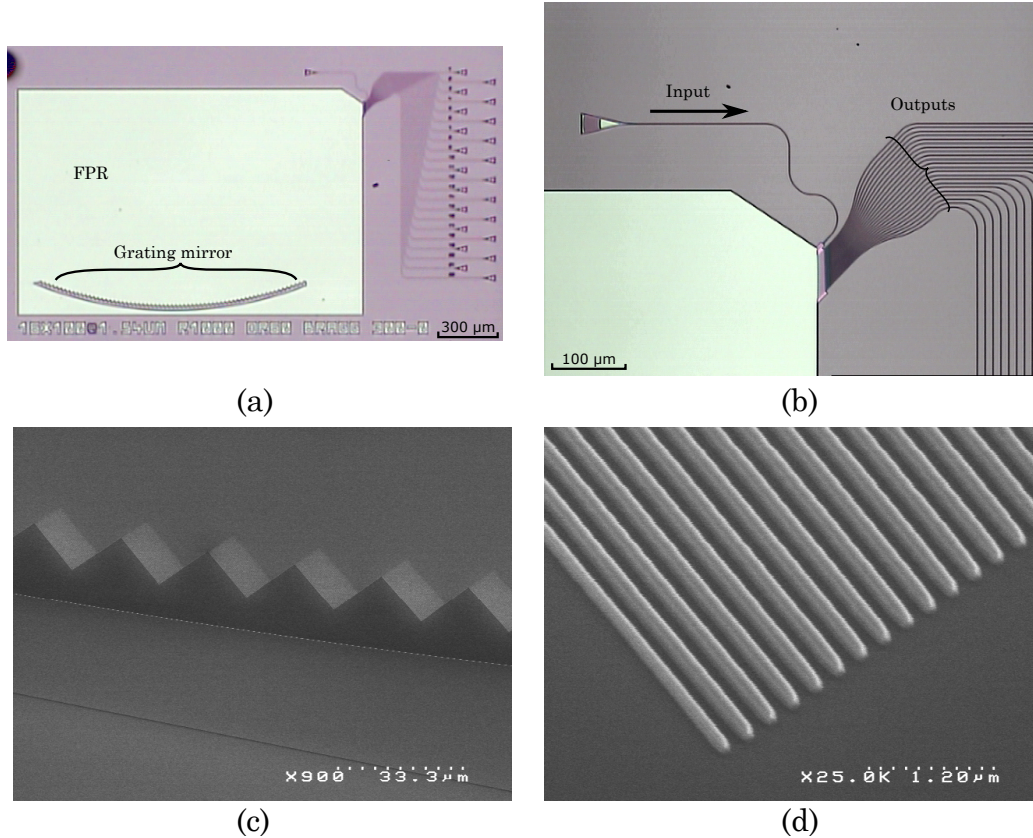


FIGURE 3.5: (a) Optical microscope view of complete design (b) Optical microscope zoom on input/output guides (c) scanning electron microscope (SEM) view of the grating (d) SEM zoom on one period of the grating

explain the difference in crosstalk between simulation and experiment. Parasitic reflections on the grating and/or the sides of the FPR can also further degrade the crosstalk.

In order to determine accurately the channel spacing, a Skew function is used to fit each channel in order to determine most probable peak position (see Fig. 3.6b). Inter-channel spacing was calculated by measuring the difference of position between two adjacent channels. A statistic was then made on all obtained results and give an inter-channel spacing of $100.1 \pm 1.9\text{GHz}$ and an aggregated 3dB bandwidth of $26.0 \pm 0.8\text{GHz}$ ($0.195 \pm 0.006\text{nm}$). A flattened response could be obtained with an optimisation of input and output waveguides, but at the cost of higher insertion losses [7].

A similar study was performed for applications at $1.3\mu\text{m}$. All principles explained earlier were reproduced, with results very similar to the ones in the C-band. The final spectrum is presented on Fig.3.7.

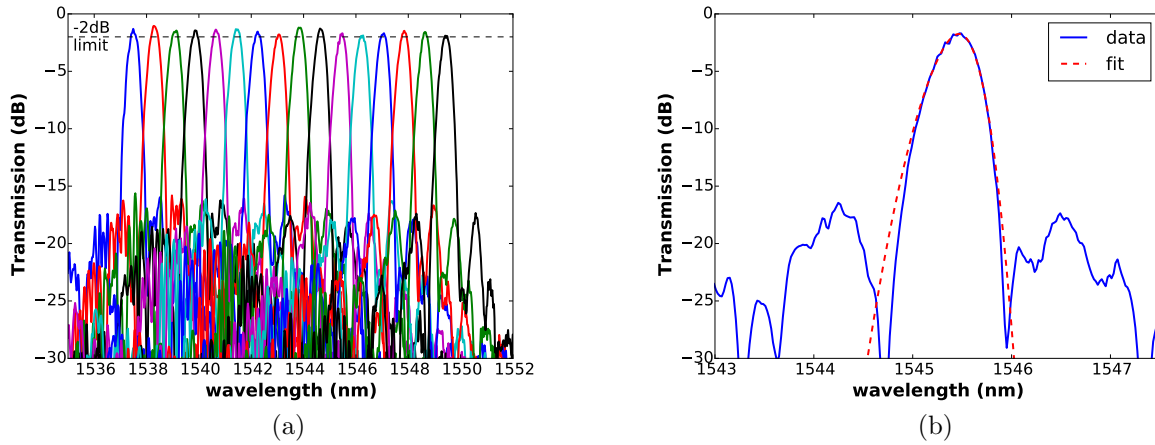


FIGURE 3.6: (a) Measured spectra for 16 channels after normalisation by vertical coupler for presented Echelle grating at $1.5\mu\text{m}$; (b) Zoom on 11th peak (full) with superimposed fit (dashed)

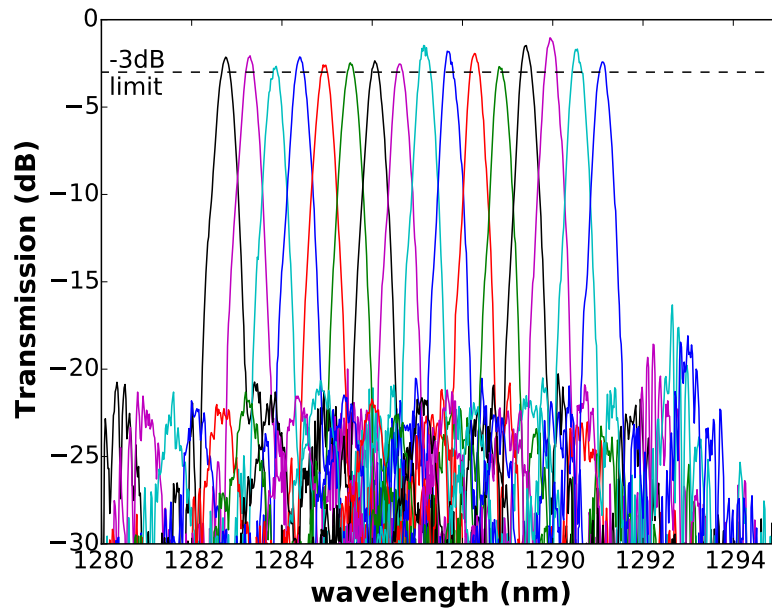


FIGURE 3.7: Measured spectra for 16 channels after normalisation by vertical coupler for presented Echelle grating at $1.3\mu\text{m}$

3.2.3 Echelle grating for Coarse WDM applications

In this section, the focus will be on simulation and measure of an echelle grating designed for CWDM applications in the O-band. The goal is to get performances close to the commercial specifications of a 4 channels, 20nm flattened top CWDM. The target specifications are summarised in table 3.3

specification	Target Value	Achieved value
Channel spacing	20nm	20nm
Center wavelength	1300nm	1310nm
inter-channel uniformity	0.5dB	~ 1dB
flat top width	13nm	10nm
Max. variation in the flat top	0.5dB	~2dB
Max. insertion loss	2.7dB	5dB
Crosstalk adjacent channels	18dB	15dB
Crosstalk other channels	25dB	20dB

TABLE 3.3: Comparaision of MMI and Directionnal couplers as power splitters

Design

As said in section 3.2.1, one can view an EG as an optical apparatus that makes an image of the input guide in front of the output guide array, with its position shifting with wavelength. The final channel response is then given by the overlap of the input image with the fundamental modes of the output waveguide. A minimum insertion loss is then obtained when the input image and output modes are identical and overlap perfectly. A common way of flattening the device’s response is therefore to use a MMI at the input and tailor it to produce a flat profile [7, 29]. But this comes at the cost of larger insertion losses as the input image profile is much larger than the output profile, thus limiting the maximum overlap.

In this section, a different approach to flatten the component’s response while keeping reasonable crosstalk and insertion losses is developed. To do that, MMI replace traditional waveguides at both input and output. They have carefully tailored profiles (see Fig 3.8), one with a dip in the middle (“dip” configuration) and the other with a peak (“peak” configuration).

From these simulation, we can extract the transfer matrix of each MMI, or in other words how much power with how much phaseshift is transferred from the eigenmodes on the waveguide end (left side of simulation in figure 3.8) to the eigenmodes on the FPR end of the MMI (right side of simulation in figure 3.8). The power transmitted to the fundamental mode at the waveguide end of the output MMI is proportional to the overlap between the incident field profile and the profile at the FPR end of the MMI.

The profile in front of the output MMI is no other than the image of the input MMI with a position shifting with wavelength. The “dip and peak” configuration ensures a constant overlap as the input profile is shifted in front of the output MMI. The steep profile on the

sides will on the other hand ensure a fast decrease of the overlap beyond the window of interest, which provides in turn a good crosstalk.

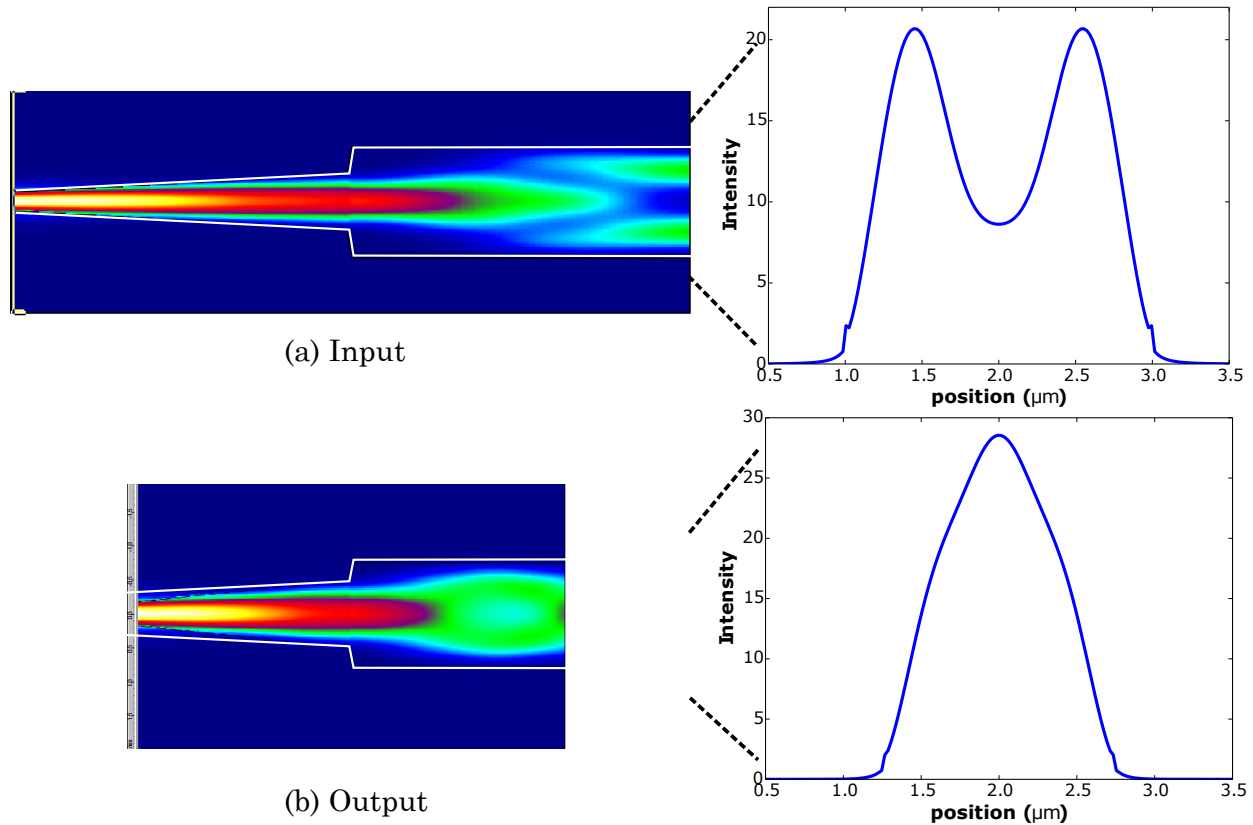


FIGURE 3.8: Intensity profiles of (a) the input MMI (b) the output MMI. The left column is a top view along with propagation in the MMI. The right column shows the intensity profile after the propagation.

The design of the elementary configuration of the EG follows the recommendations given in section 3.2.1. As such, we used a Rowland configuration with a radius of $50\mu\text{m}$. The simulation uses a perfect chirped grating; each reflecting facet of the EG is a Bragg mirror. In the fabricated device, each facet is made of a half-etched Bragg mirror. The very high index contrast between the silicon and silica enables us to create a high reflectivity mirror with a bandwidth larger than 100nm . The simulated spectrum is given figure 3.9a. A zoom on 2nd peak is given in figure 3.9b. This spectrum exhibits insertion losses better than 3dB, with a 0.5dB bandwidth of 13nm . Inter-channel uniformity is better than 0.5dB. The crosstalk is defined as the minimum difference between interest channel and other channels across said bandwidth. It is better than 15dB on the whole bandwidth for this simulation.

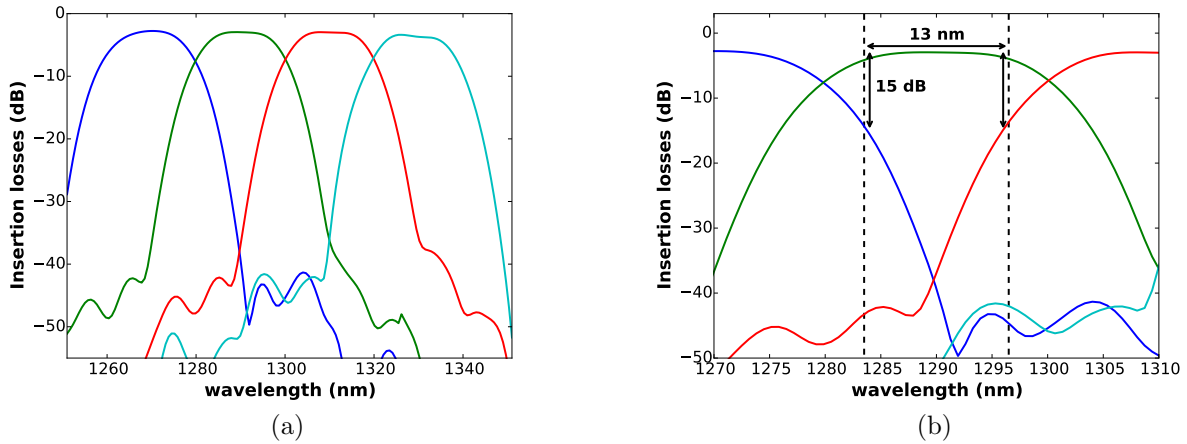


FIGURE 3.9: (a) Simulation of component spectrum ; (b) Zoom on 2nd peak

Static test

The fabrication of the device was performed on the 300nm platform from ST micro-electronics. In order to enable large scale measurement, each input and output of the component were linked to fiber grating couplers (FGC). But these FGC have a 3dB bandwidth of about 45nm, compared to the 100nm wavelength window that is necessary for the measurement. In order to get some signal at both ends of the spectrum, a tilt-orientable fiber was used in order to shift the FGC's spectrum at the central wavelength (1300nm). In that way, all channels transmit enough power to be above noise level, but the outermost part of the spectrum have a much higher noise and lower precision than the center part.

Measurement results are shown Fig. 3.10. The exhibited spectrum was normalised by the transmission of a FGC with the optical fiber tilted at 15°. The component shows insertion losses around 5dB with a flattened top close to the one predicted by simulation. This design has a 3dB bandwidth of around 14nm with a crosstalk around 10dB. But the crosstalk is improved up to 15dB if taking a reduced window around 10nm. inter channel uniformity is around 1dB. For comparison purpose, commercial CWDM components exhibit a 0.5dB bandwidth of 13nm, crosstalk better than 15dB , and insertion losses lower than 2.5dB [6]

Thermal variations

The main purpose of flattened CWDM EG is to make a component that requires no thermal control. A thermal measurement was performed to get information on that aspect. The experimental setup is the same as in part 3.2.3, with the difference that the component is heated at an arbitrary temperature with a thermo-electric heater. The 2nd peak was measured for temperatures varying between 20 and 90 degrees Celsius. Each peak was then fitted with a “soft door” as described in equation 3.8, with λ the wavelength and main variable. λ_0, M, w and s are the fit variables.

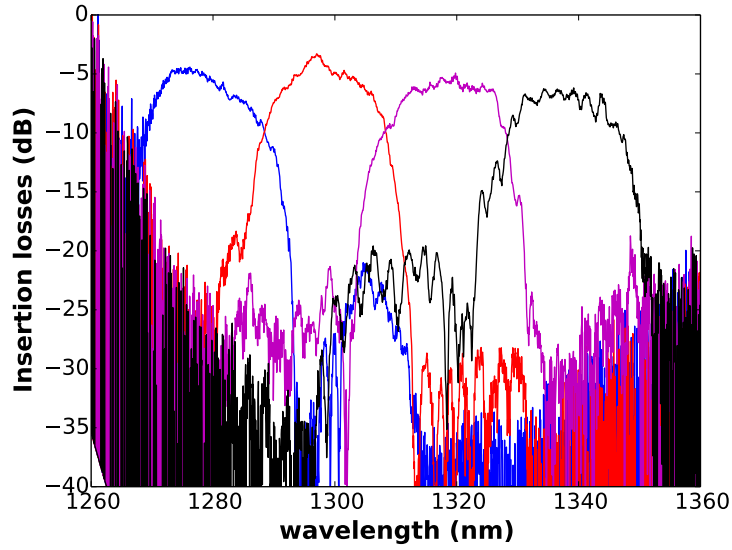


FIGURE 3.10: Measured spectrum after normalisation by FGC

$$f(x) = \begin{cases} M \text{ if } -w/2 \leq \lambda - \lambda_0 \leq w/2 \\ s.(\lambda - \lambda_0 + w/2) + M \text{ if } \lambda - \lambda_0 > w/2 \\ -s.(\lambda - \lambda_0 - w/2) + M \text{ if } \lambda - \lambda_0 < -w/2 \end{cases} \quad (3.8)$$

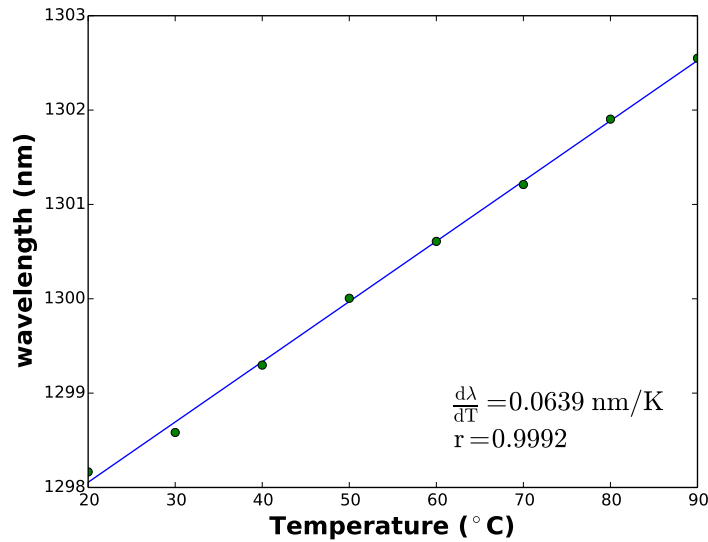


FIGURE 3.11: Thermal shift of channel 2. Dots = experimental data; line = linear fit

With every fit, we extract λ_0 , which represents the center of the door function and then

plot it with a linear regression (see figure 3.11). The temperature shift of our device can then be calculated to be 0.064nm/K, which is in the range of values for Silicon components [30]. The thermal shift results from the refractive index change of silicon and silica materials with temperature. This change is reported on the effective index of the FPR modes, which will in turn affect the interference conditions. A way to further limit the temperature shift would be to use a cladding with negative thermo-optic coefficient such as titanium dioxide [31] in order to counter-balance the thermal shift of the silicon guiding layer.

3.3 Arrayed Waveguide Gratings

Arrayed waveguide gratings (AWG) present a different approach to the wavelength multiplexer problem. They use a free propagation region, just as echelle gratings, but instead of having a grating mirror to ensure the optical path differences, they use instead an array of guides which are used as delay lines. This layout is usually preferred for DWDM applications with narrow channel-spacing. Many demonstrations of these components have been performed earlier on various platforms [1, 9, 13] but also on the thin SOI platform [11].

3.3.1 Theory

Although research on AWG still produces many papers, especially on the thin SOI platform, the theory and first results on AWG are well established and date from the early 90's [32, 33]. The basic rules for designing an AWG remain the same. This section will elaborate on AWG theory.

An AWG usually has 2 identical FPR, linked by an array of waveguides. Inputs are set on one side of the first FPR and outputs on the second. The FPR follows a confocal geometry with a radius R . Input and output waveguides are separated by a distance D_{IO} , while waveguides on the array side are separated by a distance D_{arr} . The effective index inside the FPR is noted n_S , the effective index in the array guides n_{arr} and the group index in the array guides $n_{g,arr}$. Each guide in the array has a length of $L_i = L_0 + i \cdot \Delta L$ with L_0 a constant. Most notations are described in figure 3.12.

The diffraction order of an AWG will follow this relation [34] :

$$m = \Delta L \cdot n_{arr} / \lambda_0 \quad (3.9)$$

The radius of the free propagation region is then expressed by the relation [35]

$$R = \frac{n_s \cdot D_{IO} \cdot D_{arr} \cdot \nu_0}{n_{g,arr} \cdot Sp \cdot \Delta L} \quad (3.10)$$

and the FSR [20] :

$$FSR = \frac{\lambda_0 \cdot n_{arr}}{m \cdot n_{g,arr}} \quad (3.11)$$

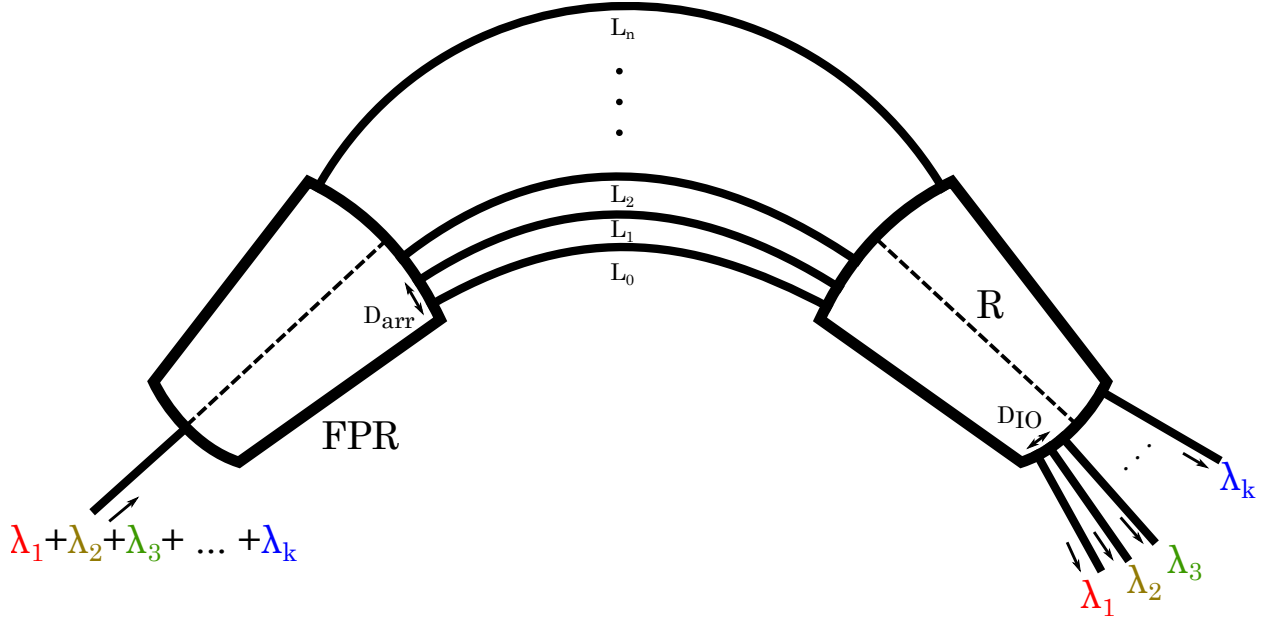


FIGURE 3.12: Schematic layout of an AWG

with $\lambda_0 = c/\nu_0$ the center wavelength. Sp represents the channel spacing, expressed in Hertz. The FSR is an important data while designing an AWG. It must be greater than the number of channels multiplied by the channel spacing so as to avoid overlapping channels.

When the light arrives in front of the FPR, it is transferred from a guided region to a semi-guided region with free propagation in the horizontal plane. Such a configuration is usually treated through a diffraction calculation. The resultant electric field in front of the array being the sum of all elementary sources from the input guide, as described by the Huygens principle. As a result, the field on one side of the FPR is the Fourier transform of the field on the other side. The field out of a waveguide is usually Gaussian. Therefore the field in front of the array will usually have a Gaussian shape. In order to get a sufficient amount of power through the waveguides, the number of waveguides in the array should cover a sizeable part of the diffracted field. An approximation of the number of required waveguides is the size of the field profile in front of the array divided by the the guide spacing. The shape of the field is directly proportional to R/w , with w the input profile's width. An approximation for the minimum number of guides N_{min} is [36] :

$$N_{min} = \frac{2.R.\lambda}{\pi.w.n_S.D_{arr}} \quad (3.12)$$

3.3.2 Modelling

In this section, the important points of an AWG simulation software developed during the thesis are detailed. The simulation runs in 4 parts. First we must determine the profile, effective and group index of all involved waveguides in the simulation. With this, one can

set the geometry of the AWG. The second step is to calculate the propagation in the first FPR and make the overlap with each array guide. The third step is to propagate each signal inside the array, leading to the fourth step where propagation is made through the 2nd FPR and final overlap with the output guides.

Mode profiles, index and overlap

In order to get an accurate simulation, the Gaussian profile of the waveguide modes assumed earlier must be refined. The actual profile can be calculated with the help of Fimmwave as described in section 2.1. One problem is that the field and indexes have to be calculated for every single wavelength, and an accurate spectrum requires at least a few hundreds points. In order to reduce calculation time while keeping an accurate estimation, only a few wavelength are calculated (typically 3-5 wavelengths) and a linear interpolation is used for the others.

The profiles calculated are discrete and propagate in the Z-direction, all the integrals expressed later were therefore discretised in the simulation software. The modes for all calculations are also normalised, which means that :

$$\iint_S \vec{E}(x, y) \wedge \vec{H}(x, y).d\vec{S} = 1 \quad (3.13)$$

With $\vec{E}(x, y)$ and $\vec{H}(x, y)$ respectively the electrical and magnetic field at coordinate (x, y) . The x and y-axis are defined locally as displayed in figure 3.13

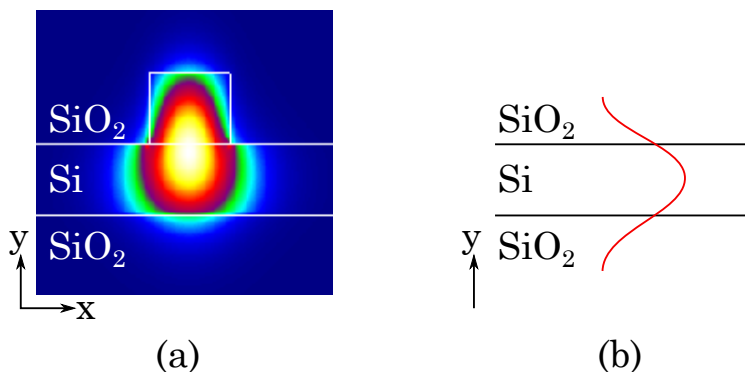


FIGURE 3.13: (a) Electrical field profile of a TE mode in an input/output waveguide (b) Magnetic field profile in the slab region

As the profiles are TE or TM, an approximation is made to simplify the calculation : the profiles are considered with a field in only one direction. For instance, only the E_x and H_y fields are taken into account during the calculation. For a TE mode, $\vec{E}(x, y) \simeq E(x, y)\vec{u}_x$ and for a TM mode, $\vec{H}(x, y) \simeq H(x, y)\vec{u}_x$

The mode profiles are necessary in order to make an overlap to the slab waveguide in the FPR. As the slab profile is a 1D profile, the overlap is made with each point column of the waveguide :

$$Ov(x) = \int E_{wg}(x, y) \cdot H^*(y) dy \quad (3.14)$$

With this method, the profile provided at the entry of the FPR can be tailored at will. The AWG simulator can for instance take into account tapered waveguides, including the interaction with neighbouring waveguides. It can also place multimode interferometer (MMI) at the input and output in order to flatten the spectral response, just as explained in section 3.2.2. This method also makes it independent on the software used to generate the mode profile.

First Free Propagation Region

The input waveguide arrives on the FPR as represented in figure 3.14. An overlap is necessary to couple the light from the waveguide to the FPR. From that point, the principle of Huygens can be applied on every point of the overlapped field.

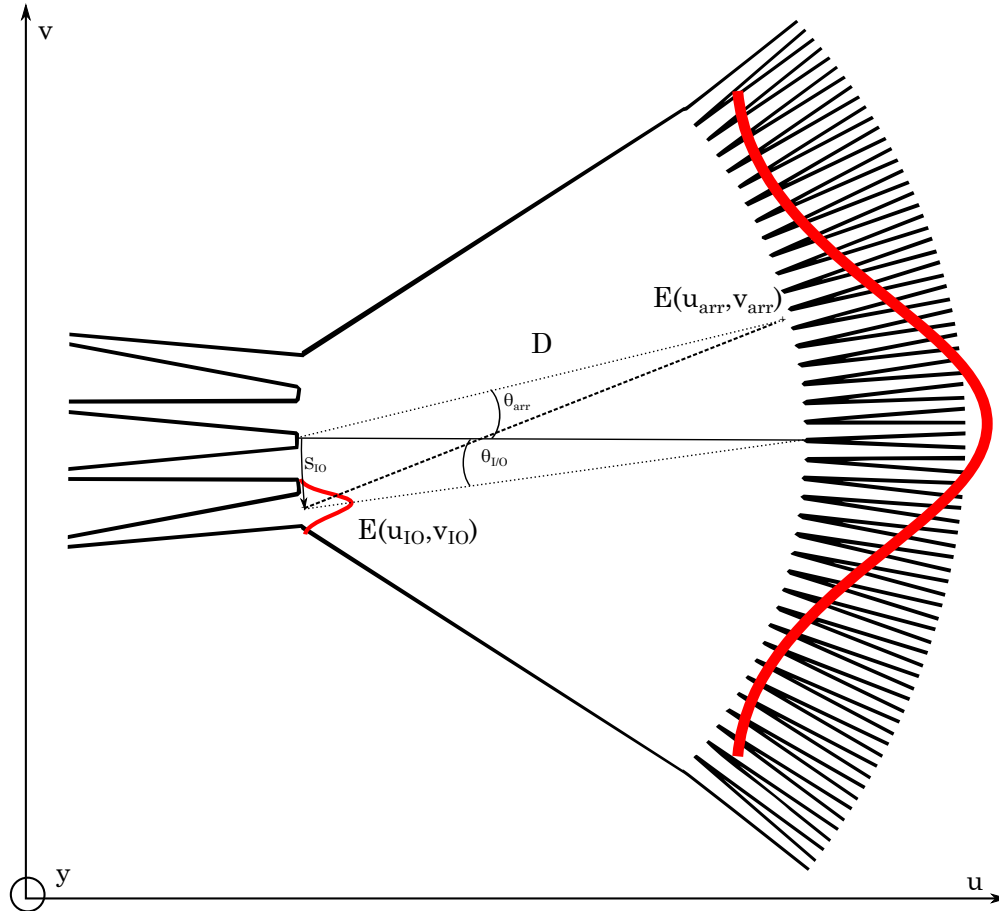


FIGURE 3.14: Application of the Huygens principle to the free propagation region

In the specific case of a 3D propagation, the formula for this principle would be :

$$E(x', y', z') = \iint_S K_{3D} \cdot E(x, y, z) \cdot \frac{\exp(i \cdot \frac{2\pi \cdot n_S}{\lambda} \cdot D)}{D} \cdot dS \quad (3.15)$$

with D the distance between point (x, y, z) and point (x', y', z') . The constant K_{3D} is there to keep the total energy throughout the diffraction process. In the 3D propagation case, the constant $K_{3D} = \frac{1}{i \cdot \lambda}$. The notations used for the 3D case are displayed in figure 3.15

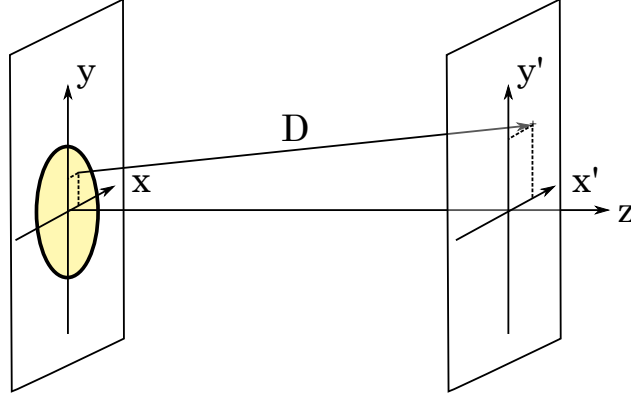


FIGURE 3.15: Notations for the 3D diffraction case

In the case of the studied FPR, the light is confined in the vertical direction and free in the horizontal plane. The diffracted profile is taken along the input/output array. The natural coordinate system for that geometry is to take a curve absciss $s_{IO} = R \cdot \theta_{IO}$, with the following coordinate transformation :

$$\begin{cases} u_{IO} = u_O - R \cdot \cos(s_{IO}/R) \\ v_{IO} = v_O + R \cdot \sin(s_{IO}/R) \end{cases} \quad (3.16)$$

The notations are displayed in figure 3.15. With the propagation in the horizontal plane, equation 3.15, can be re-written as :

$$E(u, v, y) = \int K_{2D} \cdot E_{IO}(s_{IO}, y) \cdot \frac{\exp(i \cdot \frac{2\pi \cdot n_S}{\lambda} \cdot D)}{D} \cdot ds_{IO} \quad (3.17)$$

$$D = \sqrt{(u - u_{IO})^2 + (v - v_{IO})^2} \quad (3.18)$$

D is the distance between the point (u_{IO}, v_{IO}, y) and (u, v, y) . The calculation in the program is made specifically for the set of points just before the waveguide array, with coordinates (u_{arr}, v_{arr}, y) . An overlap is then made with each of the array waveguides in order to get the transmitted power

As for the 3D case, the K_{2D} factor is there to ensure the conservation of the total energy as the wave diffracts. In the 3D case, that constant can be deduced by analysing a plane wave : after a certain propagation distance, the diffracted plane wave must be unchanged, thus giving a mean to determine the value of K_{2D} [37]

A similar calculation can be made in the 2D case, with notations described in figure 3.16 :

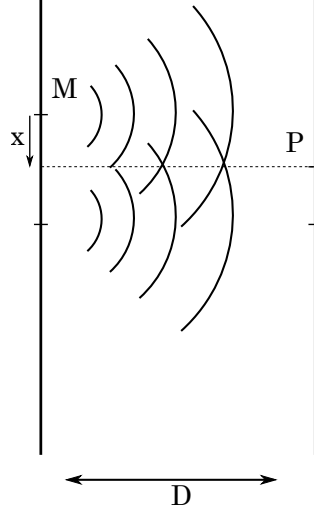


FIGURE 3.16: Schematic of a plane wave diffraction

The input field is a semi-guided plane wave. As such, the electric field distribution must remain unchanged after a propagation across a distance D in the horizontal plane :

$$E(D) = E_0 \cdot e^{i.k.D} \quad (3.19)$$

The propagation of the input wavefront can be made with a diffraction calculation :

$$E(D) = E_0 \cdot \int_{-\infty}^{\infty} K_{2D} \cdot \frac{e^{i.k.MP}}{MP} \cdot dx \quad (3.20)$$

The result obtained by this method must be a plane wave after propagation :

$$\Rightarrow e^{i.k.D} = \int_{-\infty}^{\infty} K_{2D} \cdot \frac{e^{i.k.MP}}{MP} \cdot dx \quad (3.21)$$

with

$$MP = \sqrt{x^2 + D^2} \simeq D \left(1 + \frac{x^2}{2.D}\right) \quad (3.22)$$

and

$$k = \frac{2.\pi.n_S}{\lambda} \quad (3.23)$$

$$\Rightarrow \int_{-\infty}^{\infty} K_{2D} \cdot \frac{e^{i.k.\frac{x^2}{2.D}}}{D} \cdot dx = 1 \quad (3.24)$$

$$K_{2D} = \sqrt{\frac{2.D}{\lambda}} \frac{(1-i)}{2} \quad (3.25)$$

Waveguide Array

Now that the power in each guide of the array is calculated, the next step is to compute the propagation across said waveguide. At the end of the propagation, in front of the second FPR, the field takes the following form, with k denoting the number of the waveguide and α the linear losses :

$$E_{end}[k] = E_{init}[k]. \exp(i. \frac{2.\pi.n_{arr}}{\lambda} . \Delta L.k - \alpha.\Delta L.k). \exp(i.\phi - \beta) \quad (3.26)$$

The constant $\exp(i.\phi - \beta)$ is there to take into account the phase shift and losses that are identical for all waveguides, such as the various tapers.

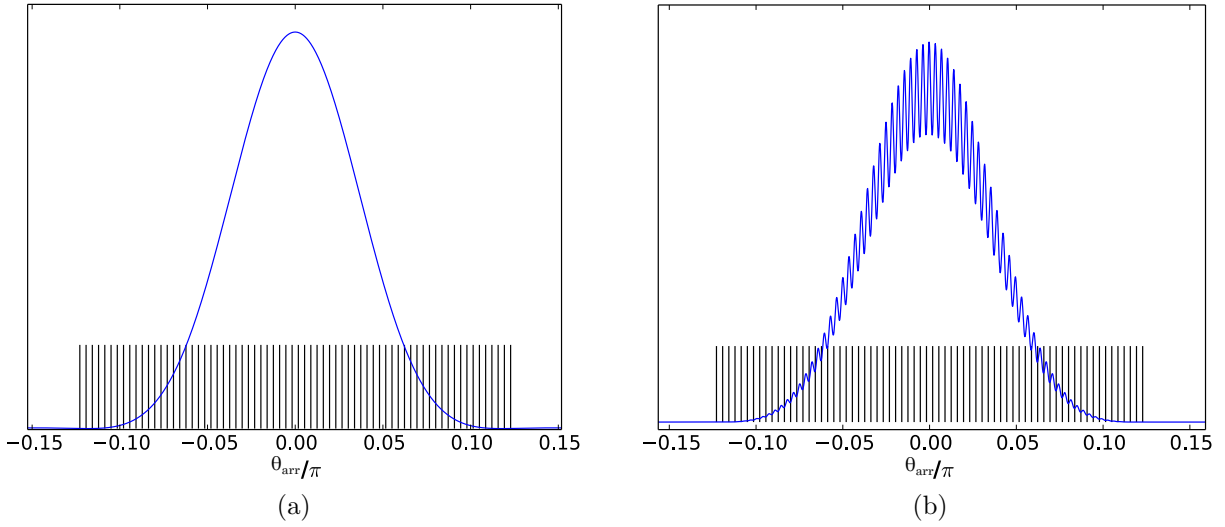


FIGURE 3.17: (a) Intensity profile just before overlap with waveguide array in function of θ_{arr}/π ; (b) Field profile just after waveguide array in function of θ_{arr}/π . The black vertical lines denotes the positions of the waveguides. Angles follow the definition from 3.14

As the waveguides have a fixed profile which is not perfectly flat, the field profile that is injected to the second FPR is not exactly the same as the one at the end of the first FPR. As we can see in figure 3.17, the profile after the array has a modulation of its amplitude in conjunction with the presence of the emitting guides.

Second Free Propagation Region

As for the first FPR, a calculation is realised for the second FPR, very similar to the first one, with the difference that the light is emitted by each guide on the array side. The resulting field on the output side can be described as follows :

$$E(u, v) = \sum_{k=1}^N \int K_{2D}.E_{arr}[k](s_{arr}, y). \exp(i. \frac{2.\pi.n_S}{\lambda} . D). ds_{arr} \quad (3.27)$$

with $s_{arr} = R.\theta_{arr}$

After the overlap with the guide is made, the calculation for that specific wavelength is finished and we get one point of the spectrum.

Effect of tapering waveguides

The simulation software proposes 2 possibilities for getting waveguide profiles and make the overlap. First possibility is to take the waveguide at its end, just before the FPR and then calculate the profile at this position. That solution is simple to implement and quick to calculate. It is a good choice for a fast choice of the main variables but is not so accurate for the spectrum prediction.

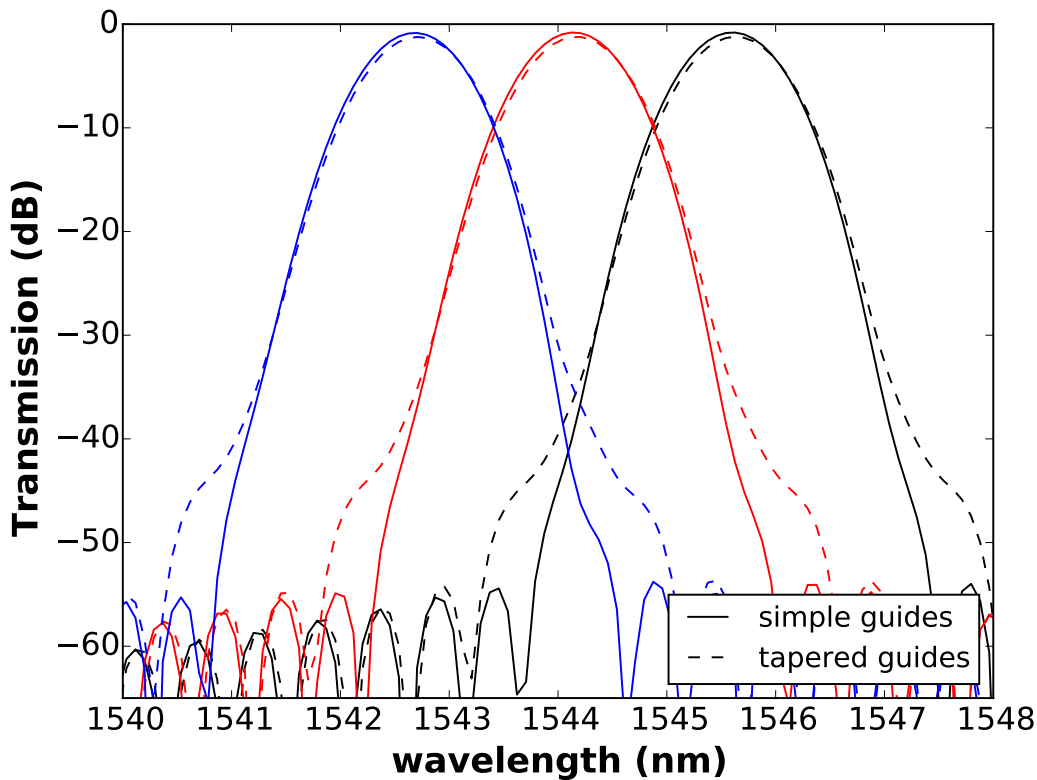


FIGURE 3.18: Simulation spectra of 3 adjacent channels of a 16X200GHz AWG with simple waveguide simulation of tapered waveguide simulation

The second possibility offered by the program is to make tapered waveguides : the light is injected at one side of the waveguide and the resulting profile at the other side is calculated. When coupling light from the incoming FPR to the waveguide, an overlap is made with every fundamental mode of the simulated waveguide structure and a propagation is made to the port of interest. With this method, the exchange of light between neighbouring waveguides can be taken into account and simulations with MMI at input and outputs can be performed.

The overall process is very similar to the one proposed in the EPPIPROP software presented in section 3.2. This method is more accurate than the previous one but is harder to implement. It also take much longer time to run through the calculation as the software needs to calculate a full propagation instead of just a fundamental mode profile. As of today, the simulation software relies on Fimmprop [25] to calculate the waveguides profiles and propagation, but the whole process is automated with minimum user inputs.

The difference between the two calculations can be evaluated in figure 3.18 for the same AWG simulation. The channel response with the tapered waveguides and light coupling to the neighbours is wider than the other and even more so at the base of the peak. This widening of the peak, in this specific case, degrades the crosstalk by more than 5dB. An imperfect fabrication with higher coupling between the guides can further deteriorate the crosstalk.

Layout

Along with the simulation program, there came the necessity to create another program to export the layout in order to draw the simulated designs. This second software is linked to the simulation. It can create at the moment two kinds of layout as displayed in figure 3.19. They are both “Manhattan” configurations, which means that each path has 4 turns, and the major part of the guides are horizontal or vertical. The path difference ΔL is always created in these straight, horizontal or vertical sections. In that way, the width and uniformity of the waveguides are better controlled, which is critical for the good operation of the AWG. The main difference between the two relies in the FPR : one is tilted, the other is not. Both configurations show advantages and drawbacks, as decribed in table 3.4 and both have given good results in the past.

	advantages	drawbacks
manhattan straight	<ul style="list-style-type: none"> - short path and small angle adjustment turns - simple to implement - smaller footprint 	The increment in adjustment turn is linear from the center. A bad control of linewidth can create a phase jump between left and right part of the array.
manhattan tilted	<ul style="list-style-type: none"> - Constant increment in adjustment turn form the first guide \rightarrow no phase jump 	<ul style="list-style-type: none"> -large adjustment turns which can, if not well controlled, change the final channel spacing - harder to implement

TABLE 3.4: Comparaison of tilted versus straight Manhattan configuration

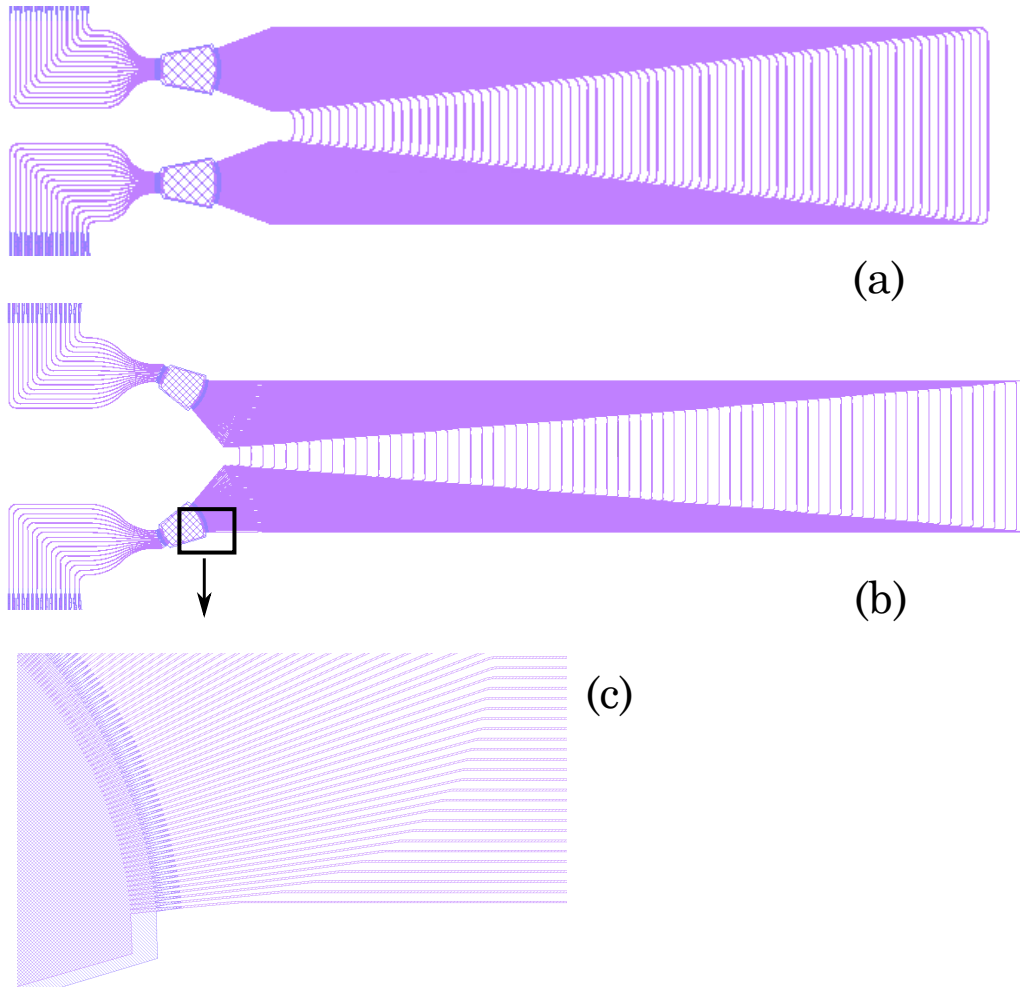


FIGURE 3.19: Layout of a 16X100GHZ AWG with Manhattan (a) Straight (b) tilted Layout. (c) is a zoom on FPR from (b)

3.3.3 Simulation & measure

With the help of the simulation program , a few types of AWG were designed. Unfortunately, the measurement results are not yet available at the time of the writing because of the time required to create the software in conjunction with the time required to fabricate the samples. On the other hand, the previous PhD student had designed some components that can be retro-simulated.

AWG $16 \times 200\text{GHz}$

The studied AWG has a manhattan straight layout with 16 channels spaced 200GHz. The aim of this AWG was to be inserted inside a slot-blocker, as shown in [11]. The goal here is to prove the accuracy of the simulation software by simulating a design that has already been measured. The simulation spectra and the measurement results are showed side by side in figure 3.20

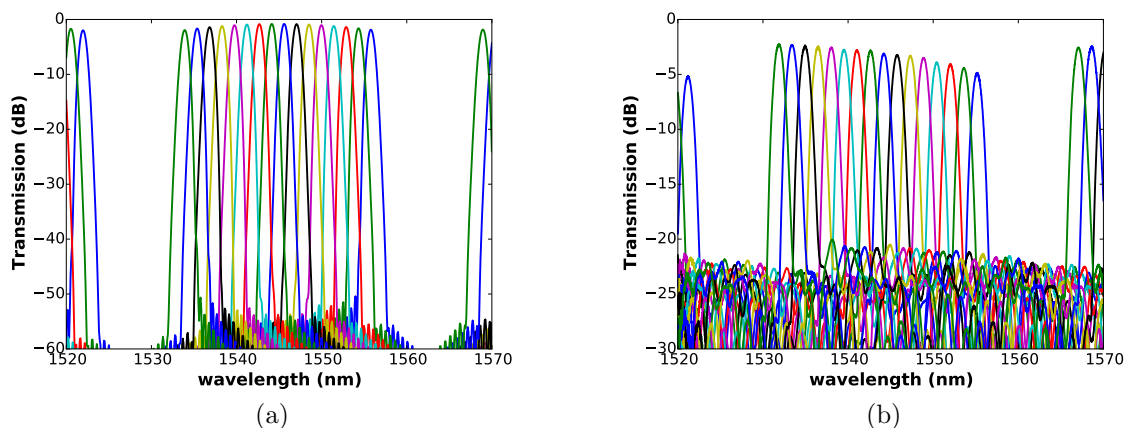


FIGURE 3.20: (a) Simulation spectrum (b) Measured spectrum of a $16 \times 200\text{GHz}$ AWG with straight Manhattan layout.

The position of the simulated and measured peaks are very close, which means that the simulation is accurate on that point and the width of array waveguides are well controlled. This simulation did not take into account waveguide losses which can alter the losses and uniformity. In particular, the losses in the waveguides that permit light injection and collection were not taken into account. As a result, the measured insertion losses are higher and the channel uniformity is different than on the simulation : the measured channel on the left of the spectrum have shorter extraction waveguides and thus lower losses than the channels on the right. But the main difference resides in the crosstalk : the noise background is much higher (-25dB vs -60dB) in the measured spectrum. This is a well known effect that can be explained by phase errors : small variations of guide width creates distortions in the phase profile at the end of the array, which in turn increases crosstalk. This phase error effect is not

yet taken into account in the simulation. Further improvement on that point are required. The last difference is in the peak width : the measured peak is wider with a 3dB bandwidth of 0.86nm for the simulated spectrum compared to 1.21nm for the measured spectrum. A small difference in RIB layer thickness or in guide shape can explain this difference. In conclusion, the simulation program is accurate to determine the spectrum position and spacing. But, as for most AWG simulation programs on this platform, it needs further improvement in the prediction of crosstalk and insertion losses.

AWG $4 \times 800\text{GHz}$

The goal of this AWG was to provide a multiplexer for an array of 4 distributed feedback lasers. This AWG was designed with a flat top in order to be more tolerant to wavelength shifts. With that purpose in mind, the same method as in section 3.2.2 was used. The component was designed to have the final spectrum as flat as possible with reasonable crosstalk and insertion losses. The simulation gives insertion losses always better than 5dB with a 3dB bandwidth around 4 nm. The simulated crosstalk is always better than 20dB on the whole bandwidth.

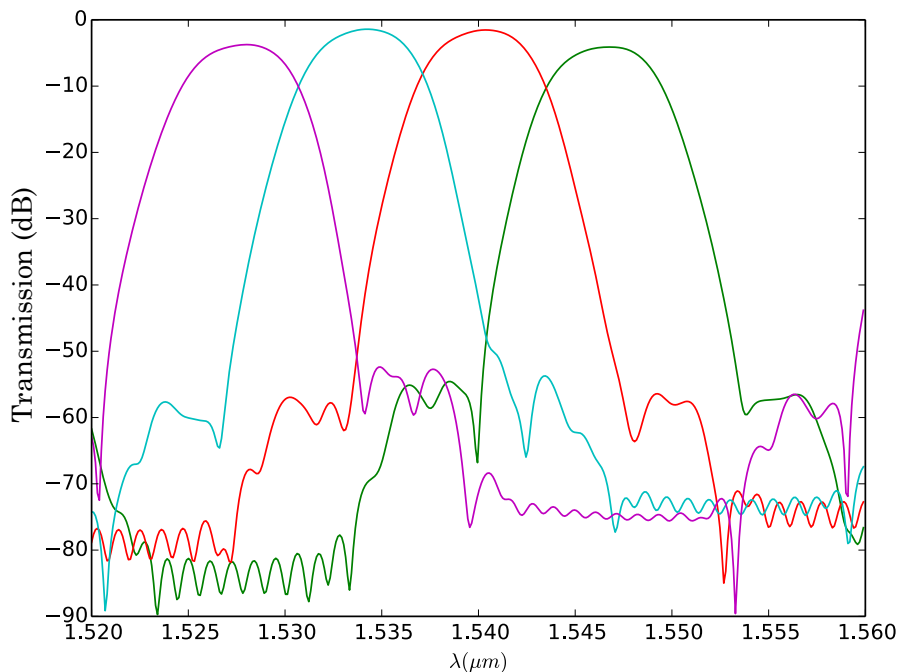


FIGURE 3.21: Simulated spectra of a flattened-top $4 \times 800\text{GHz}$ AWG

The profiles just after the input MMI and just before the array are presented in figure 3.22. One can see that the second image is, as should be, the Fourier transform of the input profile. As the input profile is close to a door function, the profile before the array is close to

a sinus cardinal, with 2 side lobes. These lobes are very important and must be transmitted through the array.

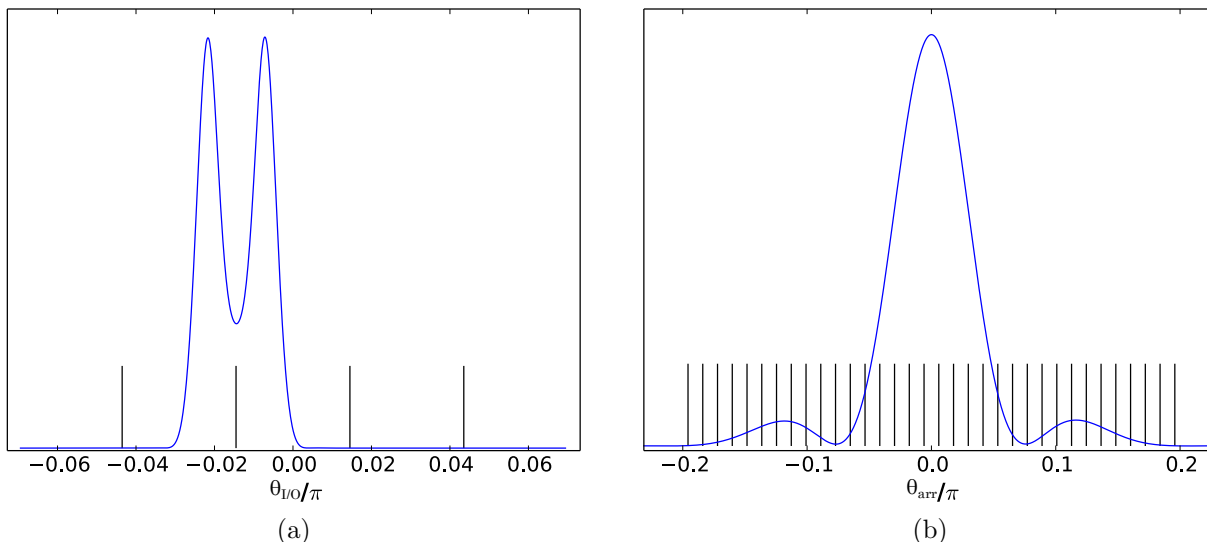


FIGURE 3.22: (a) Intensity profile just after the input MMI in function of $\theta_{I/O}/\pi$. (b) Intensity profile just before the array in function of θ_{arr}/π . Black vertical lines denotes the position of the input and array waveguides.

3.4 Conclusion

In this chapter was demonstrated the potential of the thin SOI platform for WDM applications, either dense WDM or coarse WDM. 3 different kinds of designs were detailed : ring resonators, Echelle grating and Arrayed waveguide gratings. Each of them provided interesting results with advantages and drawbacks. The ring resonators have an outstanding footprint and insertion losses but require active tuning of each ring to get a precise channel spacing. EGs are very robust to fabrication variations and are good for both CWDM and DWDM applications, but they require a good wafer thickness uniformity to begin with. AWG can provide performance similar or better than EG, but their performances are much more sensitive to fabrication uncertainties.

The EGs presented in this chapter were at the state of the art on the thin silicon platform. The first presented device is a 16×100 GHz EG with insertion losses lower than 2dB and a crosstalk around 15dB. The second is a CWDM EG with 4 channels spaced 20nm which exhibited a flat top behaviour.

An AWG simulation tool was also developed during the thesis and is able to reproduce the measurement results of previously designed components.

References

- [1] Y. HIDA et al. “Fabrication of low-loss and polarisation-insensitive 256 channel arrayed-waveguide grating with 25 GHz spacing using 1.5% Delta; waveguides”. In : *Electronics Letters* 36.9 (avr. 2000), p. 820–821.
- [2] S. JANZ et al. “Planar waveguide echelle gratings in silica-on-silicon”. In : *IEEE Photonics Technology Letters* 16.2 (fév. 2004), p. 503–505.
- [3] C. SCIANCALEPORE et al. “Low-crosstalk fabrication-insensitive echelle grating multiplexers and passives for the silicon photonics toolbox”. In : *SPIE OPTO*. International Society for Optics et Photonics. 2015, p. 936508–936508.
- [4] *16 Channels 100GHz DWDM MUX Plug-in Module*. Finisar. Mar. 2015.
- [5] *SO-DWDM-MUX-40CH*. Solid Optics.
- [6] *Coarse Wavelength Division Multiplexer/Demultiplexer (CWDM) Filter*. JDSU.
- [7] C. SCIANCALEPORE et al. “Low-Crosstalk Fabrication-Insensitive Echelle Grating Demultiplexers on Silicon-on-Insulator”. In : *IEEE Photonics Technology Letters* 27.5 (mar. 2015), p. 494–497.
- [8] O. K. KWON et al. “InP-based polarization-insensitive planar waveguide concave grating demultiplexer with flattened spectral response”. In : *ETRI journal* 31.2 (2009), p. 228–230.
- [9] Y. H. LIN et S. L. TSAO. “Improved design of a 64 x 64 arrayed waveguide grating based on silicon-on-insulator substrate”. In : *IEE Proceedings - Optoelectronics* 153.2 (avr. 2006), p. 57–62.
- [10] S. T. S. CHEUNG et al. “Low-loss and high contrast silicon-on-insulator (SOI) arrayed waveguide grating”. In : *2012 Conference on Lasers and Electro-Optics (CLEO)*. Mai 2012, p. 1–2.
- [11] G. de VALICOURT et al. “Monolithic Integrated Slot-Blocker for High Datarate Coherent Optical Slot Switched Networks”. In : *Journal of Lightwave Technology* 34.8 (avr. 2016), p. 1807–1814.
- [12] H. ISHII et al. “Zero insertion loss operations in monolithically integrated WDM channel selectors”. In : *IEEE Photonics Technology Letters* 11.2 (fév. 1999), p. 242–244.
- [13] M. KOHTOKU et al. “InP-based 64-channel arrayed waveguide grating with 50 GHz channel spacing and up to -20 dB crosstalk”. In : *Electronics Letters* 33.21 (oct. 1997), p. 1786–1787.
- [14] S. PAPAIOANNOU et al. “On-Chip Dual-Stream DWDM Eight-Channel-Capable SOI-Based MUX s/DEMUX s With 40-GH z Channel Bandwidth”. In : *IEEE Photonics Journal* 7.1 (fév. 2015), p. 1–10.
- [15] D. FENG et al. “Fabrication Insensitive Echelle Grating in Silicon-on-Insulator Platform”. In : *IEEE Photonics Technology Letters* 23.5 (mar. 2011), p. 284–286.

- [16] J. BROUCKAERT et al. “Planar Concave Grating Demultiplexer With High Reflective Bragg Reflector Facets”. In : *IEEE Photonics Technology Letters* 20.4 (fév. 2008), p. 309–311.
- [17] J. JIANG et al. “Arrayed waveguide gratings based on perfluorocyclobutane polymers for CWDM applications”. In : *IEEE Photonics Technology Letters* 18.2 (jan. 2006), p. 370–372.
- [18] Y. HU et al. “Coarse wavelength division (de) multiplexer using an interleaved angled multimode interferometer structure”. In : *Applied Physics Letters* 102.25 (2013), p. 251116.
- [19] W. SHI et al. “Ultra-compact, flat-top demultiplexer using anti-reflection contra-directional couplers for CWDM networks on silicon”. In : *Optics express* 21.6 (2013), p. 6733–6738.
- [20] L. VIVIEN et L. PAVESI. *Handbook of silicon photonics*. Taylor & Francis, 2016.
- [21] F. XU et A. W. POON. “Silicon cross-connect filters using microring resonator coupled multimode-interference-based waveguide crossings”. In : *Optics express* 16.12 (2008), p. 8649–8657.
- [22] D. BACHMAN et al. “Post-fabrication Trimming of Silicon Photonics Circuits by fs Laser Pulses”. In : *Optical Fiber Communication Conference*. Optical Society of America. 2016, Tu3E–1.
- [23] S. PARK et al. “Si micro-ring MUX/DeMUX WDM filters”. In : *Optics express* 19.14 (2011), p. 13531–13539.
- [24] *Photon Design Eppiprop version 6.3.1*.
- [25] *Photon Design Fimmwave/Fimmprop version 2.0*.
- [26] R. J. LYCETT, D. F. G. GALLAGHER et V. J. BRULIS. “Perfect Chirped Echelle Grating Wavelength Multiplexer: Design and Optimization”. In : *IEEE Photonics Journal* 5.2 (avr. 2013), p. 2400123–2400123.
- [27] P. CHEBEN. *Wavelength dispersive planar waveguide devices: echelle and arrayed waveguide gratings*. T. 5. chapter, 2007.
- [28] W. BOGAERTS, A. RUOCCO et S. DWIVEDI. “Silicon photonics non-resonant wavelength filters: comparison between AWGs, echelle gratings, and cascaded Mach-Zehnder filters”. In : *SPIE* 9365 (2015), 93650H.
- [29] K. OKAMOTO et A. SUGITA. “Flat spectral response arrayed-waveguide grating multiplexer with parabolic waveguide horns”. In : *Electronics letters* 32.18 (1996), p. 1661.
- [30] L. PAVESI, D. J. LOCKWOOD et al. *Silicon Photonics III*. Springer, 2016.
- [31] P. ALIPOUR et al. “Titania-clad microresonators on SOI with athermal performance”. In : *Conference on Lasers and Electro-Optics*. Optical Society of America. 2010, JThE44.
- [32] C. DRAGONE. “An N*N optical multiplexer using a planar arrangement of two star couplers”. In : *IEEE Photonics Technology Letters* 3.9 (sept. 1991), p. 812–815.

- [33] C. DRAGONE, C. EDWARDS et R. KISTLER. “Integrated optics N* N multiplexer on silicon”. In : *IEEE Photonics Technology Letters* 3.10 (1991), p. 896–899.
- [34] K. OKAMOTO. *Fundamentals of optical waveguides*. Academic press, 2010.
- [35] C. R. DOERR et K. OKAMOTO. “Planar lightwave circuits in fiber-optic communications”. In : *Optical Fiber Telecommunications VA: Components and Subsystems* (2008), p. 269–342.
- [36] A. LELIEPVRE. “Silicon Photonics Hybrid Lasers”. Thèse de doct. École Polytechnique, 2013.
- [37] H. BENISTY. *Cours d’Optique physique ESO1*. Course material at IOGS, 2016.

Chapter 4

Active Components & Integration

ACTIVE components play a key role in every telecommunication system. These devices are the ones used to create, modulate, amplify and detect light.

As discussed earlier (see section 1.2), the silicon platform doesn't have any easy access to a light amplification section, necessary condition for the construction of a light source. At that point, designers have four choices to get a light source on the silicon platform. The first one is to couple light from an external component with an optical fiber. The silicon then only assumes the function of modulation, detection and passive functions [1]. The second option is to use flip-chip : an active section, processed separately, is mounted on the silicon chip and the light is directly coupled to the silicon, without the need of an optical fiber [2–5]. The third option is to make a direct epitaxy of III-V material on silicon [6]. But due to the large lattice mismatch between the two materials, a large buffer is necessary to make the lattice adaptation. This buffer limits the possible mode transfer between the III-V region and the silicon. The fourth option uses the hybrid III-V on silicon platform [7–10] where the III-V material is bonded on the silicon wafer. In this case, the III-V stack can vertically couple light to and from the silicon structure (see section 4.1). This active section can lead to various functions, the most important are the semi-conductor optical amplifiers (SOA) (see section 4.2), lasers (see section 4.3) and electro-absorption modulators (see section 4.4). Silicon PN junctions can also be considered as an active component as they are a key component for high-speed modulation and will be studied in section 4.5.

With the active sections described above in conjunction with the passive devices described in earlier chapters, one can build a complex, integrated circuit with multiple functions assembled on the same chip. The rest of this chapter will be dedicated to these integrated circuits, starting with a tunable laser integrated with an EAM modulator and then I/Q modulators with the objective of creating an integrated transceiver for high data rate communication.

4.1 III-V gain section

4.1.1 Structure

The gain section in our structure is a hybrid structure made partially with a silicon waveguide and partially with a III-V stack that is very similar to the ones used on the InP platform. The III-V epitaxial structure is, from top to bottom :

- A P-doped layer, mainly used for electrical injection. This layer has large optical losses. The design of the structure should minimise the overlap of the optical mode with this layer. An electrode is deposited on top of that layer for electrical injection purpose.
- The quantum well structure with the necessary adaptation layers. This stack is responsible for the light amplification. The optical mode should have a high confinement in that stack to ensure a large gain.
- The N-doped layer. This layer is very thin and is used to collect the electrical current on side electrodes.

The quantum well section that is responsible for the gain is usually made with 6 wells with a photoluminescence set around 1520nm for sections in the C-band and 1270nm in the O-band. For more details on the fabrication process, see sections 1.7 and 1.9.

Figure 4.1 shows a schematic of the hybrid structure with the corresponding SEM image on the right. The InP mesa is located above the silicon waveguide. The two structures are separated by a very thin layer of silica. The metal electrodes are also represented and are used for the electrical injection of the component.

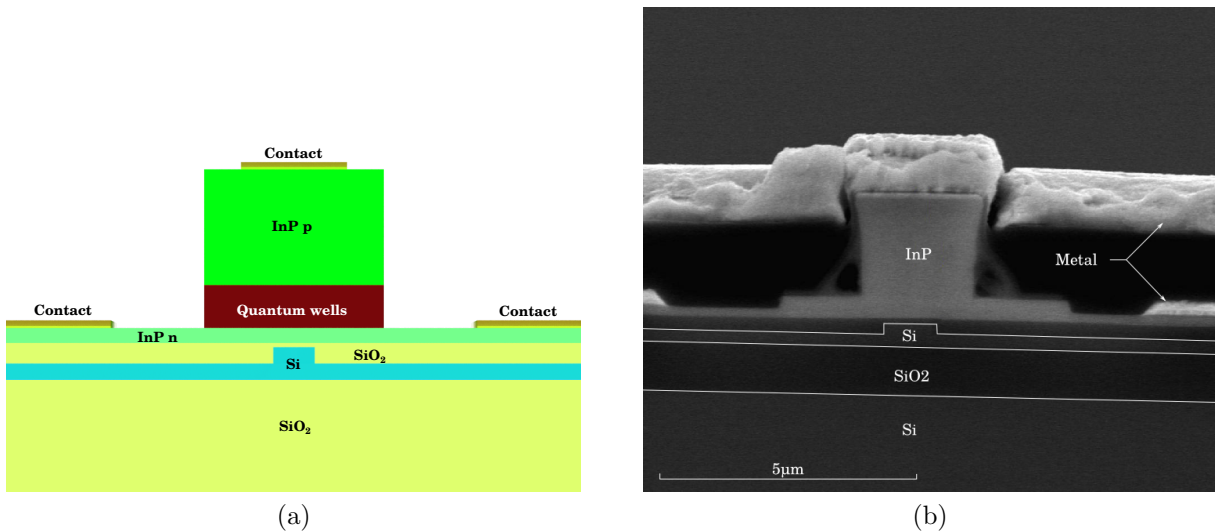


FIGURE 4.1: (a) Schematic of an hybrid III-V on silicon gain structure (b) SEM image of said structure

Because of the small distance between the two structures, an interaction occurs that is very similar to what happens in directional couplers : the natural modes of the structure are

hybrid mode, partly confined in silicon and partly confined in the InP structure. Because of this coupling, light can be coupled from the silicon waveguide to the InP structure and back again by simply changing the silicon guide’s width.

The hybrid mode is partly guided by the silicon and amplified by the quantum wells. This structure presents the advantage that one can tune the amount of field that is amplified by the InP region by changing the width of the silicon waveguide. Another advantage is that the silicon “draws” the mode to the bottom, thus reducing the amount of field in the P-doped InP region that absorbs light. The field profile of the hybrid mode is presented in figure 4.2.

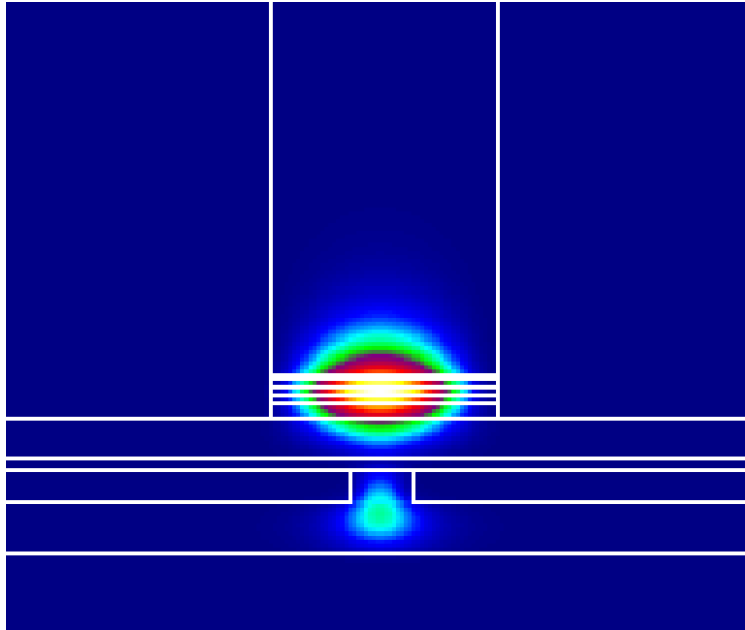
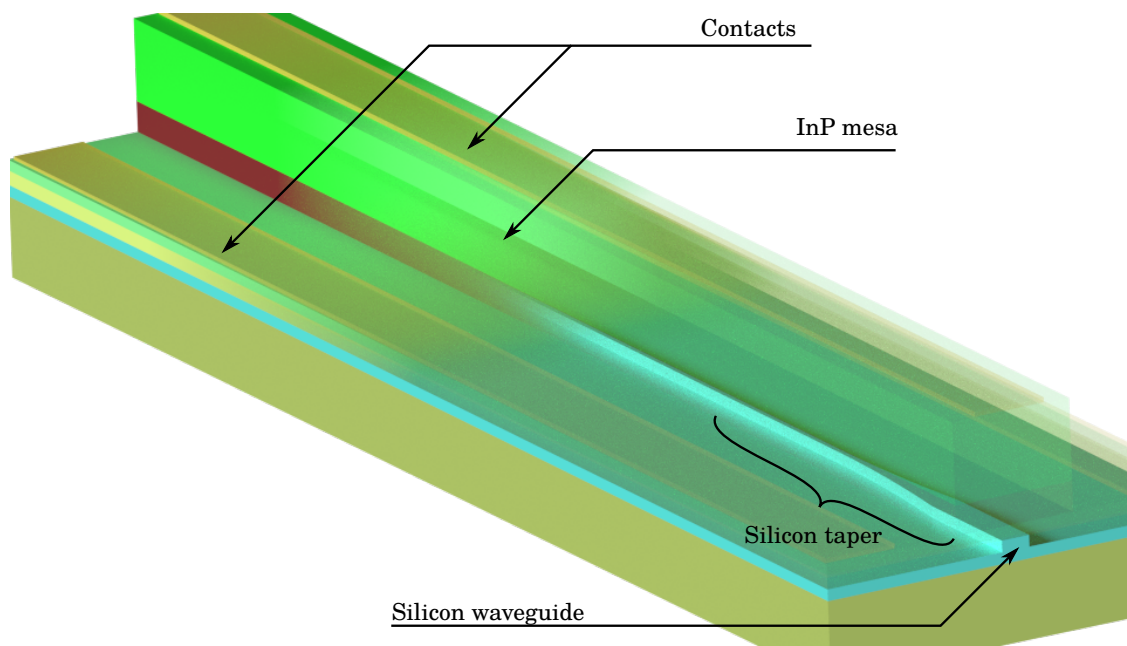


FIGURE 4.2: Field intensity of the hybrid InP-Silicon mode

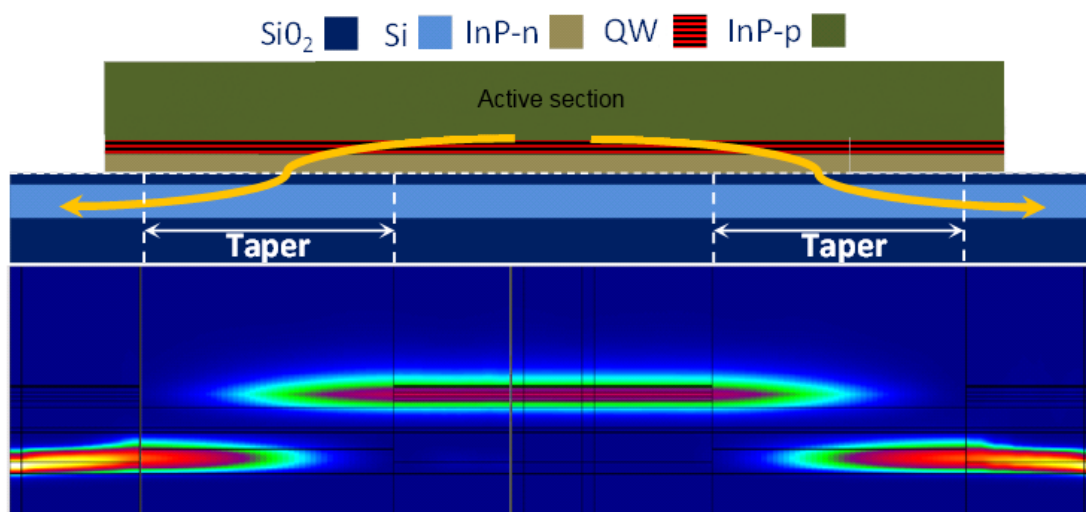
4.1.2 Transferring light from Silicon to InP

The main purpose of the gain section is either to amplify the optical mode or to suppress it in the specific case of electro-absorption modulators. All the filtering and circuitry are realised in the silicon part. A taper is made with the silicon guide in order to adapt the mode from the pure silicon mode (see figure 2.2c) to the hybrid InP-Si mode (see figure 4.2). In the taper, the width of the silicon guide is reduced until its index matches the index of the III-V region. At that tipping point, interaction between the two guides is maximum. Further narrowing of the silicon waveguide “pushes” the mode to the III-V waveguide. The theory behind that is similar to tapered directional couplers [11]. The taper is optimised to make the transfer with low reflections and the shortest length possible [7].

Figure 4.3(a) shows a schematic of the hybrid structure with the silicon taper waveguide beneath the InP mesa. Figure 4.3(b) is a side view of the same structure, with the corresponding simulation of field intensity throughout the structure. The mode is integrally transferred



(a)



(b)

FIGURE 4.3: (a) Schematic 3D view of a gain section (b) Schematic and simulation of the silicon taper

to the InP structure and then back to the silicon waveguide, thanks to the silicon taper. The efficiency of the power transfer for a quantum well structure is estimated at about 95%.

4.2 Semi-conductor Optical Amplifiers

Semi-conductor amplifiers (SOA) are gain sections with an input and an output. They are used to amplify a signal with minimum additional noise. SOAs made on the silicon platform are not the best match for a packaging as a single component because their characteristics are yet lower than their InP counterparts (typ. 27dB amplification on InP [12] versus 5-10dB on silicon [13]). But the fact that they can be integrated on the silicon platform with other functions makes them very attractive for more complex devices with large losses. An SOA can be added to boost the signal before the injection to the fiber.

Figure 4.4a shows the schematic of an SOA that has been designed, packaged and measured by our team. The sample consists of an SOA with FGC at both ends to inject and collect light. Current is injected by contact pads. The whole chip was inset in a modified butterfly package as presented in figure 4.4b. Light is injected and collected by optical fibers on the small sides of the module. Current is injected by the metal pins on the large sides of the module.

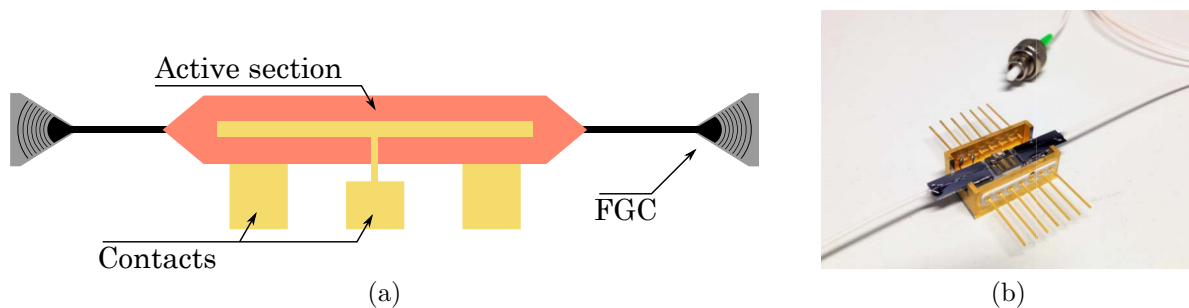


FIGURE 4.4: (a) Schematic of a gain section (b) Picture of the packaged SOA.

The SOA was thoroughly measured in order to extract the data of interest. Figure 4.5a shows the internal gain of the SOA as a function of injected current. The internal gain is, as expected, higher for large current values, but the spectrum at 90mA has more fluctuations. This effect is due to the reflections by the fiber grating coupler (FGC) : they create a Fabry-Perot cavity with very weak mirrors that are amplified by the gain section. Figure 4.5b shows the variation of the gain spectrum from fiber to fiber with respect to temperature. As the temperature increases, the gain section becomes inefficient and the gain drops. The maximum of amplification is also shifted from 1550nm at 10°C to more than 1560nm at 60°C. The fiber to fiber gain is much lower than the internal gain ($\sim 15dB$) because of the large losses induced by the FGC and the whole packaging.

For this device, the saturation power in the output silicon waveguide is around 9 dBm for an SOA current of 70 to 80 mA. The fiber-to-fiber gain in these conditions is around 5

to 6 dB. The external noise figure has a value around 17dB under working conditions. This high value of the noise figure comes from the input coupling losses estimated at 9dB.

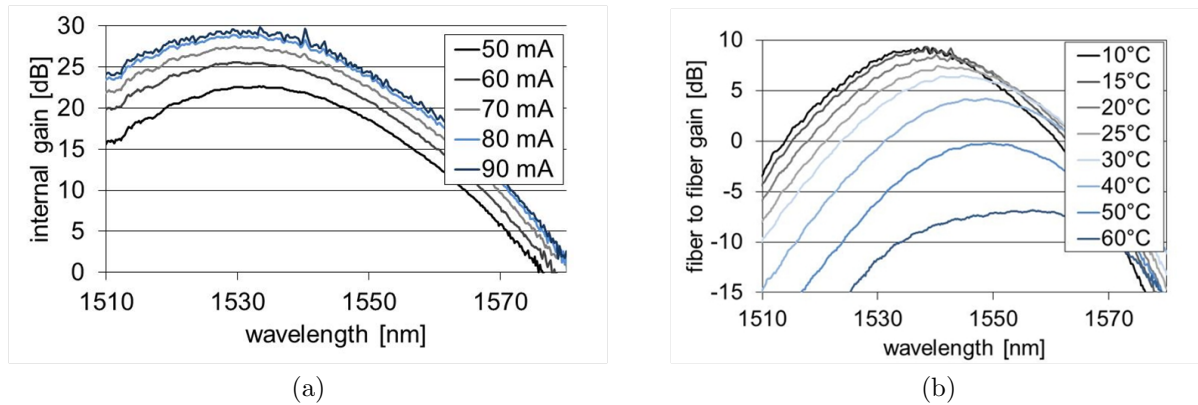


FIGURE 4.5: (a) Internal gain of SOA for various injected current (b) Thermal rolloff of fiber to fiber gain of the packaged SOA with injected current of 70mA

4.3 Tunable Lasers

The most important building block of any photonic platform is the light source, and more specifically the laser. The two main categories of semi-conductor lasers are the distributed feedback (DFB) laser [14] which uses a grating in the gain section to specifically enhance a wavelength and the tunable laser. Although DFB lasers with good performances have been demonstrated on the hybrid silicon platform [15], only the tunable laser will be studied in this thesis.

The tunable laser consists of a cavity closed by mirrors on both sides, a gain section to amplify the signal and a filtering system. In a traditional semi-conductor cavity, many modes can be amplified in what is called the Fabry-Perot cavity. The filtering system is there to ensure that only one of these modes is enhanced. The selected Fabry-Perot mode can be changed to another, making the laser tunable.

On the InP platform, the preferred filtering system uses Sample Grating Distributed Bragg Reflector (SG-DBR) [16] or Digital Supermode Distributed Bragg Reflector (DS-DBR) [17]. Both use Bragg gratings as mirrors and filtering system. The tunability is usually made by thermal heating of one or both mirrors.

Silicon photonic, on the other hand, will prefer ring resonators to Bragg reflector. Ring resonators are chosen mostly because of the fabrication process : a good quality ring is easier to make than a good quality Bragg grating. The ring geometry is also more versatile as the rings can be combined with other structures. Because of the platform's specificity that allows very sharp turns, rings with a very large free spectral range (FSR) can be obtained (see section 2.6). The position of the ring's peaks can also be thermally tuned to enhance only one of the cavity mode. The ring must have a FSR large enough to cover most of

the gain bandwidth. The single rings designed by our team have FSR around 30nm. With such a large FSR, the ring is only a few microns in perimeter. This kind of component has reasonable losses only thanks to the silicon properties that enables extremely sharp bends.

4.3.1 The Vernier effect

The single ring tunable laser has many qualities such as being easy to operate, but the tuning range is limited by the maximum temperature produced by the heater before breakdown. A solution consists in using the Vernier effect with a double ring. The aggregated FSR in a Vernier filter can be expressed as a function of the FSR of the two filters :

$$FSR = \frac{FSR_1 \cdot FSR_2}{FSR_1 - FSR_2} \quad (4.1)$$

with FSR_1 and FSR_2 the FSR for the first and second filter respectively. The aggregated FSR is much larger than the FSR of either rings. It enables to relax the constraints on ring design since they will each have a lower FSR than the single ring filter.

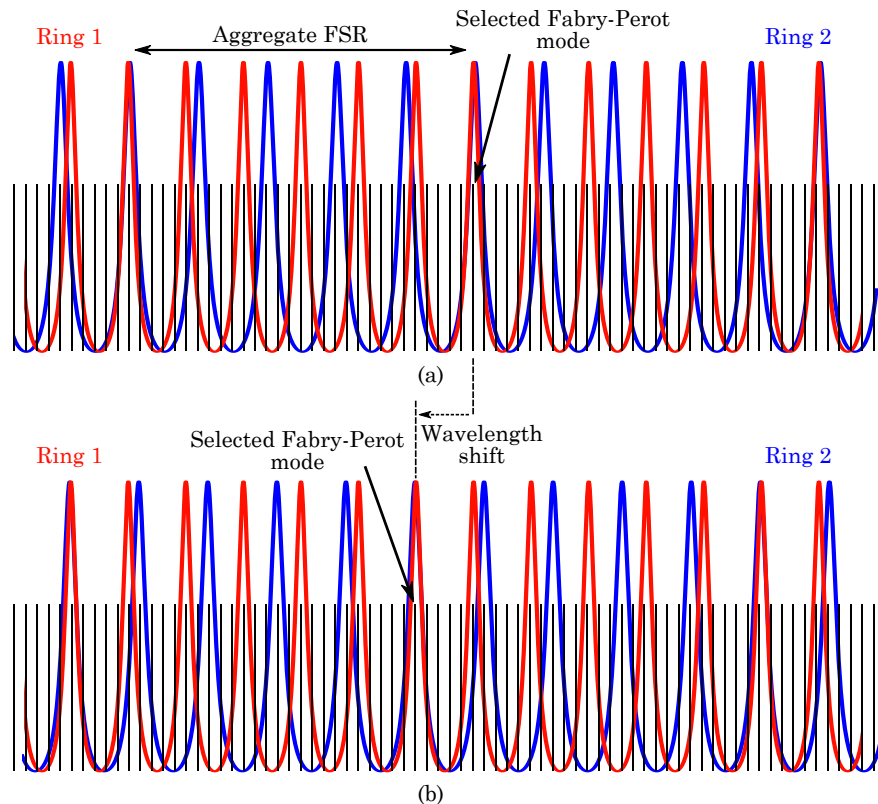


FIGURE 4.6: Schematic of the Vernier effect with tunability. (a) without heating (b) heating ring 2

The tunability is achieved by translating the spectrum of one ring with a heater. As shown in figure 4.6, a small modification in spectrum position of ring 2 creates a large change in

the selected wavelength. By tuning both rings, one can select any of the Fabry-Perot cavity modes in the aggregated FSR with reasonable heating power. The measured spectrum of a double ring is displayed in figure 4.7. With the ring's FSR of 400GHz and 430GHz, the aggregated FSR is 45nm. This double ring configuration was incorporated in a Fabry-Perot cavity. The amplification medium ensures that only the mode that coincides with the vernier filter is amplified, giving a good single mode behaviour.

With the power injected in the heaters, the temperature in the rings can reach several hundred degrees Celsius. To limit thermal crosstalk, heaters are set a minimum of $100\mu\text{m}$ from any other heat-sensitive structure.

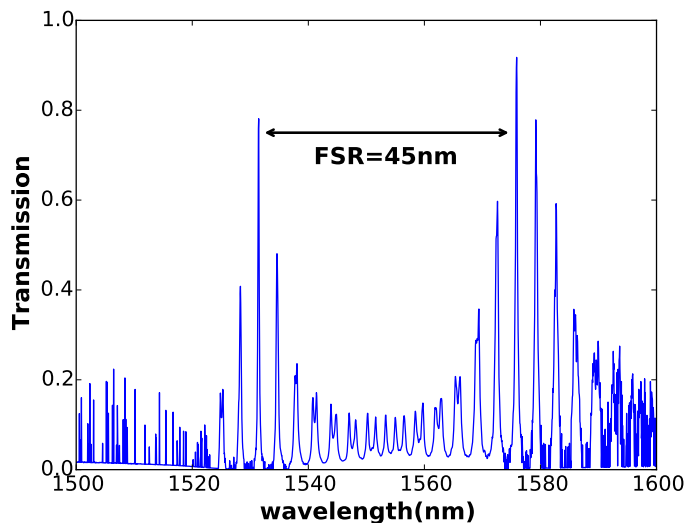


FIGURE 4.7: Spectrum of a Vernier filter made of two rings with FSR of 400GHz and 430GHz with coupler transmission coefficient $T=0.9$

Many design variations of the double ring tunable laser have been implemented in the past, from the use of a serial double ring cavity [2, 8, 18] to more complex geometries with for instance rings integrated in a Sagnac mirror [19] or parallel ring resonators [20].

4.3.2 Experimental results

The “standard” tunable laser (TUL) therefore consists of a gain section, mirrors on both sides of the cavity and a double ring filtering system, as displayed in figure 4.8.

Measurement were made on standalone tunable lasers without other integrated functions. The power and current curves in function of injected current in the laser section are presented in figure 4.9a. The laser has a maximum power of almost 2mW with a threshold of 30mA. The power curve displays discontinuities or “jumps”. Those are caused by the heating of the gain section : the power injection in the gain section creates heat, that heat creates a change in the optical length of the laser cavity. This causes a shift of the Fabry-Perot spectrum, thus

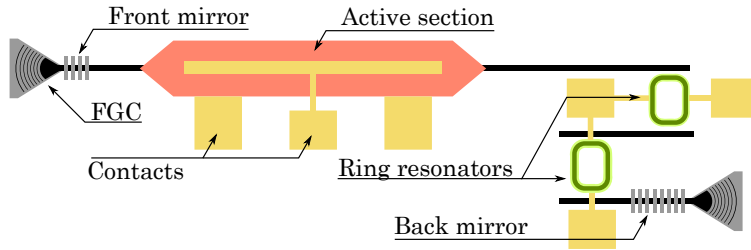
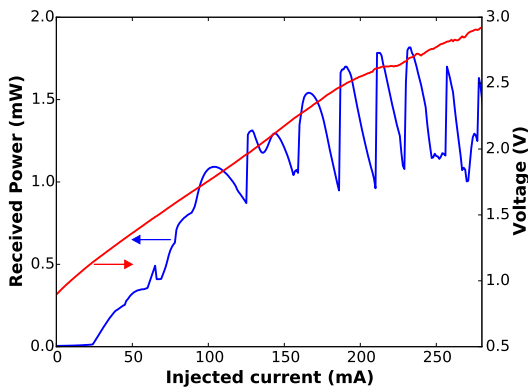


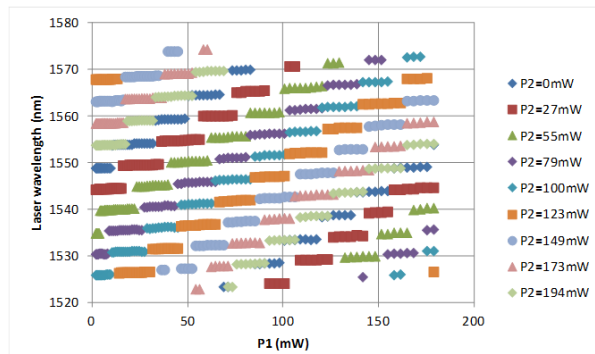
FIGURE 4.8: Schematic of a double ring tunable laser

changing the mode selected by the double ring filter. Each jump corresponds to a change of wavelength.

The tunability range was also measured in figure 4.9b. Power was injected in both rings and the wavelength was measured at each point. One can see that all wavelengths in the 45nm tuning range are accessible. The heating of a single ring shows the small jumps in wavelength that were predicted by the theory.



(a)



(b)

FIGURE 4.9: (a) Power and voltage of a tunable laser as a function of injected current, without thermal tuning on ring resonators (b) Laser wavelength in function of current injected in the first ring (P_1) and the second ring (P_2)

Figure 4.10 shows the laser spectrum for various wavelengths. The tuning range is 45nm with a side mode suppression ratio greater than 40dB.

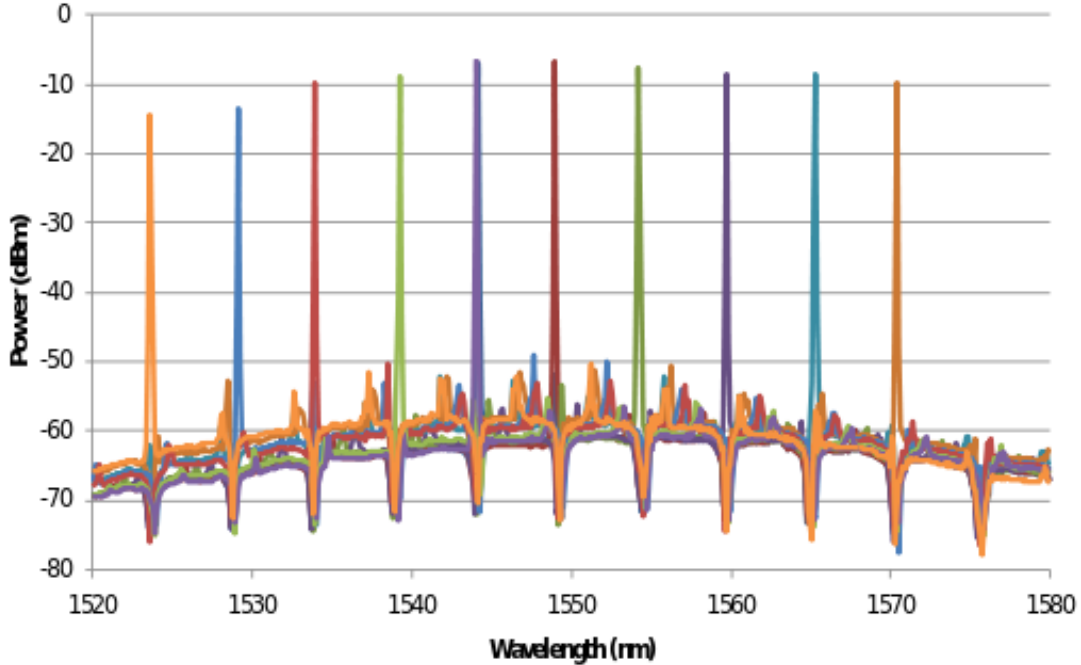


FIGURE 4.10: Spectrum of a tunable laser at various wavelengths

4.4 Electro-absorption modulators

Electro-absorption modulators (EAM) are another kind of component that can be made out of a gain section. In this case, instead of applying a direct bias, the gain section is reverse-biased. Instead of injecting light from a current, light is absorbed and creates a current. The interesting property of the EAM is to have an absorption spectrum that depends on the bias. The EAMs presented in this section use the confined Stark effect in the quantum wells to realise that modulation function [21].

Figure 4.11 explains the principle of the EAM. In the unbiased state, the EAM has an absorption spectrum (the red, “ON state” curve) with an absorption edge at a short wavelength. When the EAM is biased, the absorption edge is shifted towards longer wavelengths (the blue “OFF state” curve). An optical signal with a wavelength located just on the right of the unbiased absorption edge won’t be absorbed in the “ON state” and will be absorbed in the “OFF state”. One can thus modulate the optical signal by simply changing the bias of the EAM. An excitonic absorption peak is also present as a side effect of the confined Stark effect.

For an epitaxial structure with a maximum gain centered around $1.54\mu\text{m}$, the absorption edge is located around $1.55\mu\text{m}$. In our current process, the light source and the EAM have the same epitaxial structure. Because of that, the wavelength range that can be used is reduced to the wavelengths above $1.55\mu\text{m}$.

EAMs have been created and measured on both the InP platform [22] and the hybrid

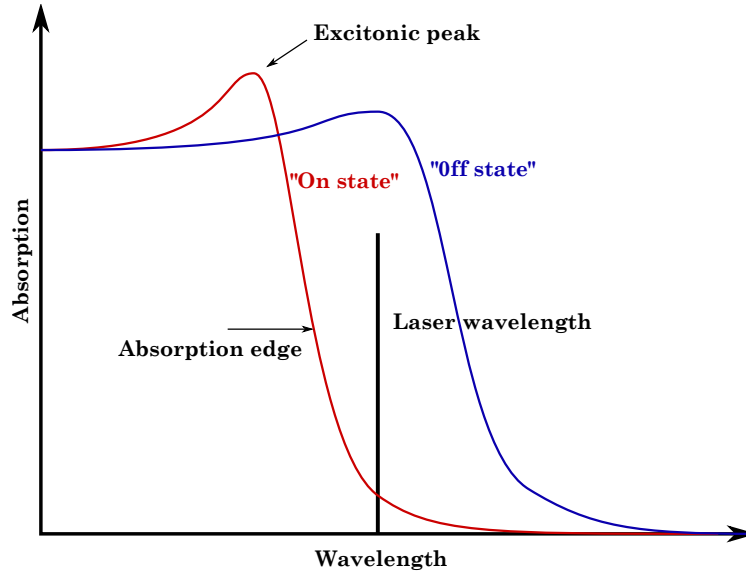


FIGURE 4.11: Principle of an electro-absorption modulator

silicon platform. On the latter platform, transmissions were made up to 67Gbit/s in the O-band with a wavelength window of 30nm [23]. The EAM was also integrated with a DFB laser source with transmission up to 50Gbit/s [24].

4.4.1 Integrated laser with modulator : first generation

In order to have more efficient devices, the trend is to integrate multiple functions on the same chip. In this section, the tunable laser source is integrated with the EAM modulator.

Figure 4.12 shows a schematic layout of the photonic integrated circuit. It consists of a tunable laser, the same as described earlier, whose output is coupled to an EAM via a silicon optical waveguide. The output of the modulator is then connected to a vertical grating coupler, which is used to couple light to a standard single mode fiber. The EAM is $300\mu\text{m}$ long section and has the same layer structure as the laser.

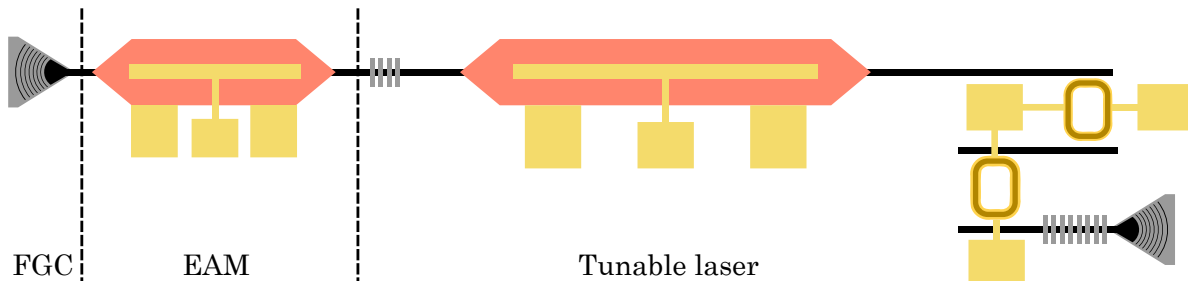


FIGURE 4.12: Schematic of EAM with integrated laser source

Static characteristics

For all experiments, the laser bias current is set around 120mA. The tunable laser itself has a tuning range of 45nm. As the EAM has the same epitaxial layer structure as the laser, the wavelength range in which the EAM operates efficiently is reduced from 50nm [25] to around 10nm. The fiber coupled output power after the EAM biased at 0V range from -20 to -23dBm. The low power at the end of the device is due to the vertical grating coupling losses (~ 6 dB) and high waveguide losses induced by unoptimal fabrication.

Figure 4.13a shows the superimposed optical spectra at four chosen wavelengths that range from 1551nm to 1561nm. Any wavelength between 1551nm and 1561nm is accessible. The single mode behaviour is excellent with a minimum of 45dB side mode suppression ratio (SMSR).

Figure 4.13b shows the static response of the EAM when submitted to a DC bias. The laser is switched on with power injection bias around 120mA. This figure shows a very large extinction ranging between 35 and 40dB with the presence of an excitonic peak around -1.5V bias. This peak is less pronounced and shifts to the left at longer wavelength. This can be explained by the larger wavelength detuning with respect to the absorption edge. On the other hand, the slope between 0 and -1.5V is very steep and remains almost unchanged with wavelength. The optimal bias condition is between -0.5 and -1.0V and the peak to peak voltage is less than 1V for 10dB extinction ratio.

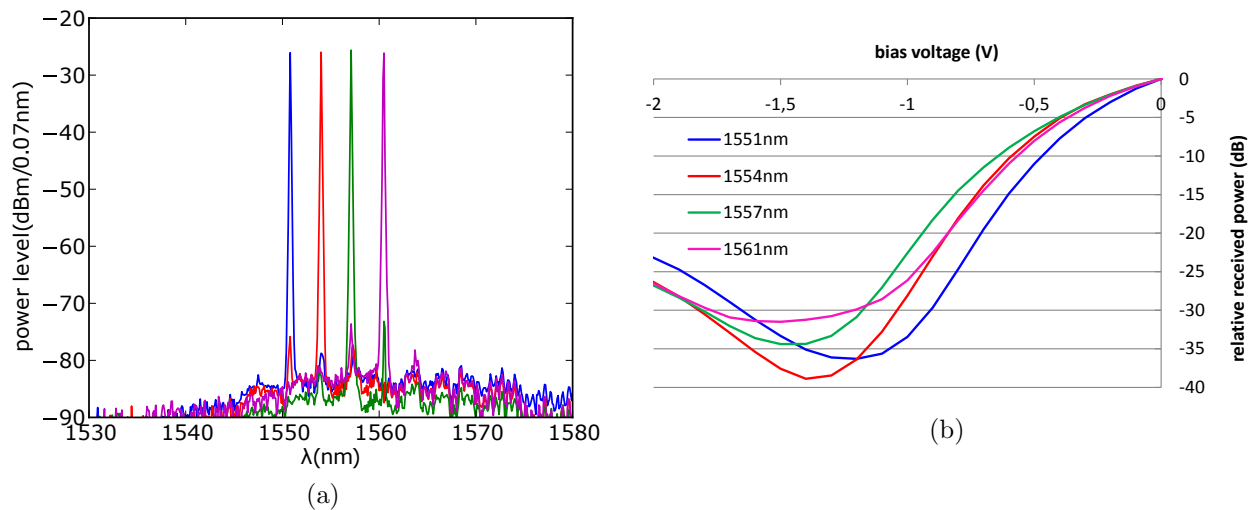


FIGURE 4.13: (a) Optical spectrum at the output of the component under modulation conditions (b) Static extinction of the EAM in function of applied bias.

Small signal bandwidth

Measurements of the small signal electro-optical modulation bandwidth of the sample were made. To do so, an electrical signal with small periodic perturbations is applied to the

EAM. The optical response is compared to the electrical injection signal in order to extract the transfer matrix of the component, and especially the S_{21} parameter.

Figure 4.14a shows the optical parameter S_{21} at 1555nm for various bias. The electro-optical bandwidth is around 5GHz at 0V and at -0.5V bias. On the other hand, the bandwidth is lower at -1V. At this bias, the system oscillates around the excitonic peak with a reduced absorption slope, which explains the degraded bandwidth.

Figure 4.14b shows S_{21} at a bias of -0.5V for various wavelengths. The optical response is nearly identical for all wavelengths, with again a 3dB bandwidth around 5GHz.

The low 3dB bandwidth of 5GHz is mainly due to the size of the EAM. The active section is $300\mu\text{m}$ long. With that size, capacitive effects are important and create a limited bandwidth. On the other hand, the extinction ratio is extremely large. A shorter EAM would have a higher bandwidth in exchange for a lower extinction ratio. With that bandwidth, one can expect to make transmissions up to 10Gb/s at maximum.

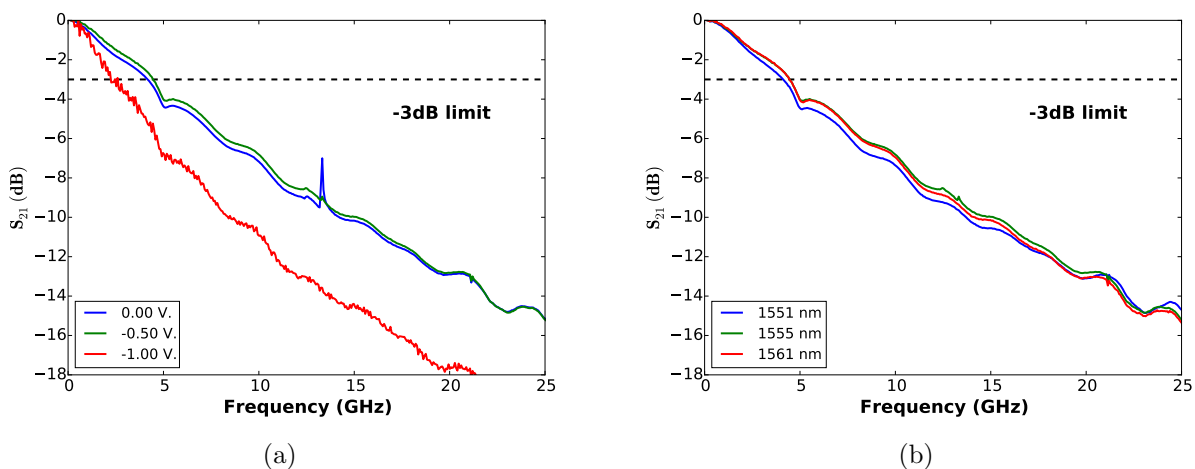


FIGURE 4.14: (a) Optical S_{21} at 1555nm for various bias (b) Optical S_{21} at -0.5V for various wavelengths

Transmission & bit error rate

Transmission measurements were performed at 10Gbit/s for the four wavelengths expressed earlier in the static measurement section. The setup used for these measurements is specific for bit error rate (BER) and eye diagram measurements. A schematic of the setup is presented in figure 4.15. Light is coupled out of the sample with a monomode fiber. The signal then passes through an erbium doped fiber amplifier and filtered with a band-pass tunable filter. The signal is then transmitted through a propagation fiber with lengths of 0km, 25km, 35km and 50km. The signal is then switched to the desired measurement instrument. The BER is measured with a high sensitivity avalanche photodiode receiver with a sensitivity of -28.5dBm at 10^{-10} BER. Eye-diagram and BER are measured for each wavelength. The pseudo random binary sequence (PRBS) length is $2^{31} - 1$.

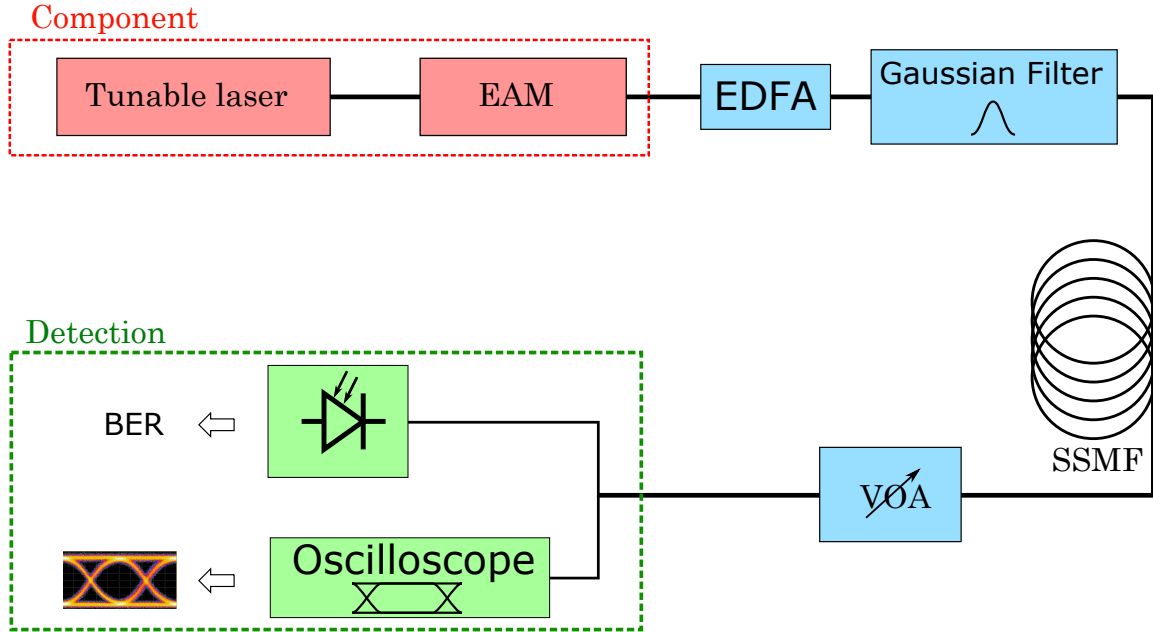


FIGURE 4.15: Schematic of EAM with integrated laser source

Fig 4.16a shows the measured BER. One can see that the power level enabling a BER of 10^{-10} is around -26dBm for back to back, quite close to the reference level of -28.5dBm. Error-free operation is obtained for all measured wavelengths up to 50km. Since the EAM section has not been optimised, the chirp leads to transmission penalties of 3dB at 25km and 8dB at 50km.

Fig 4.16b shows all the eye diagram measured for this experiment. The eye shape is very similar for all wavelengths and remains opened until 35km. The eye becomes nearly closed for a distance of 50km. The average dynamic extinction ration in back to back is around 7dB.

The optical budget for this specific sample is low (less than 4dB for back to back operation at 10^{-9} BER) because of the low output power coupled to the fiber. This sample however performed the first demonstration of an integrated tunable laser with electro-absorption modulator on the hybrid III-V on silicon platform. These results were presented at the OFC conference in 2016 [26].

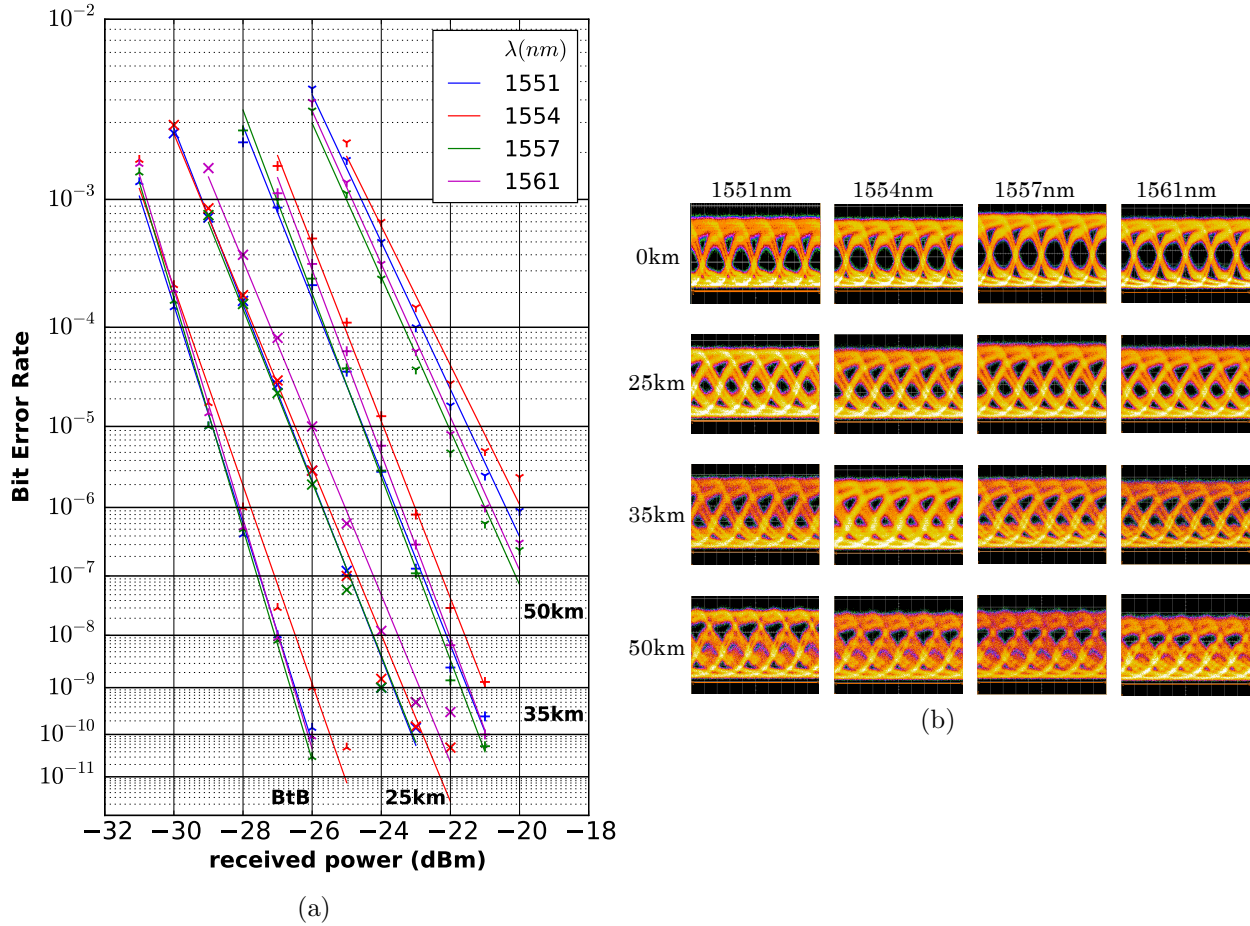


FIGURE 4.16: (a) Bit error rate at 10Gbit/s vor various wavelengths and propagations distances (b) Eye diagramm at 10Gbit/s for the same wavelengths and propagation distances

4.4.2 Integrated laser with modulator : second generation

The previous section showed a transmission with an integrated tunable laser with EAM. The transmission was made up to 50km at 10Gbit/s, but the optical budget was very low. A second generation was processed which has a much higher output power. The sample has an output power around -7 dBm with an unbiased EAM compared to -20 dBm for the previous sample.

The laser spectrum was measured at 1564nm and presented in figure 4.17. The laser spectrum is excellent with a side mode suppression ratio greater than 50dB. For this sample, the epitaxial layer presents an offset in gain spectrum. The transparency region of the EAM is shifted to the longer wavelengths. The useful range is in this case from 1555nm to 1564nm (instead of 1551-1561nm in the previous sample).

A transmission was performed at 10Gbit/s with the same setup (figure 4.15). The results are presented in figure 4.18 with only two wavelengths displayed for readability reasons. The BER of 10^{-9} is obtained for powers around -24dBm for the back to back configuration. The

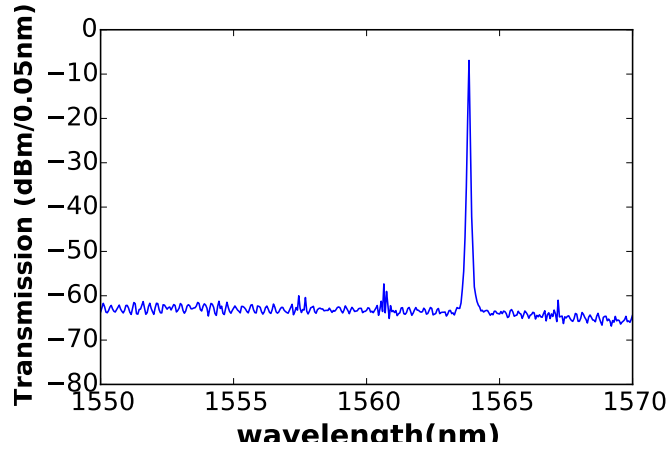


FIGURE 4.17: Laser spectrum after the EAM

power penalty is therefore of 4.5dB (compared to 2dB for the first generation) on back to back. On the other hand, the penalty for 25km propagation remains nearly identical. A BER of 10^{-9} was not obtained for the longer distance of 50km. A forward error correction (FEC) is therefore necessary for this distance.

The output power under modulation conditions is about -15dBm for a polarisation bias of $-1V$ with modulation of $1.15V_{pp}$. The optical budget is therefore much better than for the previous sample with almost 10dB for back to back operation (compared to 4dB).

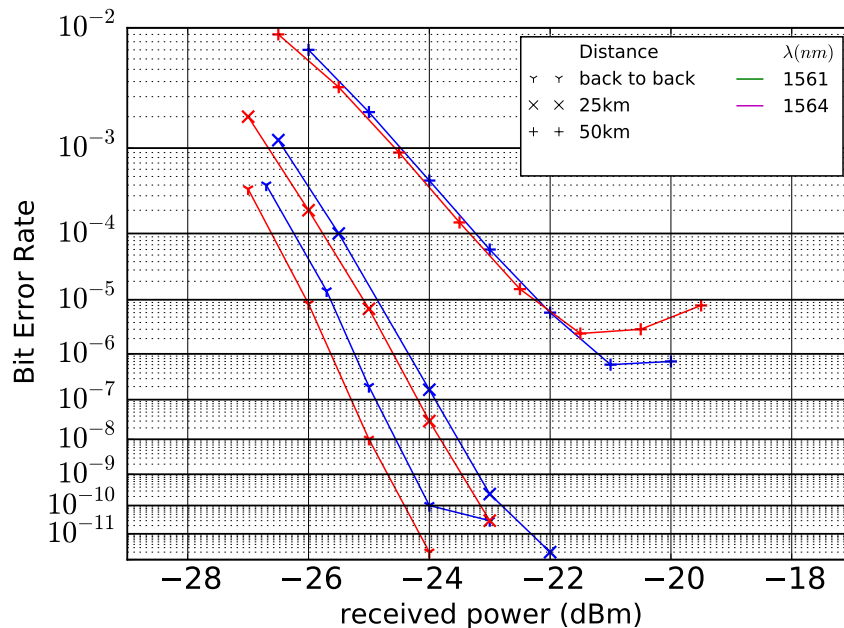


FIGURE 4.18: Bit error rate for a bias polarisation of $-1V$ for various wavelength and distances

This second generation has similar performances than the previous one, but with much higher output power, giving a higher optical budget. The next generation will have an implantation in the EAM active region in order to reduce the size of the injected section to $150\mu m$ (instead of $300\mu m$). This should reduce the EAM's capacitance and enable operation up to 25Gbit/s.

4.5 Modulation with silicon junctions

The second type of active components studied in this chapter are the silicon PN junctions. The doped silicon can create junctions where the carrier density can be changed by an electrical injection. This modified carrier density will alter the refractive index of the material and thus the effective index of any mode propagating close to that junction. A tailored interference can then transform this effective index change in amplitude or phase modulation, most often in a ring resonator configuration or in a Mach-Zehnder configuration.

4.5.1 Different types of silicon junctions

The silicon platform enables multiple kinds of modulator junctions. The most commonly used is the lateral PN junction that will be described in detail in the next sections. But other kind of junctions exist and have been implemented in the past. Figure 4.19 shows a schematic of the most common kinds of modulator junctions on the silicon platform. The PN lateral junction consists of doped regions in the optical waveguide. The junction is perpendicular to the optical propagation direction, hence the “lateral” junction. The interleaved PN junction is similar to the lateral PN junction, only with interleaved doped regions that are parallel to the optical waveguide. The PIN junction is a variant of the PN lateral junction : the two doped layer are separated by a thin layer of intrinsic silicon. The MOS-capacitor junction relies on carrier accumulation at the interface between the doped region or depletion. The two regions are separated by an isolant, usually silica.

The performances of each junction can be characterised by a few parameters : the modulation speed, the optical losses and the $V_\pi L_\pi$. This last parameter is very important as it defines the phase shift efficiency. It corresponds to the applied voltage multiplied by modulator's length that are necessary to obtain a π phaseshift.

Table 4.1 gives modulator characteristics for a few selected components in the literature. The MOS-capacitor modulator has the best $V_\pi L_\pi$, but this comes at the cost of higher losses, up to 6.5dB/mm. Lateral and interleaved PN junctions have similar performances with a $V_\pi L_\pi$ of 2.4V.cm and losses of 1dB/mm.

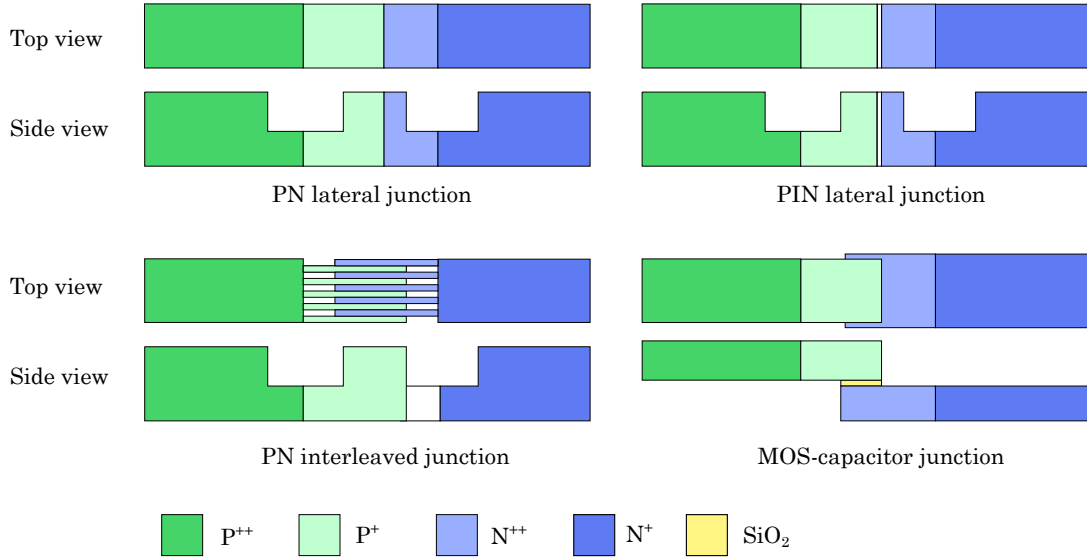


FIGURE 4.19: Schematic of a PN-junction

Junction type	year	Max. speed (Gbit/s)	$V_{\pi}L_{\pi}$ (V.cm)	losses	implementation
MOS-capaciitor [27]	2014	28	<0.2	6.5dB/mm	MZ
lateral PN [28]	2015	25	2.4	1dB/mm	MZ
lateral PN [29]	2015	56	~ 1.3	~ 18 dB	RR
interleaved PN [30]	2013	40	2.4	1dB/mm	MZ
lateral PIN [31]	2014	56	-	5.3dB/mm	MZ

TABLE 4.1: Performances of a selection of silicon modulators

4.5.2 the PN junction

The PN junction consists of a rib waveguide with dopant implantations as displayed in figure 4.20. The dopant changes the electrical properties of the material : the silicon's conductivity increases. The frontier between the P-dopant and the N-dopant is what makes the PN junction.

The junction has a diode electrical characteristics : when biased in the forward direction, a current passes through. When polarised in the reverse direction, the current is stopped : electrons and holes deplete on either sides of the junction. This carrier accumulation creates a small change on the silicon refractive index, that can be further used to create interferences.

Figure 4.21 shows the simulated dopant concentration repartition in the waveguide, taking into account dopant activation and diffusion during the fabrication process. The concentration is medium close to the junction in order to mitigate the optical losses due to dopants.

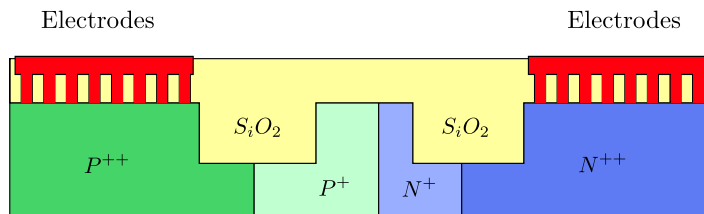


FIGURE 4.20: Schematic of a PN-junction

The concentration far from the waveguide is much higher in order to decrease the access resistance.

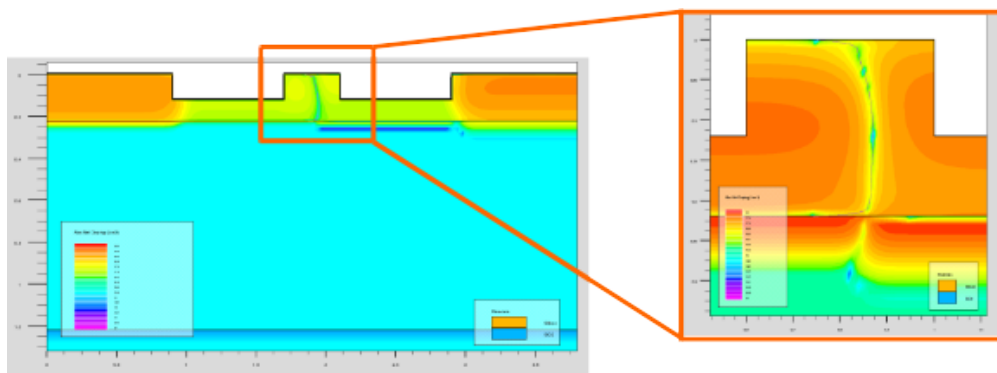


FIGURE 4.21: Simulation of dopant concentration in a PN junction. Courtesy of Leti.

From this doping profile, an electro-optic simulation can be made that gives the performance of the simulated junction as a function of the dopant density. The main merit factors are the optical losses caused by the junction and the $V_\pi L_\pi$. Figure 4.22 shows the simulation results for various P and N dopant concentration. Each curve is made with a constant N-dopant concentration with P-dopant concentration increasing from leftmost point to rightmost point. Concentrations are expressed in number of atoms per cm^3

4.5.3 Mach-Zehnder modulators

The PN junction was implemented in a Mach-Zehnder configuration. The fabrication for the first generation presented here was performed on the 220nm platform at Leti. One of the arms has an additional phaseshifter in the form of a heater. By varying the heater power, one can tune the static phase difference in the modulator. Figure 4.23a shows the variation of output power as a function of the injected heater power. Each curve corresponds to a different junction bias, from 0V to -5V. The curves are sinusoidal functions, as expected from a Mach-Zehnder interferometer (see section 2.7).

The bias of the junction creates an additional phaseshift, which explains why the sinusoidal curves are shifted for decreasing values of bias voltage. A fit was made on each of

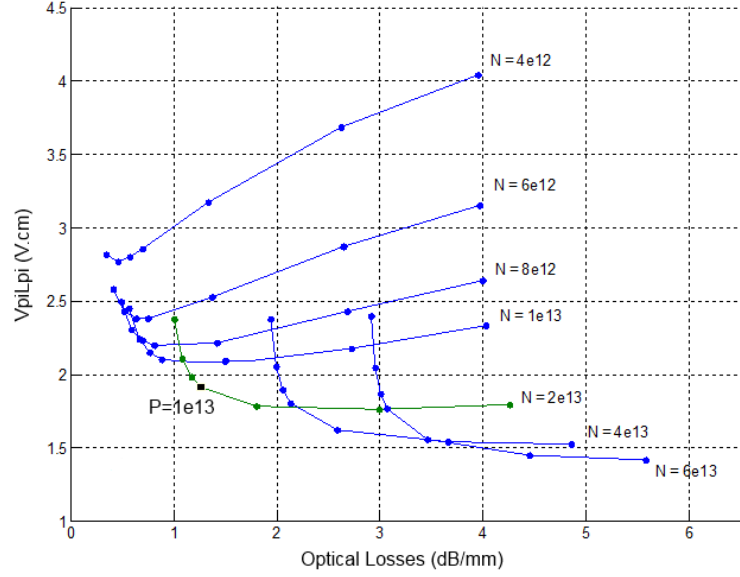


FIGURE 4.22: Simulation of modulator efficiency vor various concentrations of P and N dopants. Each curve is made with a constant N-dopant concentration with P-dopant concentration increasing from leftmost point to rightmost point. Courtesy of Leti.

these curves with a sinus function. The phaseshift was extracted and plotted of figure 4.23b. The length of the junction is 4mm. We can therefore extract the $V_{\pi}L_{\pi}$ of the junction. The efficiency decreases as the voltage decreases : at higher voltage, all the carriers close to the junctions have already been extracted. The $V_{\pi}L_{\pi}$ at -5V is about 2.3V.cm. from the slope, we can expect a $V_{\pi}L_{\pi}$ lower than 3V.cm at larger bias.

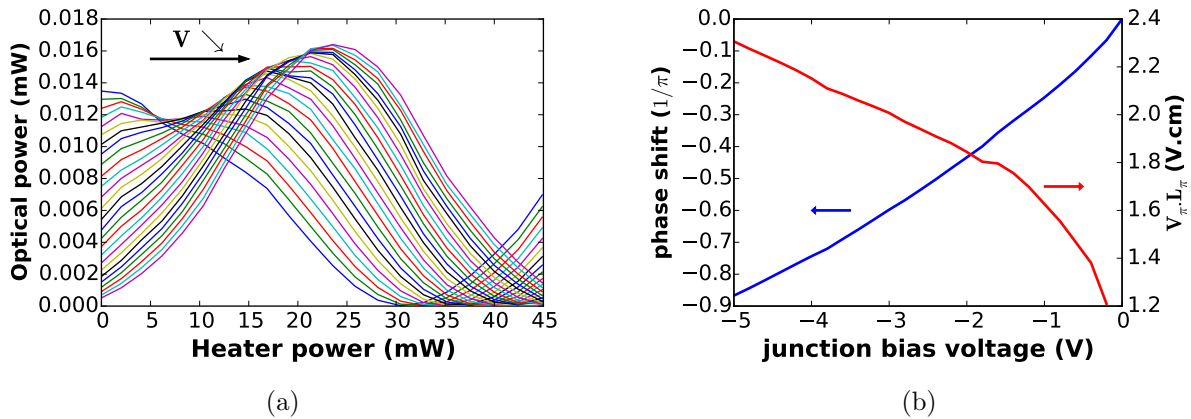


FIGURE 4.23: (a) Power at the output of the modulator in function of injected power in heater for various junction polarisation bias. the guide geometry is a rib 200-150 W0.4 (b) Extracted values of phaseshift (left axis) and $V_{\pi}L_{\pi}$ (right axis)

The small signal electro-optic response of the sample was also measured. Figure 4.24 shows the optical S_{21} parameter in function of frequency for different bias voltage. The bandwidth is nearly identical for the three bias, with a 3dB bandwidth around 12GHz.

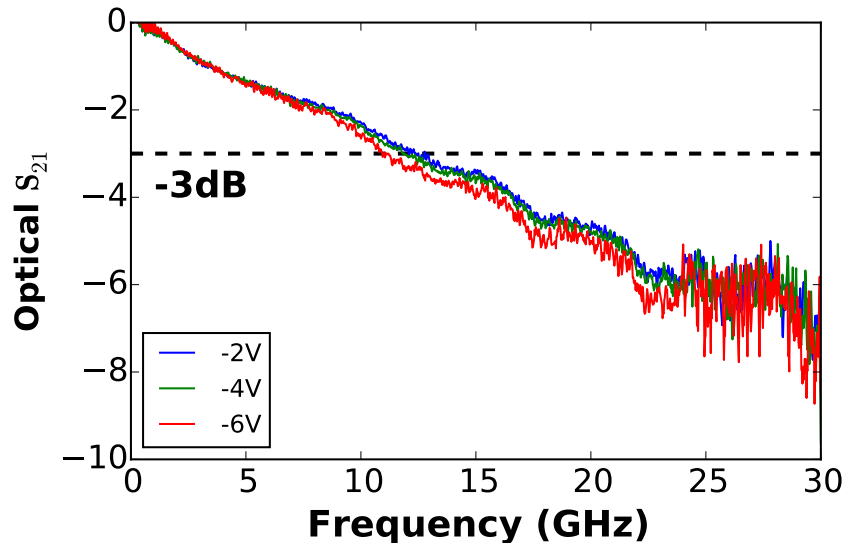


FIGURE 4.24: Electro-optical bandwidth of a Mach-Zehnder silicon modulator.

4.6 I/Q modulators

As explained earlier in section 1.1.3, phase modulation in conjunction with amplitude modulation can increase the aggregated bitrate of a transmission while keeping relatively low modulation speed. This section explains how to design an In-phase/Quadrature modulator (I/Q modulator). Two kinds of modulators are studied. First the silicon I/Q modulator which is very similar to commercial I/Q modulators and later the EAM I/Q modulators.

4.6.1 I/Q modulators with PN junctions

push-pull modulator

The basic building block of the I/Q modulator is a simple Mach-Zehnder interferometer with a “push-pull” configuration. This means that both arms have reverse-biased PN junction with junctions biased in two opposite positions. That configuration is explained in schematic 4.25a. The first arm of the Mach-Zehnder receives a bias of $V_1 = V_0 + \Delta V$ with V_0 a constant and ΔV the modulation bias. The second arm receives the symmetric bias $V_2 = V_0 - \Delta V$ and has a phase difference of π with the first arm. The resulting signal at the output of the Mach-Zehnder is represented in figure 4.25b as the purple circles. The output signal is the sum of the two arms, represented by red and blue circles. With the push-pull configuration,

the output signal always remains on the in-phase axis. Depending on the applied bias ΔV , one can have a phase of 0 or π and a varying amplitude. This Mach-Zehnder can be used both as a phase switcher and an amplitude modulator.

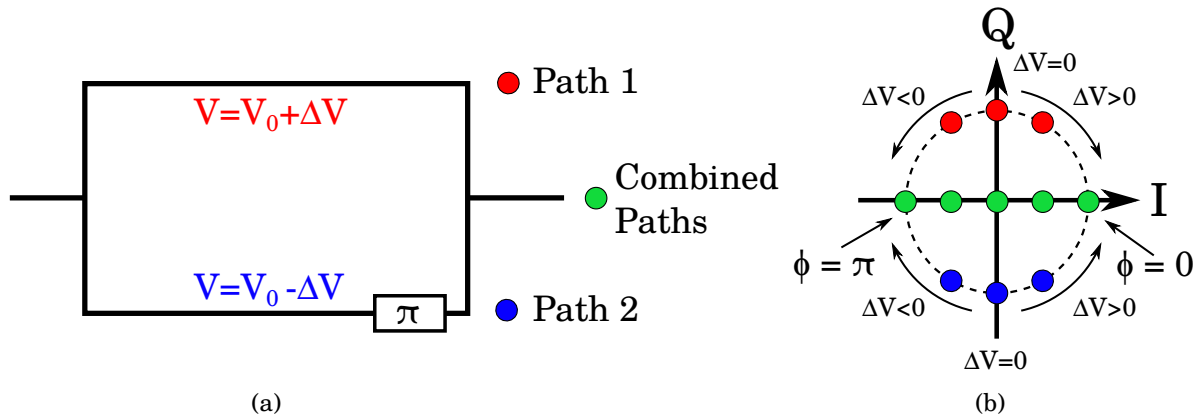


FIGURE 4.25: (a) Schematic of a Mach-Zehnder modulator in push-pull configuration with applied bias (b) Corresponding constellation diagram with variations of ΔV

Combining modulators to an I/Q modulator

A complete I/Q transceiver is constituted of two near-identical sections : one for each polarisation of the electrical field in the output fiber, as displayed in figure 4.26. Each of these contains an I/Q modulator, which consist of two Mach-Zehnder interferometers with push-pull configuration, one for the in-phase component and one for the quadrature component. Each of the Mach-Zehnder modulator can create the constellation diagram presented in the previous section. One of them has an additional phase shift of $\pi/2$ so that one modulator is always on the in-phase axis while the other is always on the quadrature axis. The combination of the two modulators gives access to every point on the constellation diagram.

The necessary building blocks for a complete integrated I/Q modulator are the following :

- A light source, preferably tunable. The classic tunable laser described in section 4.3 will be used.
- Power splitters to split the signal between the different Mach-Zehnder interferometers. Directional couplers are used in order to minimize reflections.
- Mach-Zehnder interferometers in push-pull configuration
- A polarisation rotator and polarisation combiner. The 2D fiber grating coupler combines the two functions (see section 2.3.2)
- Optionally an optical amplifier to boost the signal after the numerous propagation losses. An SOA is used for that function.

All these building blocks were implemented in the final layout shown in figure 4.27. The laser, SOA and output are positioned between the two I/Q modulators. Travelling

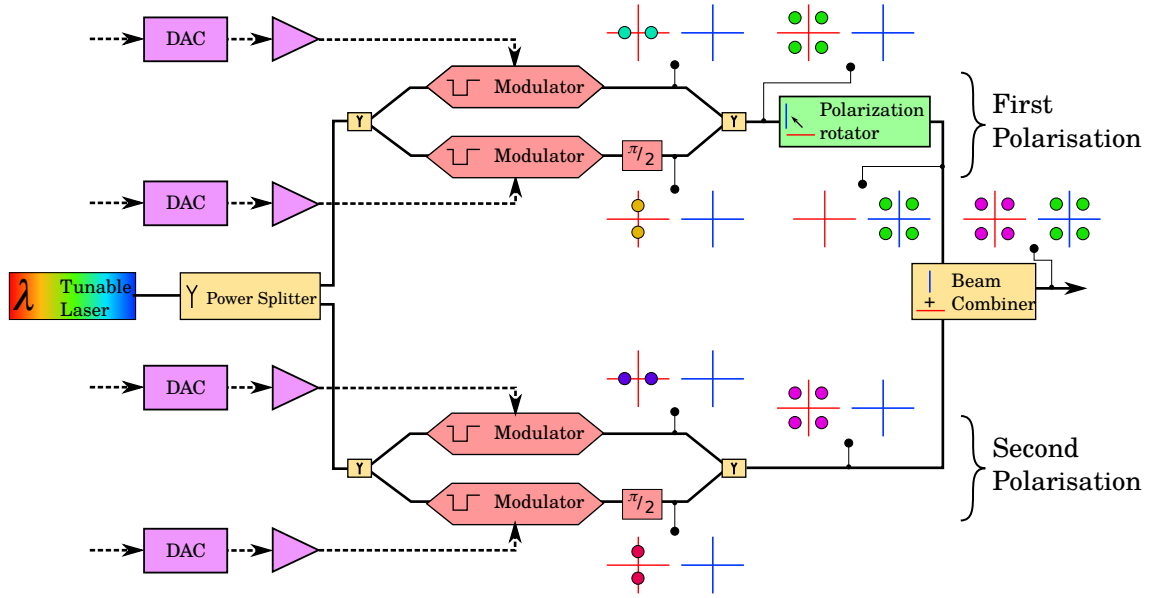


FIGURE 4.26: Schematic of a dual-polarisation I/Q transceiver.

wave electrodes are designed with bonding pads close to the border of the chip in order to minimise the bonding distance from the access lines. Auxiliary input and outputs were added on each modulator in order to characterise the device without interferences from the other blocks. They were used to characterise the static and dynamic properties of the PN-junction presented in section 4.5.

Fabricated component

Many layouts were designed during the thesis, but only one design had enough time to come back from the fabrication process. Static and small signal bandwidth measurements were made on silicon modulators and were presented in section 4.5. The insertion losses at $1.55\mu m$ for a single Mach-Zehnder are about 17dB. This high insertion loss can be split into the elementary components :

- FGC : $\sim 2 \times 5dB$
- MMI : $\sim 2 \times 1dB$
- Propagation losses in the junction : $\sim 4dB$
- Propagation losses outside the junction : $\sim 1 - 2dB$

Figure 4.28 shows a picture of the I/Q modulator of that first generation.

The fully integrated devices coming from the first fabrication did not work due to some fabrication issues. The second run is actually ongoing.

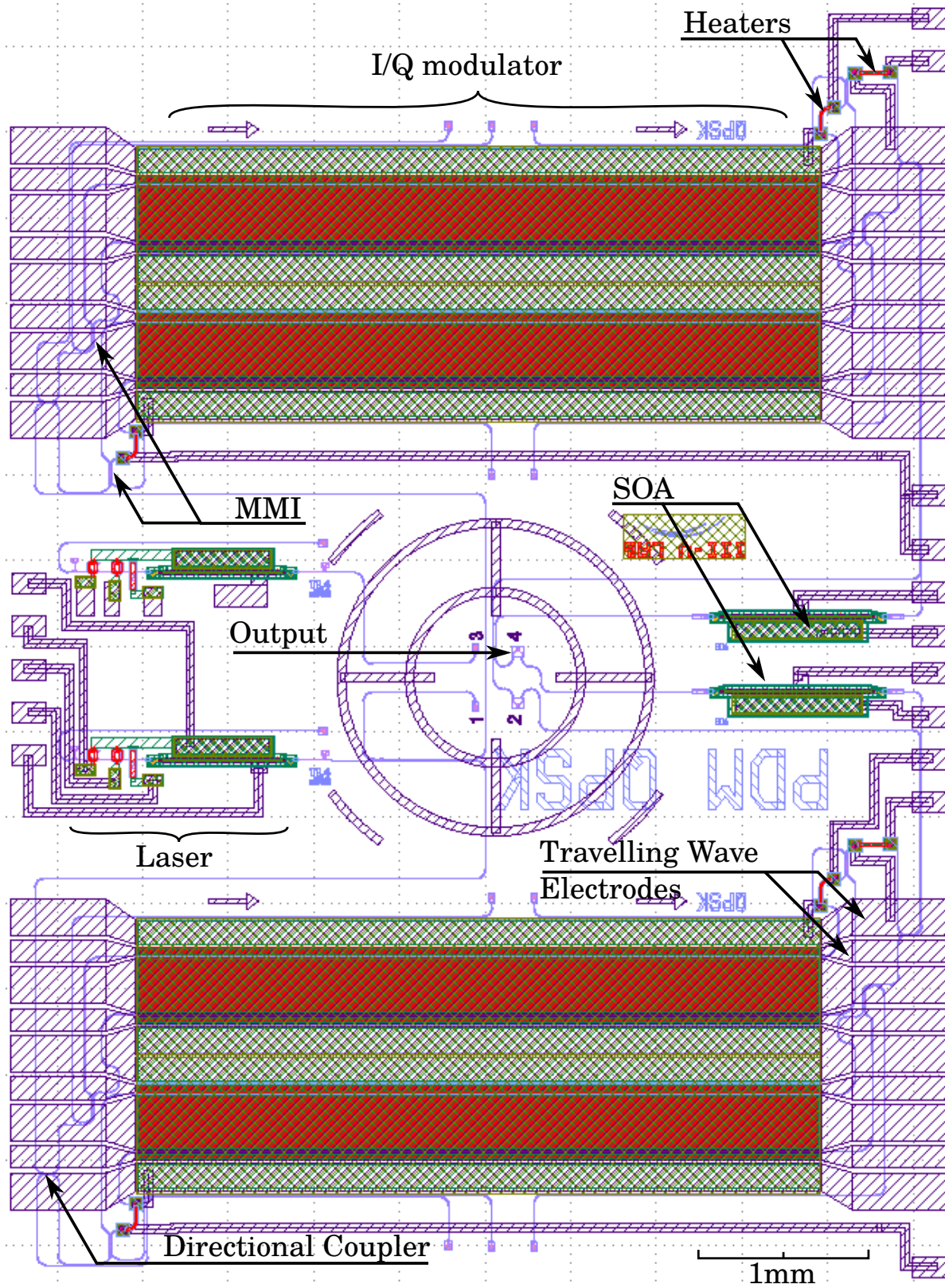


FIGURE 4.27: Layout of the silicon I/Q transceiver

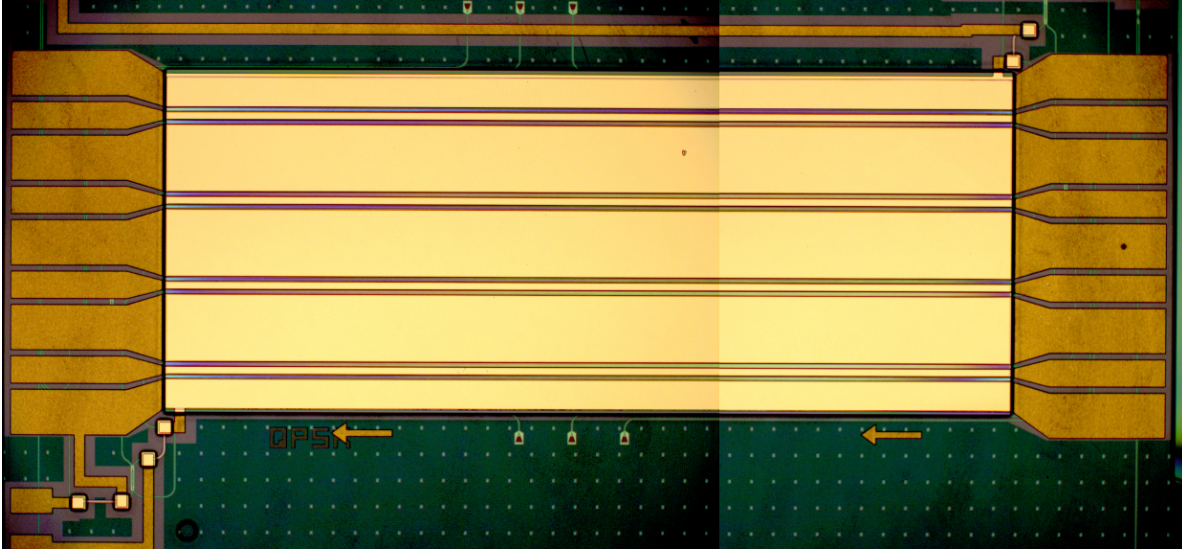


FIGURE 4.28: Mosaic Picture of an I/Q silicon modulator on optical microscope with 5X zoom.

4.6.2 I/Q modulators with electro-absorption modulators

I/Q modulator can also be made out of EAM instead of silicon PN junctions. This system relies once again on a Mach-Zehnder geometry. The main difference is that there is no phase tuning nor interferences. The two arms have a constant π phase difference, the EAM is used to switch off the light from one arm and let the light from the other arm go through [32, 33]. This principle is explained in figure 4.29. The left part shows the light paths with the top EAM in the “through” state and the bottom EAM in the “stop” state. The right part shows the reverse situation. With the added π phase shift on the lower arm, the signal strength remains the same in both cases but the phase is changed.

This configuration presents the advantage of using EAM instead of silicon PN junctions. The required bias voltage is therefore much lower with lower power consumption. But this comes at the cost of additional losses : half of the signal is lost in the “stop” EAM and another half is lost at the power combiner, for a total additional loss of 6dB. On the other hand, there are fewer additional losses due to waveguide propagation. In the end, the EAM I/Q modulator might have lower overall losses despite the intrinsic 6dB loss from the EAM.

Apart from the phase modulator building block, the base buildings blocks for the complete transceiver are the same as for the silicon-modulator transceiver.

RF electrodes

In the chosen configuration, a long RF line is required to drive the EAM. This line should bring as little perturbation as possible to the electrical signal with minimum propagation losses. The line should operate with frequencies larger than 20GHz for a target modulation at 25Gbit/s. The chosen line structure is the micro-strip. This structure has the advantage

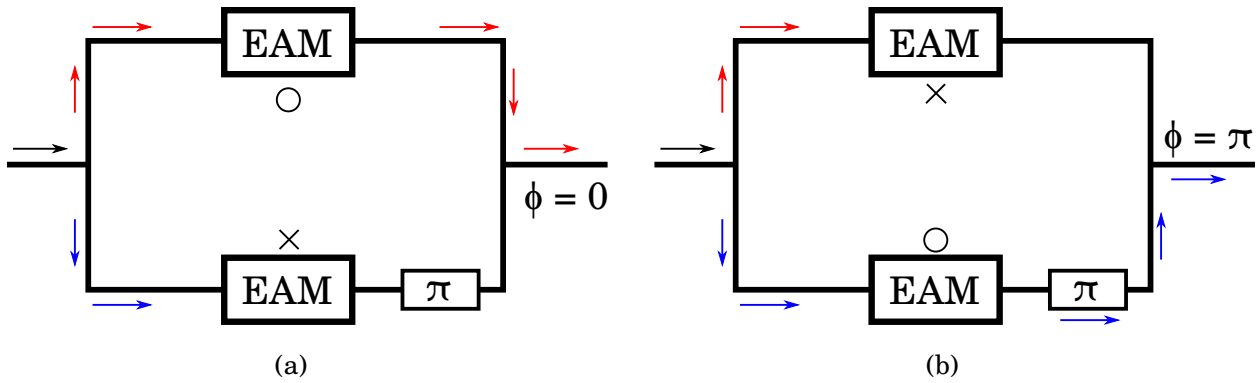


FIGURE 4.29: Schematic of an EAM phase modulator with one EAM in the "through" state and one EAM in the "stop" state. (a) Top EAM is "through" (b) Top EAM is "stop"

of not being sensitive to bends. In this stack, the electric field lines are all between the signal line and the ground plane (see figure 4.30a). This configuration considerably reduces interactions with the layers beneath the microstrip and especially the optical waveguides.

The micro-strip structure is presented in a schematic in figure 4.30b with a dielectric layer made out of BCB with $H \simeq 6\mu m$ and a line height of $h \simeq 1\mu m$. The line's width was tuned to have a characteristic impedance close to 50Ω . The optimal width was simulated with a value of $W = 14.5\mu m$.

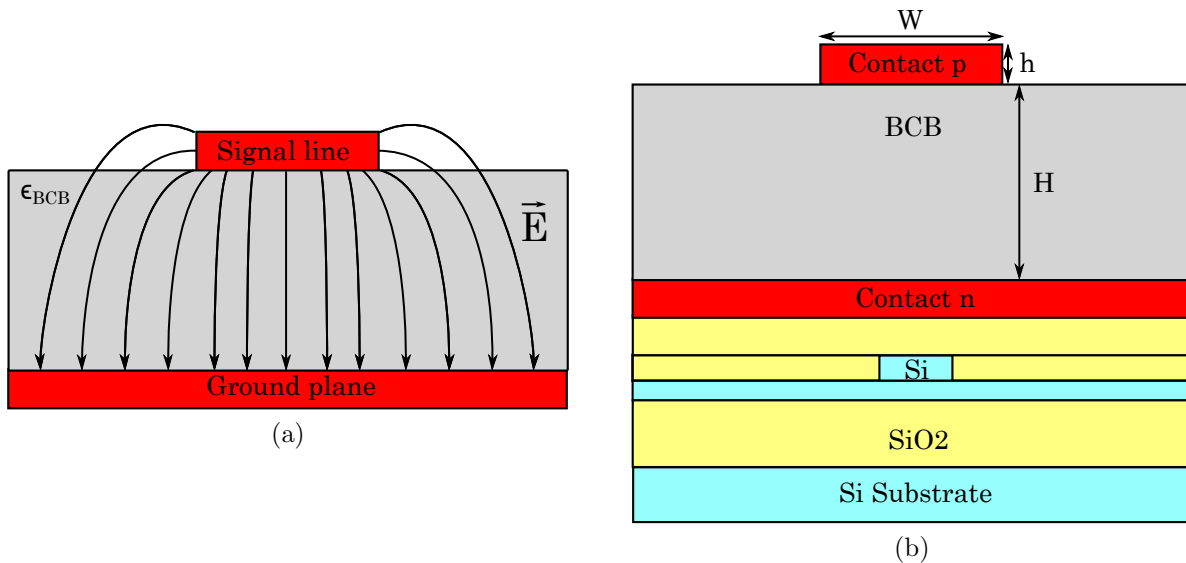


FIGURE 4.30: (a) Schematic of a generic microstrip with corresponding electric field lines. (b) Schematic of the whole microstrip structure with silicon guides beneath

A simulation of that microstrip was realised by our partners at CEA Leti. The results are presented in figure 4.31. Figure 4.31a represents the real part of the line's impedance. For a good impedance matching with electrical equipment, that value should be equal to 50Ω . The

line fulfils that condition for frequencies larger than 10GHz. Figure 4.31b shows the line's lineic losses as a function of frequency. The transceiver have lines with a maximum length of 1mm. The electrical losses should therefore be lower than 0.4dB on the whole targetted bandwidth.

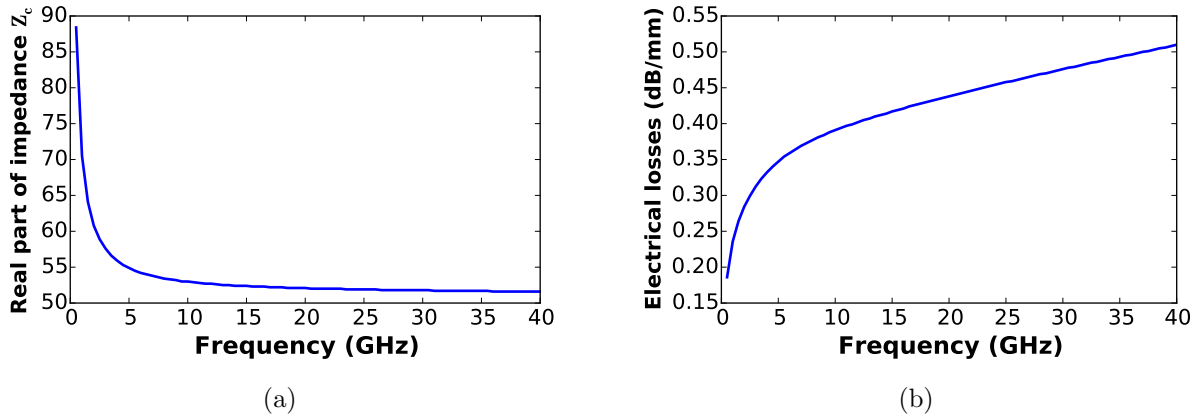


FIGURE 4.31: (a) Simulation results of the real part of a microstrip line impedance in function of signal's frequency (b) Simulation results of the lineic losses of a microstrip in function of signals's frequency

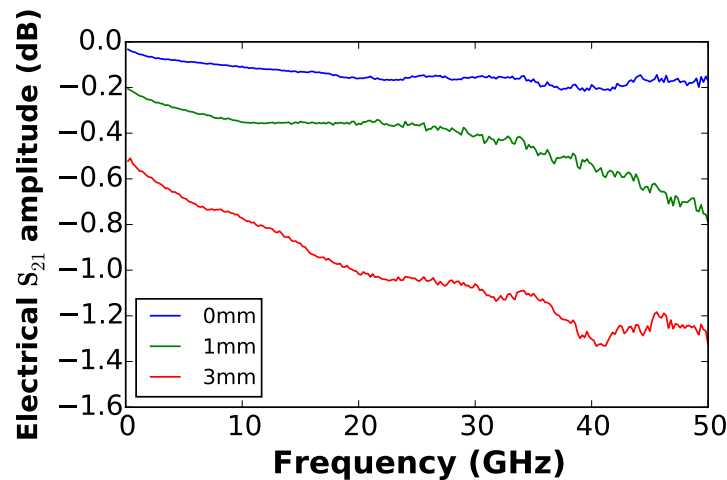


FIGURE 4.32: Measured S_{21} parameter in a microstrip line in function of frequency for various propagation lengths

Measurements were made on the fabricated microstrip line. Figure 4.32 shows the electrical parameter S_{21} which corresponds to the electrical losses from the beginning to the end of the line. The losses can be estimated to be around 0.2-0.4dB/mm, which is compatible with the simulation results. The losses for the 0mm line are driven by the adaptation section from the RF probe to the microstrip line.

Fabricated device

As for the silicon transceiver, many layouts were designed during the thesis, but only one reached the end of fabrication, on the same wafer as the silicon transceiver. A few of the functions could be tested, but the whole device was not fully functional.

An annotated picture of the fabricated device is presented in figure 4.33. The device is much more compact than the silicon transceiver due to the small footprint of the EAM.

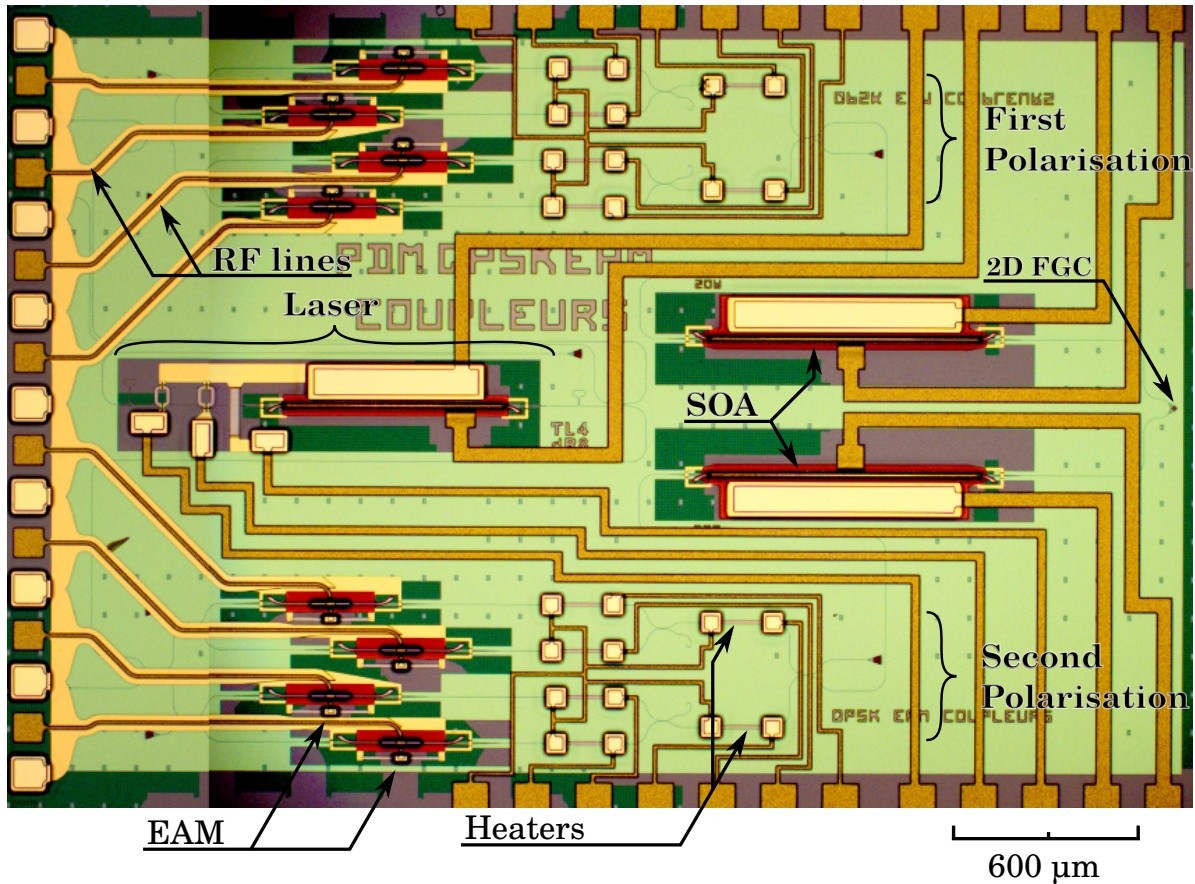


FIGURE 4.33: Mosaic picture on optical microscope of an integrated I/Q EAM transceiver

4.6.3 Silicon vs EAM I/Q modulator

Each of the two proposed solutions have advantages and drawbacks. The silicon transceiver has a much larger footprint than the EAM, but it has a wider tunability range for instance. A comparison is made between the two devices on table 4.2

	PN-junction	EAM
Footprint	5.5×7.5mm	3×4mm
Average bias voltage	-4V	-1V
Modulation amplitude	8V _{pp}	1V _{pp}
intrinsic modulator loss	~1dB/mm	6dB (EAM Mach-Zehnder)
Tunability range	45nm (limited by tunable laser)	10nm due to the same epitaxial structure for EAM and laser.

TABLE 4.2: Comparison of MMI and Directional couplers as power splitters

4.7 Conclusion

In this chapter were studied various active devices and their integration into more complex functions.

The first sections studied the hybrid III-V on silicon devices, namely the SOA, tunable laser and EAM. An SOA was fully packaged with a fiber to fiber gain larger than 5dB and an internal gain of 28dB. The tunable lasers exhibit a tuning range of 45nm with more than 1mW coupled to the fiber.

This chapter also shows the performances of the first tunable laser integrated with an EAM on the hybrid III-V on silicon platform with transmission at 10Gb/s. Two generations were demonstrated with similar performances but with a larger output power for the second generation, enabling an optical budget up to 10dB.

The next section studied the silicon PN-junction and their use in Mach-Zehnder interferometers. The measured junctions showed a $V_{\pi}L_{\pi}$ lower than 3V.cm with an electrical bandwidth reaching 12GHz.

The active devices discussed above were then integrated into PICs. Integrated I/Q modulators and coherent receivers integrating both active and passive elements were designed, and the fabrication is still on going. Measurement results are expected in the coming months.

References

- [1] L. CHEN et al. “Integrated GHz silicon photonic interconnect with micrometer-scale modulators and detectors”. In : *Optics express* 17.17 (2009), p. 15248–15256.
- [2] K. NEMOTO, T. KITA et H. YAMADA. “Narrow spectral linewidth wavelength tunable laser with Si photonic-wire waveguide ring resonators”. In : *The 9th International Conference on Group IV Photonics (GFP)*. 2012.
- [3] J. DALLESASSE et S. B. KRASULICK. *Method and system for template assisted wafer bonding*. US Patent 8,222,084. Jul. 2012.

- [4] C.-C. LIU et al. “The microstructure investigation of flip-chip laser diode bonding on silicon substrate by using indium-gold solder”. In : *IEEE Transactions on components and packaging technologies* 26.3 (2003), p. 635–641.
- [5] S. TANAKA et al. “High-output-power, single-wavelength silicon hybrid laser using precise flip-chip bonding technology”. In : *Optics express* 20.27 (2012), p. 28057–28069.
- [6] A. Y. LIUA et al. “Quantum dot lasers on silicon”. In : (2014).
- [7] M. LAMPONI et al. “Low-threshold heterogeneously integrated InP/SOI lasers with a double adiabatic taper coupler”. In : *IEEE photonics technology letters* 24.1 (2012), p. 76–78.
- [8] A. LE LIEPVRE et al. “Widely wavelength tunable hybrid III–V/silicon laser with 45 nm tuning range fabricated using a wafer bonding technique”. In : *The 9th International Conference on Group IV Photonics (GFP)*. 2012.
- [9] A. W. FANG et al. “Electrically pumped hybrid AlGaInAs-silicon evanescent laser”. In : *Optics express* 14.20 (2006), p. 9203–9210.
- [10] G.-H. DUAN et al. “Hybrid III–V on Silicon Lasers for Photonic Integrated Circuits on Silicon”. In : *IEEE Journal of selected topics in quantum electronics* 20.4 (2014), p. 158–170.
- [11] M. G. WILSON et G. TEH. “Tapered optical directional coupler”. In : *IEEE Transactions on Microwave Theory Techniques* 23 (1975), p. 85–92.
- [12] *C-Band Booster Optical Amplifier*. BOA 1004P. Thorlabs.
- [13] P. KASPAR et al. “Packaged hybrid III-V/silicon SOA”. In : *2014 The European Conference on Optical Communication (ECOC)*. Sept. 2014, p. 1–3.
- [14] G. P. AGRAWAL et N. K. DUTTA. *Semiconductor Lasers, second edition*. KLUWER ACADEMIC PUBLISHERS, 1993.
- [15] G.-H. DUAN et al. “Hybrid III-V Silicon Photonic Integrated Circuits for Optical Communication Applications”. In : *IEEE Journal of Selected Topics in Quantum Electronics* 22.6 (2016), p. 1–11.
- [16] V. JAYARAMAN, Z.-M. CHUANG et L. A. COLDREN. “Theory, design, and performance of extended tuning range semiconductor lasers with sampled gratings”. In : *IEEE Journal of Quantum Electronics* 29.6 (1993), p. 1824–1834.
- [17] A. J. WARD et al. “Widely tunable DS-DBR laser with monolithically integrated SOA: design and performance”. In : *IEEE Journal of selected topics in quantum electronics* 11.1 (2005), p. 149–156.
- [18] S. MATSUO et T. SEGAWA. “Microring-resonator-based widely tunable lasers”. In : *IEEE Journal of Selected Topics in Quantum Electronics* 15.3 (2009), p. 545–554.
- [19] T. CHU, N. FUJIOKA et M. ISHIZAKA. “Compact, lower-power-consumption wavelength tunable laser fabricated with silicon photonic wire waveguide micro-ring resonators”. In : *Optics express* 17.16 (2009), p. 14063–14068.

- [20] T. SEGAWA et al. “A novel tunable laser with flat-output wideband tuning based on parallel ring resonators”. In : *2012 International Conference on Photonics in Switching (PS)*. IEEE. 2012, p. 1–3.
- [21] L. VIVIEN et L. PAVESI. *Handbook of silicon photonics*. Taylor & Francis, 2016.
- [22] H. DEBRÉGEAS et al. “Record 6dBm Electroabsorption Modulated Laser For 10Gb/s and 25Gb/s High Power Budget Access Networks”. In : *Optical Fiber Communication Conference*. Optical Society of America. 2017.
- [23] Y. TANG, J. D. PETERS et J. E. BOWERS. “Over 67 GHz bandwidth hybrid silicon electroabsorption modulator with asymmetric segmented electrode for 1.3 μm transmission”. In : *Optics express* 20.10 (2012), p. 11529–11535.
- [24] S. R. JAIN et al. “Integrated hybrid silicon transmitters”. In : *Journal of Lightwave Technology* 30.5 (2012), p. 671–678.
- [25] A. GARREAU et al. “10Gbit/s Amplified reflective electroabsorption modulator for colourless access networks”. In : *2006 International Conference on Indium Phosphide and Related Materials Conference Proceedings*. IEEE. 2006, p. 168–170.
- [26] X. POMMAREDE et al. “Transmission Over 50km at 10Gbs/s with a Hybrid III-V on Silicon Integrated Tunable Laser and Electro-absorption Modulator”. In : *Optical Fiber Communication Conference*. Optical Society of America. 2016, p. M2C–7.
- [27] M. WEBSTER et al. “An efficient MOS-capacitor based silicon modulator and CMOS drivers for optical transmitters”. In : *11th International Conference on Group IV Photonics (GFP)*. 2014.
- [28] T. FERROTTI et al. “Power-efficient carrier-depletion SOI Mach-Zehnder modulators for 4x25Gbit/s operation in the O-band”. In : *SPIE OPTO*. International Society for Optics et Photonics. 2015, p. 93670D–93670D.
- [29] M. PANTOUVAKI et al. “56Gb/s ring modulator on a 300mm silicon photonics platform”. In : *Optical Communication (ECOC), 2015 European Conference on*. IEEE. 2015, p. 1–3.
- [30] D. MARRIS-MORINI et al. “Low loss 40 Gbit/s silicon modulator based on interleaved junctions and fabricated on 300 mm SOI wafers”. In : *Optics express* 21.19 (2013), p. 22471–22475.
- [31] S. AKIYAMA et T. USUKI. “High-speed and efficient silicon modulator based on forward-biased pin diodes”. In : *Frontiers in Physics* 2 (2014), p. 65.
- [32] I. KANG. “Phase-shift-keying and on-off-keying with improved performances using electroabsorption modulators with interferometric effects”. In : *Optics express* 15.4 (2007), p. 1467–1473.
- [33] H. MARDOYAN et al. “PIC-to-PIC experiment at 130Gb/s based on a monolithic transmitter using switching of prefixed optical phases and a monolithic coherent receiver”. In : *Optical Fiber Communication Conference*. Optical Society of America. 2014, Th5C–2.

Conclusion & Perspectives

THE main goal of this thesis was the realisation of integrated I/Q transmitters and coherent receivers. To do so, the basic building blocks and wavelength multiplexers were thoroughly studied, followed by active devices such as tunable lasers, EAM and silicon modulators. Finally, design and preliminary results on I/Q modulators were presented.

Highlights

The main achievements of this thesis are described below, chapter by chapter.

Passive Building Blocks

- Analysis of strip and rib waveguides with propagation losses measurements. The rib waveguide exhibits losses around 1.4dB/cm and the strip waveguide lower than 4dB/cm.
- **Simulation and measure of various types of bends.** The study was able to find the best shape as a function of the desired bend radius, with clothoid bends for large radii and hyperbolic cosine for smaller radii. **The optimised bends have bend losses much lower than the linear propagation losses** due to waveguide rugosity.
- Power splitters in the form of directional couplers and MMI were measured. The results are promising as for their addition in integrated devices. The MMI exhibits a very good balancing of the outputs and the directional coupler shows very small insertion losses.
- Guide crossings that are necessary in the elaboration of coherent receivers. Losses are around 0.3dB per crossing.
- **Different designs of hybrid 90°.** It was found that the smaller MMI has better simulated performances, but the longer is more robust to fabrication uncertainties. **The measured performances are compatible with coherent receivers.**

Wavelength Division Multiplexing : passive devices

Three different types of wavelength multiplexers were studied : first the ring resonator-based multiplexer, then echelle gratings (EG) and finally arrayed waveguide gratings (AWG). A Ring resonator-based multiplexer was demonstrated with 8 channels spaced 100GHz. The insertion losses were very low but an individual control of peak position was necessary.

Two designs of echelle gratings were demonstrated. One for DWDM applications and the other for CWDM applications. The first is an EG with 16 channels spaced 100GHz. **State of the art results are achieved** with insertion losses lower than 2dB and a crosstalk around 15dB for all 16 channels. The second device exhibited **4 channels spaced 20nm with a flat top behaviour and reasonable crosstalk**. This was made possible thanks to the use specifically designed input and output mode profiles.

AWG were thoroughly studied and **a simulation tool was created from scratch during the thesis**. This tool can simulate several kind of devices, including flattened-top AWG. **Retro-simulation were also performed and prove the validity of the simulation tool**. Other designs were discussed and their fabrication is expected in the near future.

Active Components & Integration

Several active components were studied in the last chapter. SOA and tunable laser show good performances compatible with an integration in I/Q modulators and coherent receivers. Mach-Zender PN modulators were also tested. The present samples have a $V_\pi L_\pi$ lower than 3V.cm with an electro-optical bandwidth up to 12GHz.

In the last chapter were also presented the results of **the first realisation of a tunable laser with an integrated EAM on the hybrid III-V on silicon platform at 10Gbit/s**. A second generation was also measured. It exhibits the same performances as the first generation, but with a larger optical budget of 10dB.

The main interest of this thesis was the realisation of integrated I/Q modulators and coherent receivers. Two types of I/Q modulators were studied, one that uses silicon PN junction and the other that uses EAM modulators.

Perspectives and future work

Although many interesting results were presented in this thesis, most of the layouts designed during the thesis are still under fabrication. The near future should see new measurement results from the next generations of integrated components. Some of the devices coming in the future are :

- A new generation of integrated silicon I/Q modulators modulators with optimised RF performances.
- Shorter EAM with a predicted bandwidth compatible with 25GHz operation and I/Q modulators with the modified EAM.
- Several generations of coherent receivers.
- WDM transmitter with multiple directly modulated lasers and wavelength multiplexer (EG or AWG). Devices with four and sixteen channels have been designed. The lasers are either DFB or tunable lasers.
- The same devices as above, but with an EAM to modulate the signal instead of direct modulation of the laser.

Looking in the future, there is no doubt that hybrid III/V PICs will find interesting applications for optical communications. However, there are still several challenges to be overcome :

- **Fabrication yield and reliability** : As the number of functions on a chip increases, so must the yield of individual building blocks. The main problem that was met during this thesis is that the fabrication uncertainties are still very large compared to the typical sizes of our devices. As a result, one can observe deviations in performance from device to device. The main challenge in order to create reproducible integrated devices is therefore to reduce these deviations in order to have a large percentage of the integrated devices that are fully functional at the end of the fabrication process.
- **Packaging between PICs and electronic circuits** : The question is how to co-package PICs and electronic circuits with a large number of connections. 3D packaging with the copper pillars technology used in micro-electronics could be a solution to that problem.
- **Power consumption** : The integrated devices still have a large power consumption, which can cause issues due to the very small size of the device. Progress must be made to further reduce the energy consumption of the PICS. One of the possible ways would be to drastically reduce the power consumption of the tuning sections such as static phase-shifters.

Résumé (Français)

Le monde des télécommunications a vu de très nombreux changements au cours des dernières décennies. La croissance exponentielle de la consommation de données a été rendue possible par le développement des communications par fibre optique. Parmi les technologies émergentes appelées à améliorer les capacités des réseaux actuels se trouve la photonique sur silicium, et plus particulièrement la plateforme III-V sur silicium développée par notre équipe. Cette plateforme utilise les technologies de fabrication de la micro-électronique et les applique à la réalisation de composants photoniques. Un collage de matériaux III-V, typiquement du phosphure d'indium est ajouté afin d'apporter une section d'amplification au dispositif.

Le principal objectif de cette thèse est la réalisation de transmetteurs I/Q et de récepteurs cohérents. Pour ce faire, plusieurs briques de base passives sont nécessaires et ont été étudiées dans les chapitres 2 et 3. Le chapitre 4 traite des composants actifs (lasers, SOA (semiconductor optical amplifier), MEA (modulateur à électro-absorption) et modulateurs silicium). Des résultats préliminaires de modulateurs I/Q ont aussi été présentés dans ce dernier chapitre.

Briques élémentaires passives

- Analyse de guides photoniques de type 'strip' et 'rib'. Les guides présentent un comportement monomode et des pertes d'insertion mesurées de 1.4dB/cm et 4dB/cm respectivement.
- Simulation et mesure de plusieurs types de virages. L'étude a permis de déterminer la meilleure forme de virage en fonction de la taille désirée. Les virages basés sur des cosinus hyperboliques sont préférables pour les faibles rayons de courbure et les clothoïdes pour les rayons de courbure plus élevés. Les mesures montrent que les pertes dues aux virages suivant ces recommandations sont beaucoup plus faibles que les pertes linéiques de propagation dues à la rugosité du guide.
- Des diviseurs de puissance sous la forme de coupleurs directionnels et d'interféromètres multimode (MMI) ont été étudiés. Des résultats prometteurs ont été obtenus dans les deux cas. Les MMI sont préférables pour les applications nécessitant un bon équilibrage des puissances. Les coupleurs directionnels, quant à eux, seront utilisés dans les applications où les réflexions parasites sont problématiques.

- Simulation et mesure de croisements de guides. Deux géométries différentes ont été étudiées, l'une avec un élargissement linéaire du guide avant le croisement, et l'autre avec un élargissement plus travaillé en forme de 'S'. Ce dernier dispositif présente de meilleures performances avec des pertes de l'ordre de 0.3dB par croisement avec un crosstalk supérieur à 40dB.
- Simulation et mesure d'hybride 90. Ces composants sont essentiels à la réalisation de récepteurs cohérents. Un MMI 4X4 a été choisi pour remplir cette fonction. Plusieurs designs présentant des gabarits différents ont été proposés. Il en ressort que les récepteurs cohérents les plus courts ont des résultats de simulation et de mesure meilleurs que les longs, mais avec une variabilité due aux incertitudes de fabrication beaucoup plus importante.

Multiplexage en longueur d'onde

Trois types de (dé)multiplexeurs ont été étudiés au cours de la thèse. Premièrement, un dispositif qui utilise des résonateurs en anneau en série pour extraire chacune des longueurs d'onde. La seconde catégorie est les réseaux échelle et la troisième les AWG (arrayed waveguide grating).

Un démultiplexeur en anneaux avec 8 canaux séparés de 100GHz a été démontré. Il présente d'excellentes performances en termes de pertes d'insertion, mais un contrôle individuel de la position des canaux est rendue indispensable par les variabilités de fabrication.

Deux designs de réseaux échelle ont été proposés. Le premier avec 16 canaux séparés de 100GHz et le second avec 4 canaux séparés de 20nm avec un profil aplati. Le premier dispositif a montré des performances à la pointe de la recherche avec des pertes d'insertion inférieures à 2dB et un crosstalk de 15dB. Le second dispositif présente des caractéristiques prometteuses avec un profil bien aplati, performance rendue possible grâce à l'utilisation spécifique de MMI en entrée et en sortie du réseau échelle.

Dans la dernière partie de ce chapitre, la théorie des AWG a été explorée et un outil de simulation a été développé sur les bases de cette théorie. Ce nouvel outil permet de faire une simulation complète d'AWG. Des rétro-simulations ont été faites qui prouvent la validité de l'outil de simulation.

Composants actifs et intégration

Dans ce chapitre ont été étudiés plusieurs composants comportant une section active en matériaux III-V. Les SOA et lasers accordables étudiés présentent de bonnes performances compatibles avec leur utilisation dans les dispositifs intégrés. Ont également été étudiés les modulateurs silicium. Ces derniers présentent un $V_{\pi}L_{\pi}$ plus faible que 3V.cm avec une bande passante de 12GHz. Ce chapitre couvre également les premiers résultats de dispositifs intégrés. Le premier et plus simple d'entre eux est un laser intégré avec un MEA. La première génération démontre une transmission à 10Gbit/s sur 50km avec une accordabilité de 10nm. La seconde génération présente des caractéristiques similaires, mais avec un meilleur budget

optique, jusqu'à 10dB. L'objectif ultime de cette thèse est la réalisation de transmetteurs I/Q. Plusieurs variations ont été étudiées à la fin de ce chapitre.

List of Acronyms

AWG Arrayed Waveguide Grating.

BB Building Blocks.

BER Bit Error Rate.

BPSK Binary Phase Shift Keying.

CMP Chemical Mechanical Planarisation.

CMRR Common Mode Suppression Ratio.

DC Directional Coupler.

DSP Digital Signal Processing.

EAM Electro-Absorption Modulator.

EDFA Erbium Doped Fiber Amplifier.

EG Echelle Grating.

FEC Forward Error Correction.

FGC Fiber Grating Coupler.

FPR Free Propagation Region.

FSR Free Spectral Range.

HDP High Density Plasma deposition.

I/Q modulator In phase/Quadrature modulator.

InP Indium Phosphide.

laser Light Amplification by Stimulated Emission of Radiation.

LO Local Oscillator.

MMI MultiMode Interferometer.

MZ Mach-Zehnder.

NRPS Non-Reciprocal PhaseShift.

NZR Non-Zero return.

ONU Optical Network Unit.

OOK On-Off Keying.

OSA Optical Spectrum Analyser.

OSI Open Systems Interconnection.

PAM Power Amplitude Modulation.

PIC Photonic Integrated Circuit.

PRBS Pseudo Random Binary Sequence.

QAM Quadrature Amplitude Modulation.

QPSK Quadrature Phase Shift Keying.

RIE Reactive Ion Etching.

SEM Scanning Electron Microscope.

SMF Single Mode Fiber.

SMSR Side Mode Suppression Ratio.

SOA Semi-Conductor Amplifier.

TUL Tunable Laser.

WDM Wavelength Division Multiplexing.

WM Wavelength (de)-Multiplexer.

Titre : Circuits photoniques intégrés III-V/Si pour les applications en télécommunications optiques.

Mots clefs : photonique, integration, silicium, laser, modulateur, multiplexeur

Résumé : Afin de poursuivre leur montée en débit, les composants des télécommunications par fibre optique nécessitent l'élaboration de nombreuses briques de base : laser, modulateur, photo-détecteur, multiplexeur... et leur intégration avec les circuits de traitement du signal. Cette thèse a pour objectifs de concevoir et de caractériser ces différentes briques actives et passives en utilisant la technologie hybride III-V/Si. Ces briques sont ensuite utilisées dans des circuits photoniques intégrés (PIC) complets d'émission et de réception, qui présentent des avantages tels qu'une taille réduite, une consommation et un coût de fabrication faibles. . Après une partie d'introduction, plusieurs éléments passifs sont étudiés en détail dans la 2ème partie : guides d'ondes, virages, diviseurs de puissance, croisements de guides et hybride 90°. Tous ces dispositifs présentent de bonnes performances compatibles avec leur utilisation dans les PICs.

La 3ème partie traite le problème du (dé)-multiplexage en longueur d'onde. Trois dispositifs sont étudiés : le démultiplexeur basé sur des résonateurs en anneau, des réseaux échelle et des AWG (arrayed waveguide grating). Pour les réseaux échelles, des performances à l'état de

l'art ont été démontrées, d'une part sur un composant de 16 canaux séparés de 100GHz et d'autre part sur un composant de 4 canaux séparés de 20nm avec un profil aplati. Une méthode de simulation d'AWG a ensuite été présentée avec des résultats expérimentaux et théoriques à l'appui.

La dernière partie traite des composants dits "actifs" et de l'intégration de toutes les fonctions précédentes dans des circuits photoniques intégrés. Les composants actifs étudiés sont les lasers, les Amplificateurs optiques en semi-conducteurs (SOA), les modulateurs à électro-absorption (EAM) et enfin les jonctions PN sur silicium comme modulateur de phase. Les PICs présentés sont d'abord deux générations de laser accordable intégré avec un EAM avec une transmission à 10Gbit/s sur 50km. Puis sont étudiés des modulateurs I/Q avec source laser accordable intégrée, d'une part avec des jonctions PN en silicium et d'autre part avec des EAM comme modulateurs pour des débits cibles de 25Gbaud/s.

Une conclusion générale est tirée à la fin de la thèse. Des perspectives à court et moyen termes sont également tracées.

Title : Hybrid III-V/Si photonic integrated circuits for optical communication applications

Keywords : photonoc, integration, silicon, laser, modulator, multiplexer

Abstract : In order to follow the new needs in terms of optical bandwidth, optical fiber communications require the elaboration of numerous building blocks : laser, modulator, photo-detector...and their integration with signal processing circuits. This thesis has for objective the conception and characterisation of various active and passive building blocks using the hybrid III-V/Si technology. These building blocks are then used in photonic integrated circuits (PIC) with all the necessary emission and reception functions. This enables a reduced footprint, a lower power consumption and fabrication cost.

After an introduction section, several passive elements are studied in detail in the second part : waveguides, bends, power splitters, waveguide crossings and hybrid 90°. All these designs present good performances compatible with their integration in PICs

The third part treats the problem of wavelength (de)-multiplexing. Three types of device were studied : a demultiplexer based on ring resonators, echelle gratings and arrayed waveguide gratings (AWG). For the echelle gra-

tings, state-of-the-art performances were demonstrated, first on a sample with 16 channels separated 100GHz and on the other hand a sample with 4 channels separated 20nm with a flattened profile. A simulation method for the AWG was presented with experimental and theoretical results to support the method.

The last part is about "active" devices and the integration of all the previous designs in PICs. The studied active components are the lasers, semi-conductor optical amplifiers (SOA), electro-absorption modulators (EAM) and finally silicon PN junctions used as phase modulators. Two generations of a tunable laser integrated with an EAM were studied with a transmission at 10Gbit/s over 50km. The next section studied I/Q modulators with an integrated tunable laser source, using either PN silicon junction modulators or EAM with a target speed of 25Gbaud/s.

A general conclusion is drawn at the end of the thesis. Short term and mid-term perspectives were also drawn.

